

27 years of Spaceborne IR Astronomy: An ISO, Spitzer, WISE and NEOWISE Survey for Large-Amplitude Variability in Young Stellar Objects

CHINMAY S. KULKARNI ,¹ THOMAS BEHLING ,^{1,2} ELISABETH E. BANKS ,¹ JASON JONES,¹ TYLER ROBBINS ,^{1,3} NATHANAEL BURNS-WATSON ,^{1,4} S. THOMAS MEGEATH ,¹ ROBERT GUTERMUTH ,⁵ SAMUEL FEDERMAN ,^{1,6} SAVIO B. OLIVEIRA ,¹ WAFA ZAKRI ,⁷ WILLIAM J. FISCHER ,⁸ AND RIWAJ POKHREL ,¹

¹*Ritter Astrophysical Research Center, Department of Physics and Astronomy, University of Toledo, Toledo, OH 43606, USA*

²*Department of Physics and Astronomy, Michigan State University, East Lansing, MI 48824, USA*

³*Department of Aerospace, Physics and Space Sciences, Florida Institute of Technology, Melbourne, FL 32901, USA*

⁴*Department of Astronomy, University of Texas at Austin, Physics Math and Astronomy Building, Austin TX, 78712, USA*

⁵*Department of Astronomy, Lederle Graduate Research Tower, University of Massachusetts, Amherst, MA 01003, USA*

⁶*INAF-Osservatorio Astronomico di Capodimonte Napoli, IT*

⁷*Physical Sciences Department, Jazan University, Jazan, Saudi Arabia*

⁸*Space Telescope Science Institute, 3700 San Martin Drive, Baltimore, MD 21218, USA*

ABSTRACT

Infrared observations can probe photometric variability across the full evolutionary range of young stellar objects (YSOs), from deeply embedded protostars to pre-main-sequence stars with dusty disks. We present 3-8 μm light curves extending 27 years from 1997 to 2024 obtained with three space-based IR telescopes: ISO, Spitzer and WISE. Although unevenly sampled with large gaps in coverage, these light curves show variability on time scales ranging from days to decades. We focus on the Spitzer-identified YSOs with disks and envelopes that exhibit variations of a factor of two or more in this wavelength range. We identified seven YSOs where the light curves are dominated by bursts of sustained (> 5 yr) high flux, including four that show a steep decay ending the burst and three that are ongoing as of the final observation. We find six YSOs that are undergoing declines, which may be the end of bursts that began before 1997. The most common form of variability, exhibited by 26 YSOs in our sample, show variations over time intervals of years to months but do not exhibit sustained bursts or fades. The Spitzer [3.6]-[4.5] and WISE [3.5]-[4.6] colors either increase or remain constant with increasing brightness, inconsistent with dust extinction as being the primary source of the large-amplitude variability.

Keywords: Young stellar objects, Star formation, Variable stars

1. INTRODUCTION

Young stellar objects (YSOs) exhibit variability across the electromagnetic spectrum, from X-rays to radio waves (e.g. Stauffer et al. 2014; Rebull et al. 2014; Forbrich et al. 2017; Grosso et al. 2020). Observations from the Spitzer space telescope and Wide-field Infrared Survey Explorer (WISE) show that YSOs with dusty disks and envelopes commonly show variability in the 3-8 μm regime (e.g. Morales-Calderón et al. 2011; Megeath et al. 2012; Flaherty et al. 2013; Park et al. 2021). This variability is manifested through a rich range of behaviors, from small-amplitude periodic fluctuations to large-amplitude bursts (e.g. Fischer et al. 2012; Poppenhaeger et al. 2015; Flaherty et al. 2016; Park et al. 2021). In contrast to visible or even near-infrared data, 3-8 μm observations can detect deeply embedded protostars, and thus can be used to observe variability over the full evolutionary sequence of YSOs from Class 0 protostars to evolved pre-main sequence stars with disks (e.g. Rebull et al. 2014; Safron et al. 2015; Zakri et al. 2022).

Large-amplitude variability, which we define to occur when the flux changes by a factor ≥ 2 , may be of particular importance for the formation of stars. These variations can be driven by large changes in the mass accretion rate, where the luminosity released by accretion is reprocessed into infrared radiation (Fischer et al. 2023). The discovery of luminous outbursts, or "bursts", from young stars that lasted decades, and the observation that the typical luminosities of protostars are lower than the expected accretion luminosity, led to a picture where most of a star's mass is assembled during sustained bursts of rapid accretion (Hartmann & Kenyon 1996; Audard et al. 2014; Dunham et al. 2010b; Hartmann et al. 2016; Fischer et al. 2019, 2023; Narang et al. 2024; Hartmann et al. 2025). This picture is supported by models in which disks regulate the accretion of infalling gas onto protostars, leading to episodes of rapid accretion (Vorobyov & Basu 2006; Dunham & Vorobyov 2012). Despite the support for this picture, alternative models for the lower luminosities of protostars remain viable (Offner & McKee 2011; Fischer et al. 2017).

Determining the importance of episodic accretion thus requires direct measurements of time-varying accretion, and in particular the frequency, amplitudes, and durations of accretion bursts (Fischer et al. 2019; Zakri et al. 2022). Since most mass is accreted when protostars are deeply embedded in dense envelopes, measurements in the infrared or sub-millimeter are necessary (e.g. Safron et al. 2015; Mairs et al. 2024). For these sources, bursts can be detected using IR and sub-millimeter light curves, and the durations and amplitudes of bursts constrained from the curves (Fischer et al. 2019; Park et al. 2021; Mairs et al. 2024). Current estimates using $3 - 5 \mu\text{m}$ multi-epoch photometry range from one burst per 1000 years for protostars to one burst per $> 10,000$ years for more evolved pre-main sequence stars with disks (Scholz et al. 2013; Fischer et al. 2019; Zakri et al. 2022); however, comparisons of these studies are complicated by the different criteria and data used to identify bursts. Due to the small number of bursts found in surveys of well characterized populations of YSOs, and the uncertainties in the rates, amplitudes, and durations of the bursts, the contribution of bursts to the total masses of stars remains poorly constrained (Zakri et al. 2022).

Directly measuring infrared variability at $\lambda > 3 \mu\text{m}$ requires the sensitivity and photometric stability of space-based IR telescopes. Due to the limited and inhomogeneous $\lambda > 3 \mu\text{m}$ photometry of YSOs over these timescales, previous work has often made simplifying assumptions, for instance that most large-amplitude variations are sustained outbursts (Fischer et al. 2019). To better characterize the light curves of large-amplitude variables, we construct $3-8 \mu\text{m}$ light curves that span 27 years, the longest possible baseline to measure the mid-IR variability of these objects. These observations start in 1997 with ISOCAM on the Infrared Space Observatory (ISO, Cesarsky et al. 1996). Launched in 1995, ISO was the first space-based IR telescope with the angular resolution needed to separate individual YSOs in nearby star-forming regions (Blommaert et al. 2003; Kaas et al. 2004). Starting in 2004, the IRAC camera on the Spitzer Space Telescope provided high sensitivity with $2''$ angular resolution at $3-8 \mu\text{m}$ (Fazio et al. 2004). Observations at $3-5 \mu\text{m}$ with IRAC continued after the depletion of liquid helium in 2009 until the end of the Spitzer mission in 2019 (Mahoney et al. 2010). The WISE mission launched in 2010, scanned the sky once in all four bands and then, after the cryogen was depleted, a second time in three of its original wavebands (Wright et al. 2010). In 2013, the satellite was revived for observations in the 3.5 and $4.6 \mu\text{m}$ bands as part of the Near-Earth Object Wide-Field Infrared Survey Explorer (NEOWISE) mission, which scanned the entire sky twice a year (Mainzer et al. 2014). The last NEOWISE epoch was in July 2024, after which the mission ended¹.

The combined ISOCAM, Spitzer, and (NEO)WISE light curves give the longest time interval over which YSO variability can be measured at $> 3 \mu\text{m}$, although they suffer from large gaps in time coverage and the poor photometric accuracy of ISOCAM (Kulkarni et al. 2024). In this contribution, we publish the light curves of YSOs with full 27 year coverage. These YSOs were identified by Spitzer surveys of clouds and clusters within 500 pc, and all show infrared emission from dusty disks and envelopes (Evans et al. 2009; Gutermuth et al. 2009; Megeath et al. 2012; Kryukova et al. 2012; Dunham et al. 2015; Furlan et al. 2016; Pokhrel et al. 2023). Given the limitations of the data, we focus on YSOs showing large-amplitude variations in the $3-4 \mu\text{m}$ wavelength range covered by the shorter bands of Spitzer/IRAC, WISE and NEOWISE, or the $4-8 \mu\text{m}$ range covered by the longer wavelength filters of (NEO)WISE and the IRAC and ISOCAM cameras. Despite these limitations, the long time coverage of these observations can give our best constraints on the durations of bursts.

2. ASSEMBLING LIGHT CURVES

To generate light curves that extend up to 27 years, we assemble photometric data obtained from three space telescopes over five missions. The first epoch was obtained in 1997 with the Infrared Space Observatory (ISO), which

¹ <https://neowise.ipac.caltech.edu/news/neowise20240807/>

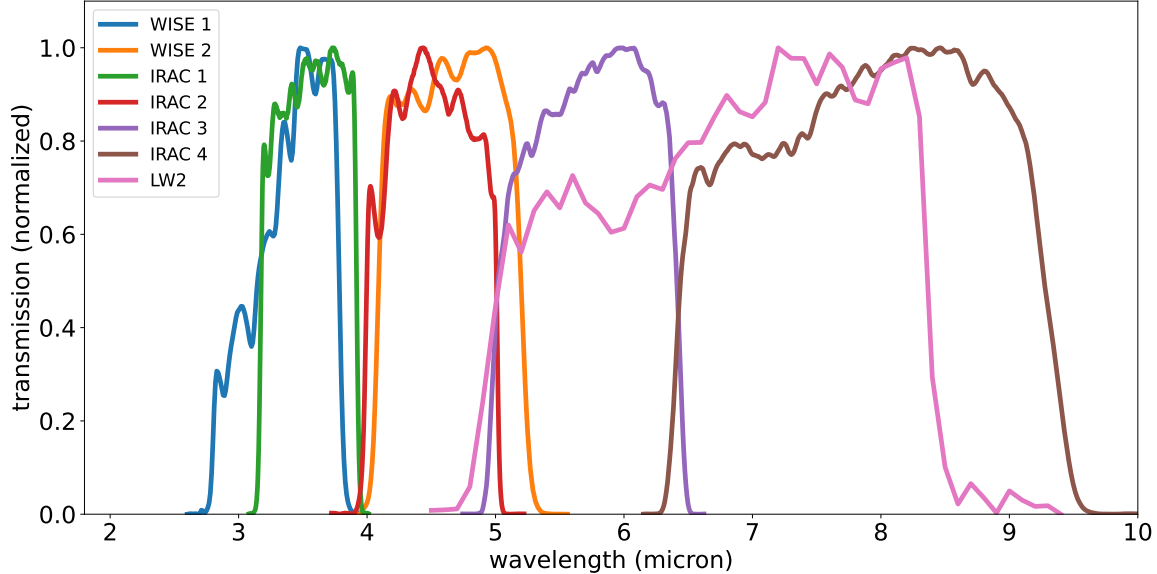


Figure 1. Transmission profiles of the six filters discussed in this work. While the WISE W1 and W2 filters significantly overlap with the IRAC I1 and I2 filters, the LW2 filter used for most of the ISO data overlaps with the I3 and I4 filters, with only minor overlap with the I2 filter. Thus, we use cryogenic Spitzer observations made in the I2, I3 and I4 filters to determine a typical offset of the LW2 filter to the I2 filter (2.2). The bandpasses are sourced from <https://svo2.cab.inta-csic.es/theory/fps/> (Rodrigo et al. 2012).

was in operation from 1995 to 1998. The ISOCAM camera surveyed 15 star-forming regions in the LW2 (5-8.5 μm) and LW3 (12-18 μm) bands (Olofsson et al. 2000; Kaas et al. 2004). The second is the Spitzer Space Telescope, which was in operation between 2003 and 2020. The cryogenic mission of Spitzer lasted from 2003 to 2009. During this mission, many star-forming regions were surveyed using the 3.6 (IRAC 1, or I1), 4.5 (IRAC 2 or I2), 5.8 (IRAC 3 or I3), and 8 μm (IRAC 4 or I4) bands of the IRAC camera, and the 24 μm band of the MIPS instrument as part of the c2d survey, Orion survey, and GTO cluster survey (Evans et al. 2009; Megeath et al. 2012; Gutermuth et al. 2009). Following the depletion of the cryogen in 2009, the warm mission of the telescope began, during which only the 3.6 and 4.5 μm bands of the IRAC camera were operated. This phase of the mission included several programs designed to re-observe star-forming regions surveyed in the cryo-mission, the most extensive of which was the YSOVAR exploration program (Morales-Calderón et al. 2011; Flaherty et al. 2013; Rebull et al. 2014; Flaherty et al. 2016; Zakri et al. 2022). WISE surveyed the sky first in four bands, 3.4 μm (WISE 1 or W1), 4.6 μm (WISE 2 or W2), 12 μm (WISE 3 or W3) and 23 μm (WISE 4 or W4), and then a second time in three bands, W1, W2 and W3. The telescope began operating in 2010 and was put in hibernation in 2011 after the depletion of the cryogen. In 2013, the satellite was reactivated as part of the NEOWISE mission. In this warm phase of the mission, only the W1 and W2 bands were operable. The NEOWISE mission scanned the sky twice a year until it ended in 2024 (Mainzer et al. 2014). During each of these scans, each object is observed approximately ten times over intervals up to 4 days. In total, the three telescopes provide coverage in the 3-8 μm regime over 27 years, although not continuously. In Fig. 1, we show the filter profiles for the bandpasses used in this paper. Sources in this study satisfy the following criteria: i.) they are identified as a YSO with a disk or envelope, ii.) their ISO photometry is not affected by source confusion or artifacts, iii.) they have Spitzer photometry from the cold and warm mission, and iv.) they have NEOWISE photometry extending to 2020 at minimum.

2.1. Spitzer YSO Catalog

We focus on YSOs identified by Spitzer using methods developed to identify pre-main sequence stars with disks and protostars (Gutermuth et al. 2009; Kryukova et al. 2012; Megeath et al. 2012, 2016). For the Orion clouds, we use the YSO catalog generated from the cryogenic Spitzer Orion survey (Megeath et al. 2012, 2016). For the remaining clouds, we use the SESNA reprocessing of the Spitzer data (Pokhrel et al. 2020). Since Spitzer has a higher sensitivity and a finer angular resolution than ISOCAM or WISE, these data provide a complete sample of the dusty YSOs that can be detected in the ISOCAM and (NEO)WISE surveys. These catalogs also provide photometry in the IRAC I1,

I2, I3, and I4 bands determined from either the mosaics of the combined images from the 2004 cryogenic epochs, or the median photometry values from all the 2004 cryogenic epochs (Gutermuth et al. 2009; Megeath et al. 2012).

2.2. ISOCAM Photometry

To obtain photometry spanning 27 years, we only look at Spitzer-identified YSOs that are detected with ISOCAM. We extracted ISOCAM photometry from images downloaded from the ESO ISO Data Science Archive². The images we used were all obtained in the LW2 (6.7 μm) band in either the 3" or 6" pixel scale. We used the fits files prefixed with "CSP". The images come from the ISOCAM survey of nearby star-forming regions (Olofsson et al. 2000). Here we chose the star-forming regions within 500 pc that had been observed over multiple epochs by Spitzer, specifically Orion B, L1641N in Orion A, Ophiuchus, the NGC 1333 cluster in the Perseus cloud, the Serpens Main cluster in the Aquilla cloud, Corona Australis, and parts of the Chameleon cloud. We did not include Taurus due to the limited multi-epoch Spitzer photometry for that region.

To find sources in the ISOCAM images, we first used DAOStarFinder in the Python Photutils package³, which is adapted from DAOFIND (Stetson 1987). We modified this routine to calculate a local background noise level in a 11×11 pixel square centered on each source, based on the approach of the IDL routine PhotVis (Gutermuth et al. 2009), and searched for sources that were $\geq 3 - 5\sigma$ over the noise, where the exact limit was chosen for each individual image. We then inspected the images, first editing out sources that were visually identified artifacts, multiples resolved in the higher-resolution Spitzer data that are not resolved by ISOCAM, or sources too close to either the edges of the images or bright nebulosity. We then added point sources that were missed by DAOStarFinder and found by eye.

We matched these sources to point source catalogs from the Spitzer Orion program or the SESNA reprocessing of the Spitzer data (Megeath et al. 2012, 2016; Pokhrel et al. 2020). To do this, we first shifted the ISOCAM images to better match the Spitzer astrometry. After this refinement of the ISOCAM astrometry, we matched the ISOCAM sources to the Spitzer sources. There are numerous artifacts in the ISOCAM data, often induced by the presence of a bright source in a scan or noise near the edges of the images. Since the sensitivity and angular resolution of the IRAC camera are higher than those of ISOCAM, if there was no source in the Spitzer catalog within 15" of a given ISO source, the ISO source was considered an artifact and deleted. Sources near the ISOCAM detection limit would have to decline by ≥ 4 magnitudes to evade detection by Spitzer. Since we only consider sources identified as YSOs by Spitzer, such sources would not be in our YSO catalog. A total of 256 sources were found.

We improved the positions of the ISOCAM point sources by fitting 2D quadratic polynomials to the PSFs using the centroid_quadratic function based in the Python PhotUtils package, with fit box and search box sizes of 5 pixels and 9 pixels, respectively. Centered on these positions, we performed aperture photometry with the Python PhotUtils package, adopting a circular aperture with a radius of 3 pixels. The background contribution was measured using the MMM statistic in an annulus extending from 4 pixels to 10 pixels. We converted the background-subtracted ISO fluxes to Vega magnitudes using the zero-point of 90.2 Jy/pixel (Blommaert et al. 2003).

To cross-calibrate the ISOCAM data with Spitzer, we compared the ISOCAM LW2 photometry with that of the Spitzer I3 (5.8 μm) and I4 (8 μm) bands for all cross matched sources in a given cloud. The LW2 filter covers the entire I3 filter and part of the I4 filter (Fig. 1). For this reason, we examined the offsets between the ISOCAM LW2 photometry and the I3 photometry, between LW2 and the I4 photometry, and between LW2 and a combination of the I3 and I4 photometry. To calculate the combination of the I3 and I4 photometry, we used

$$I_{\text{comb}} = -2.5 \log_{10} \left(F_0(I3) \cdot 10^{-m(I3)/2.5} \cdot \frac{c\Delta\lambda_{I3}}{\lambda_{I3}^2} + F_0(I4) \cdot 10^{-m(I4)/2.5} \cdot \frac{c\Delta\lambda_{I4}}{\lambda_{I4}^2} \right) + ZP, \quad (1)$$

where $F_0 = 115$ and 64.13 Jy are the zero flux densities for the I3 and I4 bands, respectively (Reach et al. 2005), c is the speed of light, $\lambda_{I3} = 5.731 \mu\text{m}$ and $\lambda_{I4} = 7.872 \mu\text{m}$ are the nominal wavelengths of the I3 and I4 bands, respectively (as defined in Reach et al. 2005), and $\Delta\lambda_{I3} = 1.42 \mu\text{m}$ and $\Delta\lambda_{I4} = 2.93 \mu\text{m}$ are the filter widths for the two bands, respectively (IRAC instrument handbook⁴). The zero point (ZP) is set so that I_{comb} equals zero when $m(I3)$ and $m(I4) = 0$, which gives $ZP = 38.451$ mag.

In Fig. 2, the differences between the ISOCAM and IRAC magnitudes are plotted for the sources in each of the clouds after the subtraction of a median offset. The median offsets and the median absolute deviation of the offsets

² <https://nida.esac.esa.int/nida-cl-web/>

³ <https://photutils.readthedocs.io/en/stable/citation.html>

⁴ <https://irsa.ipac.caltech.edu/data/SPITZER/docs/irac/iracinstrumenthandbook/>

Table 1. ISO vs Spitzer median offsets and MADs

Region	Medians			MADs		
	5.8 μ m	8.0 μ m	Combined	5.8 μ m	8.0 μ m	Combined
Orion B	0.053	0.854	0.444	0.314	0.232	0.256
Orion A	0.396	1.049	0.707	0.197	0.226	0.198
Ophiuchus	0.311	1.034	0.618	0.211	0.214	0.202
Perseus	-0.031	0.810	0.361	0.278	0.235	0.253
Serpens	0.191	0.901	0.517	0.248	0.248	0.237
CrA	0.059	0.699	0.376	0.241	0.186	0.199
Chameleon	0.131	0.791	0.411	0.172	0.235	0.166

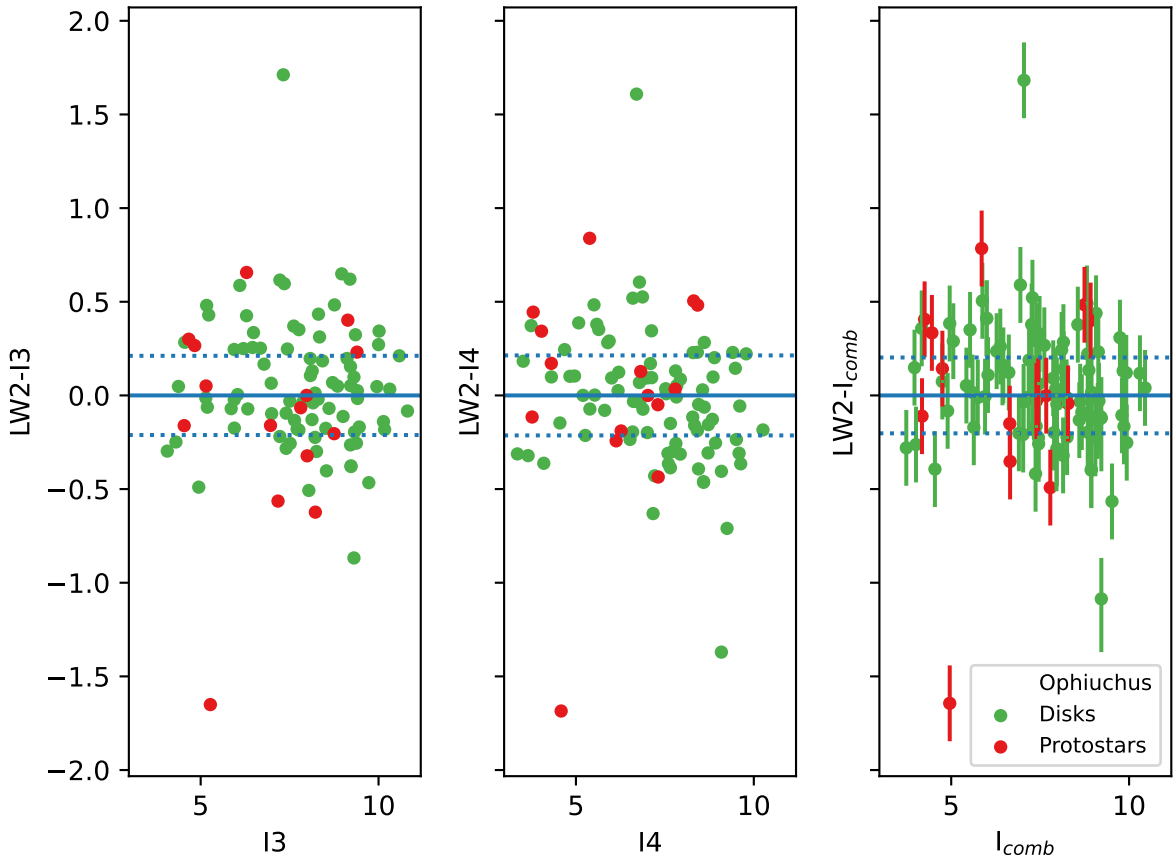


Figure 2. ISOCAM - IRAC magnitude differences for each of the clouds. The red dots are YSOs classified as protostars and the green dots are those classified as pre-main sequence stars with disks. The median differences between the ISOCAM and IRAC data presented in Table 1 have been subtracted so that the points have a median value of 0, as shown by the solid blue line. The values of the median absolute deviations (MADs) are given by the dotted blue lines. Sources toward the top of the plots show large increases in magnitudes between the ISO and Spitzer epochs, while points near the bottom show large decreases. In the LW2-I_{comb} plot (3rd panel), the error bars extends between the LW2-I3 and the LW2-I4 points. If that value is less than the MAD value for the combined plot, we set the length of each of the error bars equal to the MAD. Note that some of the data points showing large differences are not in our sample of large-amplitude variables due to the lack of the necessary Spitzer and (NEO)WISE data.

(MADs) for each field are given in Table 1. Since the sources bright enough to detect in ISO are typically YSOs, they may have intrinsic variability. For this reason, we cannot separate noise and calibration issues from intrinsic source

variability in the $\sim 25\%$ scatter given by the MADs. We therefore consider this scatter as an upper limit to the uncertainties due to noise and calibration.

2.3. *Spitzer Photometry*

The Spitzer photometry was extracted from archival data downloaded from the Spitzer Heritage Archive. The extraction method is described in [Zakri et al. \(2022\)](#). We obtain Spitzer photometry from the observations of the cryogenic survey of Orion (PID 43: Mar and Oct 2004), the warm-mission Orion: The Final Epoch program (PID 13010: Jan and Jun 2017), and observations taken during the Spitzer Final Voyage mission (PID 14301: Jul 2019). We use the cryogenic data taken in 2004 from the c2d survey for Ophiuchus (PID 177), NGC 1333 (PID 178), Serpens (PID 174), and Chameleon (PID 176), and from the Spitzer GTO Cluster Survey (PID 4) of Ophiuchus, NGC 1333, and Serpens ([Evans et al. 2009](#); [Gutermuth et al. 2009](#)). In addition, we have cryogenic photometry of Corona Australis from the Spitzer Gould Belt program (PID 30574 May 2008). We use warm-mission YSOVAR data for Ophiuchus (PID 61024), NGC 1333 (PID 61026), and Serpens (PID 61029); see [Rebull et al. \(2014\)](#) for the time sampling of these data. We also use high cadence data from Flaherty on Chameleon (PID 90141 and PID 12090). Finally, we use data from a warm-mission proper motion survey by Kraus (PID 90071) that observed Chameleon, Corona Australis, Ophiuchus, and Perseus in 2013/2014.

2.4. *WISE/NEOWISE Photometry*

The (NEO)WISE data included the analysis are collected from two archives; the NEOWISE Reactivation Releases available on the Infrared Science Archive (IRSA) and the unTimely catalog ([Meisner et al. 2023](#)). Although they originate from the same data, we use photometry from both catalogs as separate data points in our analyses. The NEOWISE Reactivation Releases, available from the InfraRed Science Archive (IRSA, [Cutri et al. 2015](#)), contains profile-fit, single-exposure photometry released on a yearly basis starting in 2013 and continuing to the deactivation of the mission in 2024. These data include passes across each source every six months as the satellite scanned the sky, with each pass containing multiple exposures. Since our focus is large-amplitude variability on longer timescales and since the individual single exposure frames suffer from a lower sensitivity and redundancy that can make them sensitive to artifacts, we combine the multiple exposures. To obtain the data from IRSA, we used the Python package PyVO to access the IVOA API available from the IRSA website. Initially, a simple-cone-search (SCS) operation was performed to retrieve any photometric detections within $5''$ of the given target position. We then imposed the restriction that the detection must be $1''$ from the source position in the Spitzer SESNA catalog. These detections were filtered using the criteria shown in Table 2. The detections were then divided into passes spaced by approximately 6 months. Within a given pass, we use all detections within $1''$ from the Spitzer location given in the SESNA catalogs. After removing detections containing saturated pixels, a median magnitude and standard deviation were determined from the remaining photometry points and used for that specific epoch. The small standard deviations show no indication of substantial variability over the few day intervals of each NEOWISE scan.

The unTimely catalog [Meisner et al. \(2023\)](#) was generated with an alternative reduction of both the WISE and NEOWISE data, and includes original WISE mission data along with the reactivation releases up to 2020. The unTimely archive consists of a set of distinct catalogs each covering a different region of the sky ([Meisner et al. 2023](#)). Using the catalog index for unTimely, any catalog centered within 2 degrees of a Spitzer YSO detected by ISOCAM were downloaded. The detections in these catalogs were sorted by distance from the SESNA position of the source, and we used the closest detection within $1''$ of the SESNA position. Only the detections within $1''$ of the SESNA position in any given epoch are included. For each six month pass, a single epoch of photometry is tabulated. Any detection with an UNWISE Saturation flag of True are marked as saturated.

Since many of the YSOs are bright, saturation must be considered in the data. As a source is scanned by (NEO)WISE, the sources may be saturated or unsaturated in the individual data frames depending on how the point source is divided by the under-sampled pixels. For the IRSA reactivation data, we removed any detections which were flagged as containing saturated pixels. If there are no detections without unsaturated data, we do not show that data point in the light curves. For unTimely, we included sources that were flagged as having saturated pixels in any of the passes, but marked those points as potentially being affected by saturation. For these sources, some of the data used in the PSF fits used to determine the unTimely magnitudes may be saturated.

Figure 3 compares the photometry returned from the two archives for all sources which also have ISOCAM and Spitzer detections. A single source is represented by a cluster of points consisting of the different epochs of that

Table 2. Filtering Criteria for (NEO)WISE data from IRSAs.

Filtering Property	Filtering Variable	Value Constraint
Reduced Chi-Squared	w1rchi2, w2rchi2	Both less than 2.5
Signal-to-Noise Ratio	w1snr, w2snr	Both greater than 2.0
Frame Quality	qual_frame	Not equal to 0
Image Quality	qi_fact	Not equal to 0
SAA Separation	saa_sep	Greater than 5
Image Saturation	w1sat, w2sat	Both equal to 0

source. A small offset between the IRSAs and unTimely magnitudes is apparent, with the IRSAs magnitudes being fainter by a median value of 0.017 mag for W1 and 0.033 mag for W2. For the sources fainter than 14th magnitude in W1 and 13th magnitude in W2, larger deviations between the IRSAs and unTimely magnitudes are apparent.

To evaluate the effect of saturation on Fig. 3, we examined each pass in the IRSAs NEOWISE data for saturation. Within a single pass, frames may be saturated if the source is centered on a single pixel and unsaturated if the peak is divided between four pixels, for example. For each pass, we split the frames into samples with and without saturated pixels. We then produced two different photometry points by taking the median of each sample and plotted these points separately. We also marked the unTimely sources that are flagged as having saturated pixels. We find that in most cases, photometry from saturated IRSAs data shows slightly brighter magnitudes than unTimely photometry of the same sources, including those cases where the unTimely data are not flagged as saturated. We also find that there are a number of sources that are flagged as saturated in unTimely, but do not have saturated pixels in the IRSAs data and have modest magnitudes.

In total, this analysis shows that sources brighter than 8th magnitude in the W1 band, and 7th mag in the W2 band, must be viewed with caution. To assess the effects of saturation on the light curves in Sec. 3, we mark unTimely (and Spitzer) data points that are potentially affected by saturation, compare the IRSAs and unTimely data when possible, check that the W1 and W2 data show the same trends, and report the magnitudes of the sources in the legends of the light curves.

2.5. Composite Light Curves

We assemble, for each source, two composite light curves from the photometry described above. The first composite light curve is assembled from the Spitzer I1 and WISE W1 bands. Since we reference everything to the Spitzer I1 band, we refer to this as the $3.6\ \mu\text{m}$ light curve. The second composite light curve is constructed from the I2, W2, and ISOCAM LW2 bands; this is referenced to the I2 band and is referred to as the $4.5\ \mu\text{m}$ light curve.

In this approach, the Spitzer I1 and I2 photometry are the ultimate reference points, and hence we cross-calibrate and correct the ISOCAM and WISE photometry so that it better agrees with the IRAC photometry. For the Spitzer photometry, we simply set the magnitudes of the light curve to the photometry at each observed epoch:

$$m_{3.6}(t) = I1(t), \quad m_{4.5}(t) = I2(t) \quad (2)$$

Offsets are found between the I1 and W1 photometry and, to a lesser extent, the I2 and W2 photometry (Fig. 4, also see Antoniucci et al. 2014). These are due to the different shapes of the filters (Fig. 1), especially the extended short wavelength wing of W1, and the different SEDs of the YSOs in this wavelength regime, as characterized in these plots by the Spitzer color. Given the scatter in these plots, we account for the differences between the Spitzer and WISE filters for each light curve individually by offsetting the W1 and W2 photometry to better align with the Spitzer photometry. The offset is determined from epochs of Spitzer photometry that are bracketed between two (NEO)WISE epochs. Using the (NEO)WISE photometry closest in time to the Spitzer point, either the unTimely and IRSAs data, as end points of a linear interpolation, we determine a W1 and W2 magnitude at the Spitzer epoch t , $W1_{int}(t)$ and $W2_{int}(t)$. The offset for each light curve is then determined by averaging the offsets between the Spitzer and interpolated NEOWISE photometry in that light curve,

$$\delta W1 = \frac{1}{n_{sp}} \sum_{i=1}^{n_{sp}} [I1(t_i) - W1_{int}(t_i)], \quad \delta W2 = \frac{1}{n_{sp}} \sum_{i=1}^{n_{sp}} [I2(t_i) - W2_{int}(t_i)], \quad (3)$$

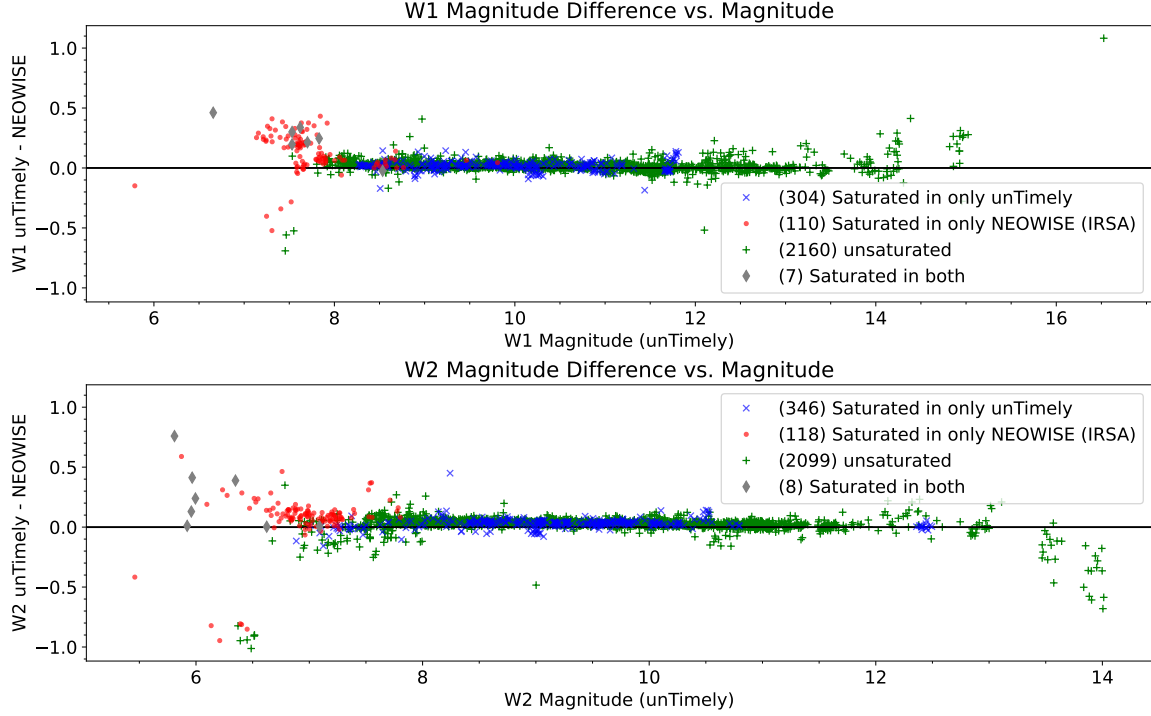


Figure 3. Difference between the NEOWISE photometry found in the IRSA and unTimely archives, with each point representing a matched set of unTimely and IRSA photometry for a specific source and epoch. These data are collected from all of the sources examined for variability in this work.

where n_{sp} is the number of Spitzer epochs bracketed by NEOWISE epochs, and $I1(t_i)$ and $I2(t_i)$ are the Spitzer photometry at those points. The (NEO)WISE photometry in that light curve are then determined using the offset:

$$m_{3.6}(t) = W1(t) + \delta W1, \quad m_{4.5}(t) = W2(t) + \delta W2. \quad (4)$$

These offsets are given for each light curve individually in the legends of the light curves (Figs. 5 - 8). We apply the same offset to the IRSA and unTimely photometry and plot both separately.

Each of the $4.5 \mu\text{m}$ curves includes a data point from the ISOCAM LW2 photometry. Here we use the offsets between the ISOCAM photometry and the I3, I4 and I_{comb} Spitzer magnitudes determined in Sec. 2.2. For the light curves, we use the middle of the three offset values, typically the offset from I_{comb} , to mark the data point and the maximum and minimum offsets to set the error bars. If the offsets are less than the MAD values in Table 1, we use the MAD values for the error bars instead. Since the I3 and I4 photometry used to cross-calibrate the ISO photometry are from the combined 2004 data in the SESNA or Spitzer Orion catalogs, we calculate the ISOCAM magnitude using

$$m_{4.5}(t_{ISO}) = [LW2 - I_{\text{spitzer}}] + I2_{2004}, \quad (5)$$

where $[LW2 - I_{\text{spitzer}}]$ is the offset between the ISO and Spitzer 2004 photometry obtained in Sec. 2.2 and $I2_{2004}$ is the $4.5 \mu\text{m}$ magnitude from the SESNA or Spitzer Orion catalogs (Sec. 2.1). Following the convention of Zakri et al. (2022), we then present the light curves in terms of delta magnitude,

$$\Delta m_{3.6}(t) = m_{3.6}(t) - \min(m_{3.6}), \quad \Delta m_{4.5}(t) = m_{4.5}(t) - \min(m_{4.5}), \quad (6)$$

where $\min(I1)$ and $\min(I2)$ are the minimum magnitudes of the $3.6 \mu\text{m}$ and $4.5 \mu\text{m}$ light curves, respectively. The values of these offsets are given in the legends of each light curves (Figs. 5 - 8).

3. RESULTS

In total, 221 sources have data from ISOCAM, Spitzer and NEOWISE spanning from 1997 to at least 2020. In Table 3, we list the 39 YSOs of these that show variations of at least a factor of two in flux, or 0.75 mag in either the

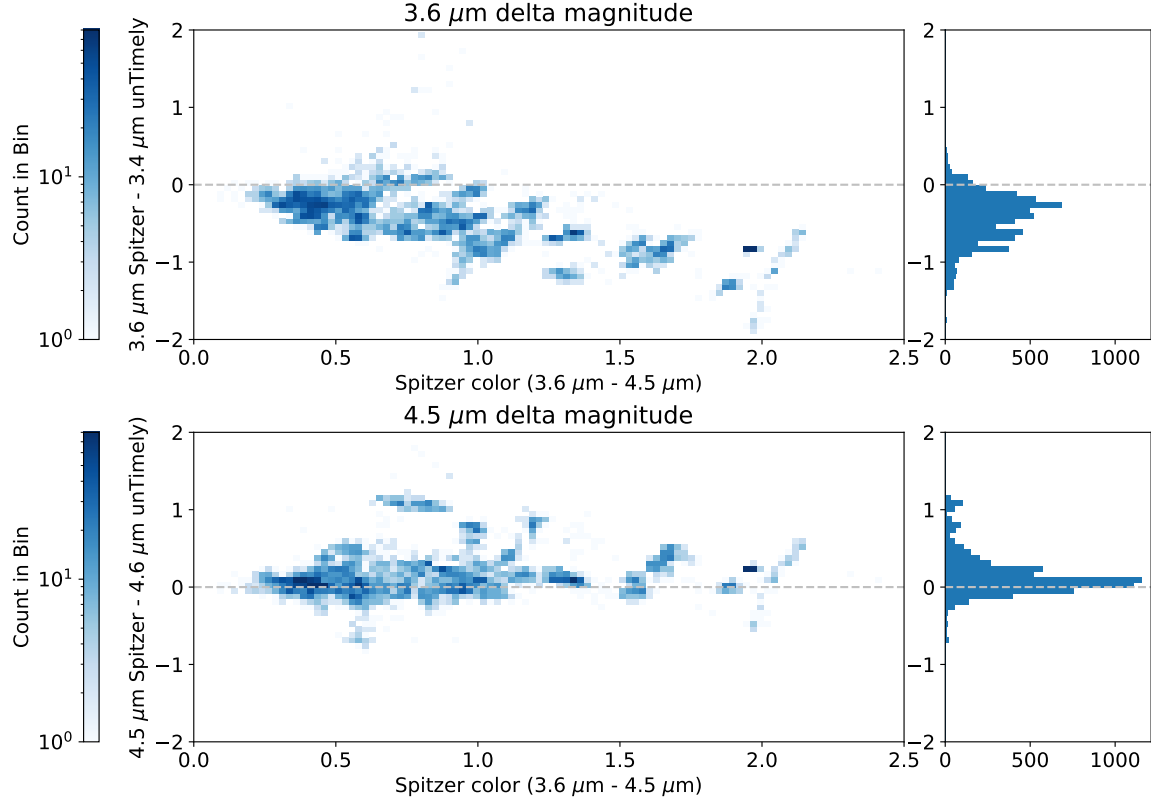


Figure 4. Offsets between concurrent Spitzer and unTimely photometry due to differences between the W1 and I1 bandpasses and between the W2 and I2 bandpasses as a function of the Spitzer $3.6 \mu\text{m} - 4.5 \mu\text{m}$ color. In total, 256 sources with ISOCAM photometry are used. Each epoch is considered independently, and distinct clusters of points are typically from a single source. In particular, the W1 and I1 magnitudes diverge for sources with large I1-I2 colors. In addition, there is significant scatter; this may be due to both the range of spectral shapes of the sources and variability between the WISE and Spitzer epochs.

3.6 or $4.6 \mu\text{m}$ light curves, as measured between their minimum and maximum Δm values. This threshold is applied to focus on the multi-decade, large-amplitude variations that can be studied with this combined data set. In Table 3, we tabulate the source name, RA and Dec., the star-forming region in which the YSO is located, the 2004 $3.6 \mu\text{m}$ and $4.5 \mu\text{m}$ magnitudes from Spitzer, and the SED class. This class was determined from the Spitzer photometry (Gutermuth et al. 2009; Kryukova et al. 2012; Megeath et al. 2012) or by the combined 2MASS+Spitzer+Herschel+sub-mm photometry in the case of protostars (Furlan et al. 2016; Pokhrel et al. 2023). We also note sources with high cadence Spitzer data from YSOVAR or other programs and include identifiers used in the Park et al. (2021) paper and other commonly used names. Thirteen of these have NEOWISE photometry out to the final unTimely data point in 2020; the remainder have IRSAs photometry that extends to 2024. In Table 3 we also include an additional protostar located in the Orion B cloud, J05473657+0020062, which has ISOCAM and Spitzer data, but no (NEO)WISE data. We exclude this source from most of our analysis.

For each source, the table also includes the maximum Δm values of the 3.6 and $4.5 \mu\text{m}$ light curves and a classification based on the light curves. We classify the YSOs into four provisional categories: completed bursts, ongoing bursts, fades, and fluctuators, which we define in the following sections. Many of the light curves show combinations of traits that can defy simple classification, and we will discuss the relationships between these categories in Sec. 4.

Table 3. Table of Large-Amplitude Variables

Name	RA (deg)	Dec (deg)	Region	3.6 μm ¹ Mag.	4.5 μm ¹ Mag.	3.6 Range	4.5 Range	Var. Class	SED Class	YSO VAR	Alt. Name ²
J03283708+3113309	52.1545	31.2252	N1333	9.85	7.96	1.51	1.88	Fade	Proto.	N	D2375, eHOPS-per-15, EES2009 Per-emb 35
J03290473+3111349	52.2697	31.1930	N1333	11.91	10.99	0.50	0.76	Fade	Disk	Y	D2433, GMM2008 85
J03285955+3121467	52.2481	31.3630	N1333	8.88	8.43	1.30	1.13	Fluc.	Disk	Y	D2418, EM* LkHA 353
J03283452+3107055	52.1438	31.1182	N1333	12.04	10.51	1.38	1.09	Fluc.	Proto.	N	D2372, eHOPS-per-13, GMM2008 14
J03285102+3118184	52.2126	31.3051	N1333	8.39	7.89	0.99	1.19	Fluc.	Disk	Y	D2390, GMM2008 50
J03292042+3118343	52.3351	31.3095	N1333	8.54	7.99	0.89	0.89	Fluc.	Disk	Y	D2473, HH 17
J03284529+3105419	52.1887	31.0950	N1333	13.19	11.95	0.77	0.73	Fluc.	Proto.	N	D2384, eHOPS-per-20, IRAS 03256+3055
J03285120+3119549	52.2133	31.3319	N1333	9.06	8.71	0.64	0.82	Fluc.	Disk	Y	D2392, GMM2008 52
J03285216+3122453	52.2174	31.3793	N1333	10.16	9.87	0.64	0.92	Fluc.	Disk	Y	D2396, GMM2008 54
J05362461-0622413	84.1025	-6.3781	Ori. A	9.37	6.95	1.69	2.52	Burst	Proto.	N	M933, H178
J05461313-0006045	86.5547	-0.1013	Ori. B	5.96	4.84	3.44	3.21	Burst	Proto.	N	M3180, H388, V1647 Ori, McNeil's Nebula
J05462569+0023416	86.6071	0.3949	Ori. B	8.61	8.01	1.55	1.66	Burst	Disk	N	M3394
J05460477-0014163	86.5199	-0.2379	Ori. B	7.22	6.30	1.02	0.92	Fluc.	Proto.	N	H385, IRAS 05435-0015
J05473657+0020062	86.9024	0.3351	Ori. B	7.84	7.04	0.57	1.38	Burst	Proto.	N	M3341, H364
J05465358+0000061	86.7232	0.0017	Ori. B	8.77	8.21	1.64	1.62	Fade	Disk	N	M3196
J05464312+0000525	86.6797	0.0146	Ori. B	6.39	5.19	0.51	1.03	Fade	Proto.	N	M3208, H363
J05460363-0014492	86.5151	-0.2470	Ori. B	9.14	7.63	1.83	1.16	Fluc.	Proto.	N	M3159, H315
J05405172-0226486	85.2155	-2.4468	Ori. B	8.22	7.58	1.16	0.98	Fluc.	Proto.	N	M2827, H294
J05413972-0202241	85.4155	-2.0400	Ori. B	9.46	9.03	1.18	1.15	Fluc.	Disk	N	M2873
J05471062+0021141	86.7942	0.3539	Ori. B	7.77	6.61	0.92	0.74	Fluc.	Proto.	N	M3359, H365
J05455630+0007085	86.4846	0.1190	Ori. B	10.12	9.91	0.95	1.23	Fluc.	Disk	N	M3264
J05415555-0223405	85.4815	-2.3946	Ori. B	10.00	9.52	0.83	1.15	Fluc.	Disk	N	M2829
J05464741+0012594	86.6975	0.2165	Ori. B	10.19	9.75	0.84	0.93	Fluc.	Disk	N	M3295
J16271758-2405139	246.8233	-24.0872	Oph.	8.32	7.78	2.14	2.28	Burst	Disk	N	D2206, ISO-Oph 123
J16271383-2443318	246.8076	-24.7255	Oph.	9.20	8.71	1.45	1.34	Burst	Disk	N	D2197, ISO-Oph 117
J16264216-2431031	246.6757	-24.5175	Oph.	9.43	8.75	1.05	1.2	Burst	Disk	N	D2154, ISO-Oph 59
J16265196-2430396	246.7165	-24.5110	Oph.	10.77	9.78	0.66	1.03	Fade	Disk	N	D2162, ISO-Oph 75
J16272180-2429536	246.8408	-24.4982	Oph.	6.94	5.72	2.01	2.72	Fluc.	Proto.	Y	eHOPS-oph-24, ISO-Oph 134
J16264421-2434487	246.6842	-24.5802	Oph.	7.67	6.01	1.99	1.79	Fluc.	Proto.	N	D2156, eHOPS-oph-9, ISO-Oph 65
J16274162-2446450	246.9234	-24.7792	Oph.	11.33	10.3	0.99	0.93	Fluc.	Proto.	N	D2246, eHOPS-oph-38, ISO-Oph 170
J16264048-2427146	246.6687	-24.4541	Oph.	9.91	9.04	0.85	1.03	Fluc.	Proto.	N	D2151, eHOPS-oph-7, ISO-Oph 54
J16262755-2441538	246.6148	-24.6983	Oph.	8.95	8.67	0.80	1.06	Fluc.	Disk	N	D2146, ISO-Oph 43
J16274709-2445353	246.9462	-24.7598	Oph.	9.54	8.93	0.65	0.98	Fluc.	Disk	N	D2254, ISO-Oph 177
J18300772+0112044	277.5321	1.2012	Serp.	8.96	8.48	0.46	0.83	Burst	Disk	Y	D2951, GMM2008 Serpens 84
J18295117+0116404	277.4632	1.2779	Serp.	10.00	8.69	1.52	1.72	Fluc.	Proto.	Y	D2876, eHOPS-agl-68, EES2009 Ser-emb 21
J18295954+0111583	277.4981	1.1995	Serp.	9.04	7.30	1.00	1.11	Fluc.	Proto.	Y	D2926, eHOPS-agl-88, EES2009 Ser-emb 24
J19025867-3707361	285.7444	-37.1267	CrA	11.44	10.04	0.56	1.02	Fade	Proto.	N	D1715, eHOPS-cra-10, GMM2009 CrA 2
J19001555-3657578	285.0648	-36.9660	CrA	13.65	12.00	0.99	1.07	Fluc.	Disk	N	D1676, ISO-CrA 76
J11094191-7634585	167.4246	-76.5829	Cham.	8.58	7.98	1.30	1.09	Fluc.	Disk	Y	D1608, ISO-ChaI 199
J11095438-7631114	167.4766	-76.5198	Cham.	11.23	10.38	1.09	0.80	Fluc.	Proto.	Y	D1617, eHOPS-cha-9, ISO-ChaI 225

¹This photometry comes from Megeath et al. (2012) or Megeath et al. (2016) for the Orion sources and from the SESNA catalog for the remainder of the regions (Pokhrel et al. 2020).

²Alternative names starting with M and D are from Park et al. (2021) paper and refer to sources from Megeath et al. (2012) and Dunham et al. (2015), respectively. Names starting with H are HOPS sources from Furlan et al. (2016). GMM2008 sources are from Gutermuth et al. (2008) and GMM2009 sources are from Gutermuth et al. (2009). eHOPS sources are from the eHOPS catalog on IRSA <https://irsa.ipac.caltech.edu/data/Herschel/eHOPS/overview.html>, also see (Pokhrel et al. 2023). EES2009 sources are from Enoch et al. (2009). ISO-Oph, ISO-CrA, and ISO-ChaI source are from Bontemps et al. (2001), Olofsson et al. (1999), and Persi et al. (2000), respectively.

3.1. Completed Bursts

Completed bursts are defined by i.) a decrease in Δm of ≥ 0.75 mag after the initial ISOCAM measurement (an increase of $\geq 2\times$ in flux), ii.) a sustained interval of low Δm (high flux) that lasts > 5 yrs, and iii.) a return in the Δm to a value close to or below the initial ISOCAM value by the final epoch of the light curve. We have identified four such completed bursts in the 27-year time span of our data (Fig. 5): the flat spectrum protostar J05461313-0006045 in the Orion B cloud, the pre-main sequence star with disk J05462569+0023416 also in Orion B, and the pre-main sequence stars with disks J16264216-2431031 and J16271758-2405139 in the Ophiuchus cloud.

The outburst of J05461313-0006045 began in the fall of 2003 (McNeil et al. 2004; Briceño et al. 2004). Also known as V1647 Ori (Samus 2004) and HOPS 388 (Furlan et al. 2016), the protostar shows a flat spectrum SED consistent

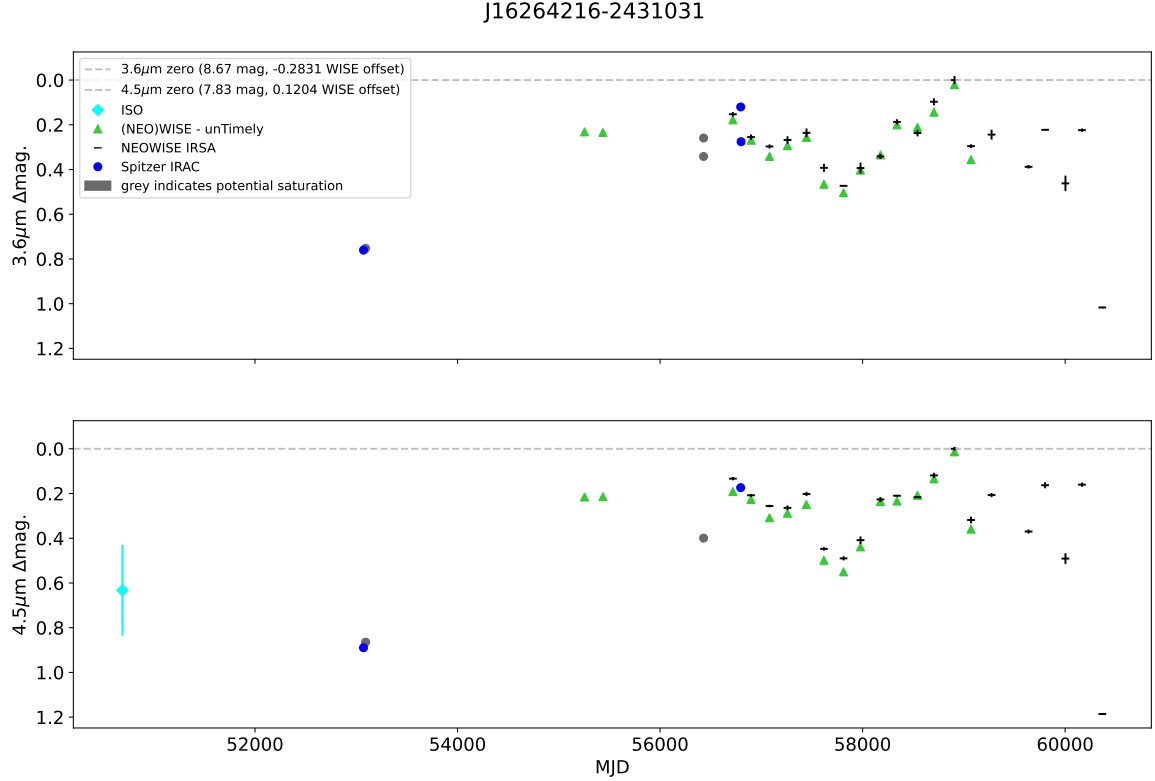


Figure 5. The 3.6 and $4.5 \mu\text{m}$ light curves of the completed bursts. We label the sources of the photometry in legend. Data that may be affected by saturation are shown with a grey color. The legends also contain the Spitzer magnitudes corresponding to $\Delta m = 0$, and the offsets added to the (NEO)WISE magnitudes to align those better to the Spitzer photometry.

with a more evolved protostar (Muzerolle et al. 2005; Flaherty et al. 2016). An ISOCAM, Spitzer, and (NEO)WISE light curve for J05461313-0006045 was presented by Kulkarni et al. (2024) which included $3.6 \mu\text{m}$ and $4.5 \mu\text{m}$ IRAC subarray photometry not included in our light curve. Kulkarni et al. (2024) found an amplitude for the burst of 3.1 mag at $4.5 \mu\text{m}$ and a duration of 16 years, using the I-band light curve to establish the time of the outburst (Briceño et al. 2004). During its burst, J05461313-0006045 (V1647 Ori) shows ~ 1 mag variations, as also found by Kulkarni et al. (2024). At visible wavelengths, it underwent a large decline in 2006 before returning to the previous level in 2008. This dip was not sampled in our $3\text{-}8 \mu\text{m}$ light curves, and we do not know its depth in our wavelength range.

The remaining three completed bursts do not have independent measurements of their bursts in other wavelength bands. This limits our ability to determine when and how quickly they rose. J05462569+0023416 and J16271758-2405139 show a rise between the ISOCAM 1997 epoch and the first Spitzer/IRAC 2004 epoch while J16264216-2431031 shows a rise between Spitzer/IRAC 2004 epoch and the first WISE epoch. For J05462569+0023416, the initial Δm is lower than the post-burst values; this suggests either different pre- and post-outburst accretion luminosities, or that the ISOCAM measurement caught this burst during its rise. During the bursts, the sparsely sampled light curves of J05462569+0023416 and J16271758-2405139 show modest variations of < 0.5 mag, while J16264216-2431031 shows 0.5-0.75 mag multi-year fluctuations. All four YSOs show rapid declines in flux from their burst phases to the post-burst phases that last less than 2 years, and less than 6 months in the case of J16264216-2431031. In the post-burst phase, the NEOWISE photometry shows continued variability as high as 1 mag for J05461313-0006045.

3.2. Ongoing Bursts

Ongoing bursts are defined by i.) a decrease in Δm of ≥ 0.75 mag after the ISOCAM measurement followed by ii.) a sustained low magnitude (high flux) through the final epoch of our light curves. We have identified three ongoing bursts in our sample (Fig. 6). These are the protostar J05362461-0622413, a Class I protostar in the Orion A cloud, also known as HOPS 178 (Furlan et al. 2016), and the pre-main sequence stars with disks J16271384-2443318 in the Ophiuchus cloud and J18300772+0112044 in the Serpens Main cluster.

J16271383-2443318

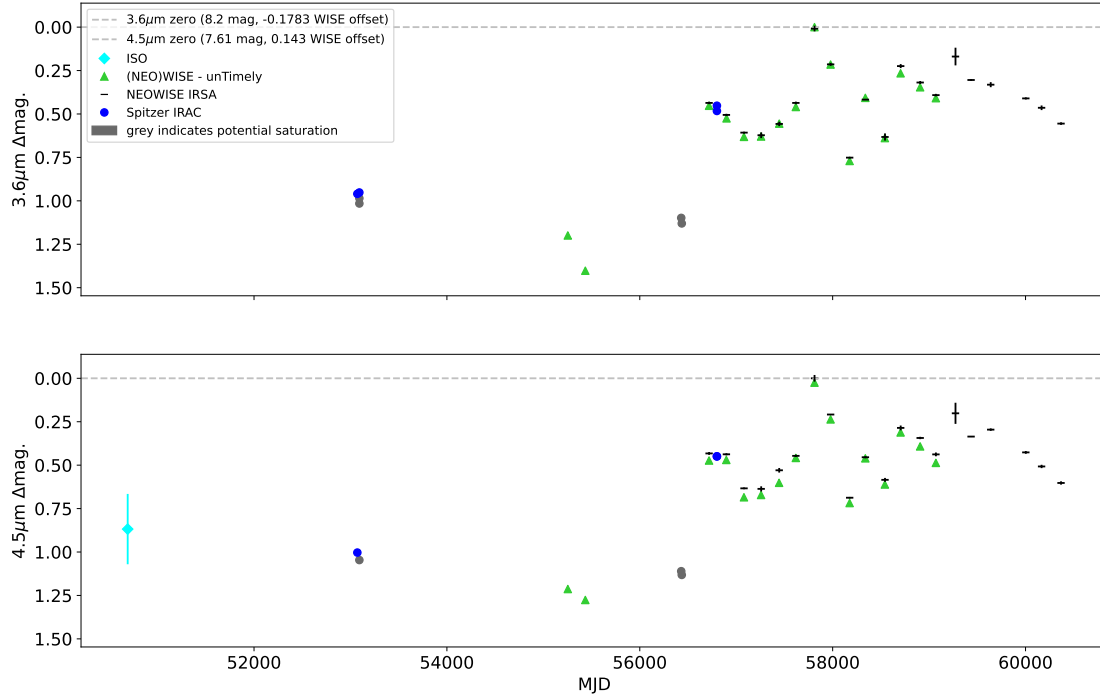


Figure 6. The 3.6 and $4.5 \mu\text{m}$ light curves of the ongoing bursts. We label the sources of the photometry in legend. Data that may be affected by saturation are shown with a grey color. The legends also contain the Spitzer magnitudes corresponding to $\Delta m = 0$, and the offsets added to the (NEO)WISE magnitudes to align those better to the Spitzer photometry.

The pre-ms star J18300772+0112044 rises between the ISOCAM 1997 epoch and the first Spitzer/IRAC 2004 epoch. There is evidence of slower, multi-year rises for the remaining two YSOs. For the protostar J05362461-0622413, the 2004 Δm is between the pre-burst and burst levels, suggesting a slow rise over 1-2 decades. For the pre-main sequence star J16271382-2443316, the burst occurs between the WISE (2010) and NEOWISE (2013) points and takes 6 years to reach the burst maximum. The NEOWISE photometry captures part of this rise, and shows that it is not monotonic.

In all three of these cases, the sustained burst phase shows significant variability. The protostar J05362461-0622413 undergoes a 0.75 mag dimming between 2010 and 2013, after which there is lower amplitude variability. The pre-ms star with disk J16271384-2443318 shows 0.5-0.75 mag multi-year fluctuations after the onset of its burst. The pre-ms star with disk J18300772+0112044 underwent a slow dip in flux and then a rise from 2004-2015, although the data is sparsely sampled. In total, the data show that the burst phase is characterized by multi-year variability that can be a significant fraction of the amplitude of the burst.

Finally, we found one additional ongoing burst, J05473657+0020062 or HOPS 364, which rises slowly between 1997 and 2017. For this source, all the (NEO)WISE data has been rejected by the filters, and hence we do not include this source in our analysis. The light curve is shown in Fig. 12 of Appendix A.

3.3. Fading YSOs

Fading sources, or fades, are defined by i.) an initial low magnitude (high flux) level, ii.) a subsequent increase in Δm of ≥ 0.75 mag across the light curve, and iii.) no return to the initial high flux level by the final epoch. We find three fading protostars and three fading pre-main sequence stars with disks (Fig. 7). In the NGC 1333 cluster, the J03283708+3113309 protostar and pre-ms star J03290473+3111349 are observed to fade. In Orion B, the protostar J05464312+0000525 (HOPS 363) and the pre-ms star J05465357+0000061 are observed to fade. In Ophiuchus and Corona Australis, the pre-ms star J16265196-2430396 and protostar J19025867-3707361, respectively, show fades.

The fades of J03283708+3113309, J03290473+3111349 and J05464312+0000525 show a gradual decline over 15 years, although J03290473+3111349 and J05464312+0000525 show significant (~ 0.5 mag) variability in the NEOWISE data, with a rise in flux in the last few epochs. The pre-ms star J05465357+0000061 shows a rapid decline in flux over two

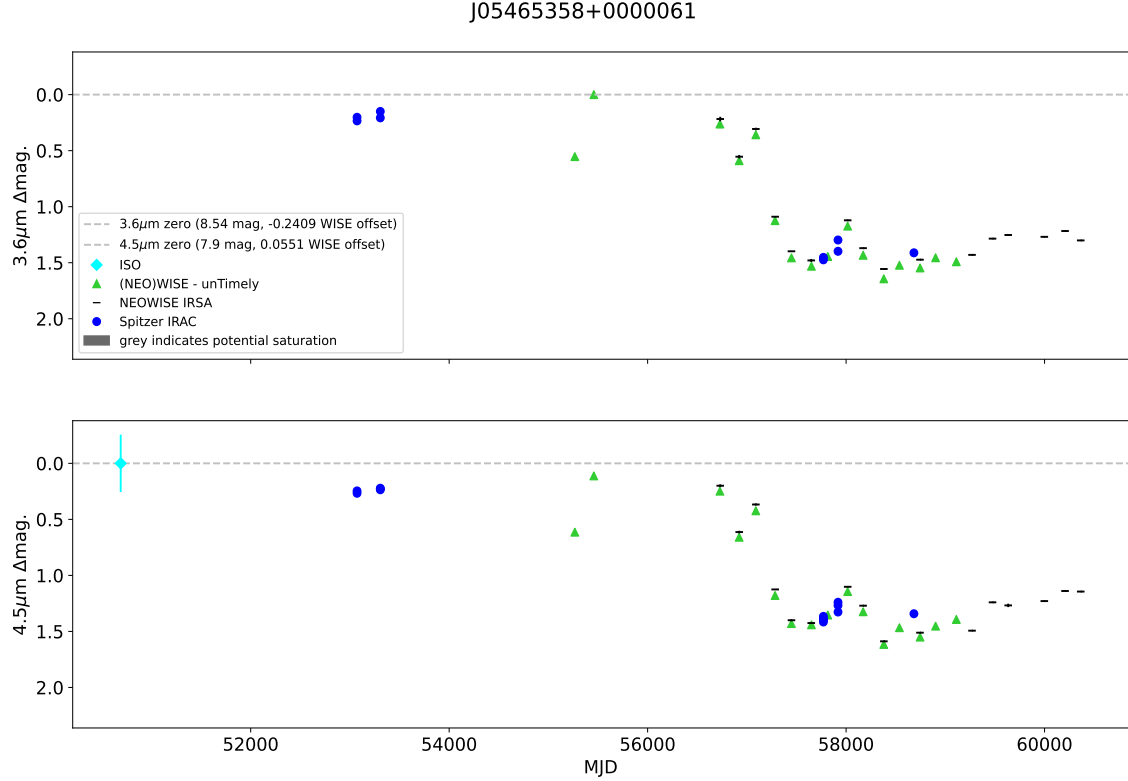


Figure 7. The 3.6 and $4.5 \mu\text{m}$ light curves of the fading YSOs. We label the sources of the photometry in legend. Data that may be affected by saturation are shown with a grey color. The legends also contain the Spitzer magnitudes corresponding to $\Delta m = 0$, and the offsets added to the (NEO)WISE magnitudes to align those better to the Spitzer photometry.

years, similar to the declines of the completed bursts in Sec. 3.1. The pre-ms star J16265196-2430396 shows a slow decline in flux over 15 years, and then a rapid decline in flux. Finally, J19025867-3707361 shows a large decline in flux between 1997 and 2004 where there is no data to sample the shape of the decline. In total, these show that the fades can be either slow or rapid, and they can exhibit significant variability superimposed on top of the overall fading.

3.4. *Fluctuating YSOs*

The category of fluctuators is defined by i.) the presence of large fluctuations in magnitude with values of $\Delta m \geq 0.75$ mag over time intervals of < 5 years, and ii.) no evident sustained burst or fade. We find 26 such YSOs that we classify as fluctuators; 13 are protostars and 13 are pre-main sequence stars with disks (Fig. 8.)

This category encompasses a wide range of behaviors. Many fluctuating YSOs show large, poorly sampled fluctuations on < 1 year time intervals as shown in the NEOWISE or Spitzer YSOVAR data. Rapid variations are often apparent in the YSOVAR data; the most extreme example is J18295225+0115476 which shows a 1.5 mag variation over the YSOVAR data that spans 35 days. A few fluctuators show coherent, fluctuating behavior on multi-year to decade intervals. The pre-ms star J03292042+3118343 shows two sharp peaks in flux separated by about 13 years. Three peaks are evident for J05405172-0226486, J03284529+3105419 and J16274709-2445353; periods of 4.4 and 5.0 yrs, respectively, were found by Park et al. (2021) for the last two of these sources in the NEOWISE light curves. Rises, potentially suggestive of non-monotonically increasing bursts, are possible for J05460363-0014492, J16274709-2445353, and J16262755-2441538. J16262755-2441538 in particular exhibits a clear rise and may be a slow outburst, but it decays in flux in its last epochs. In all three cases, the variations are more than half the putative burst amplitude. Finally, J05471062+0021141 does not show rapid variations, and it could be categorized as a fading YSO if not for the steep rise during the last three unTimely epochs.

The fluctuators are more likely to contain data from the high-cadence Spitzer observations, either from the YSOVAR program or the study of Chameleon by Flaherty et al. (2016). While 1/7 bursts and 1/6 fades have YSOVAR data, 10/26 of the fluctuators have high cadence data. All ten of the fluctuators with high-cadence data would have

J03285216+3122453

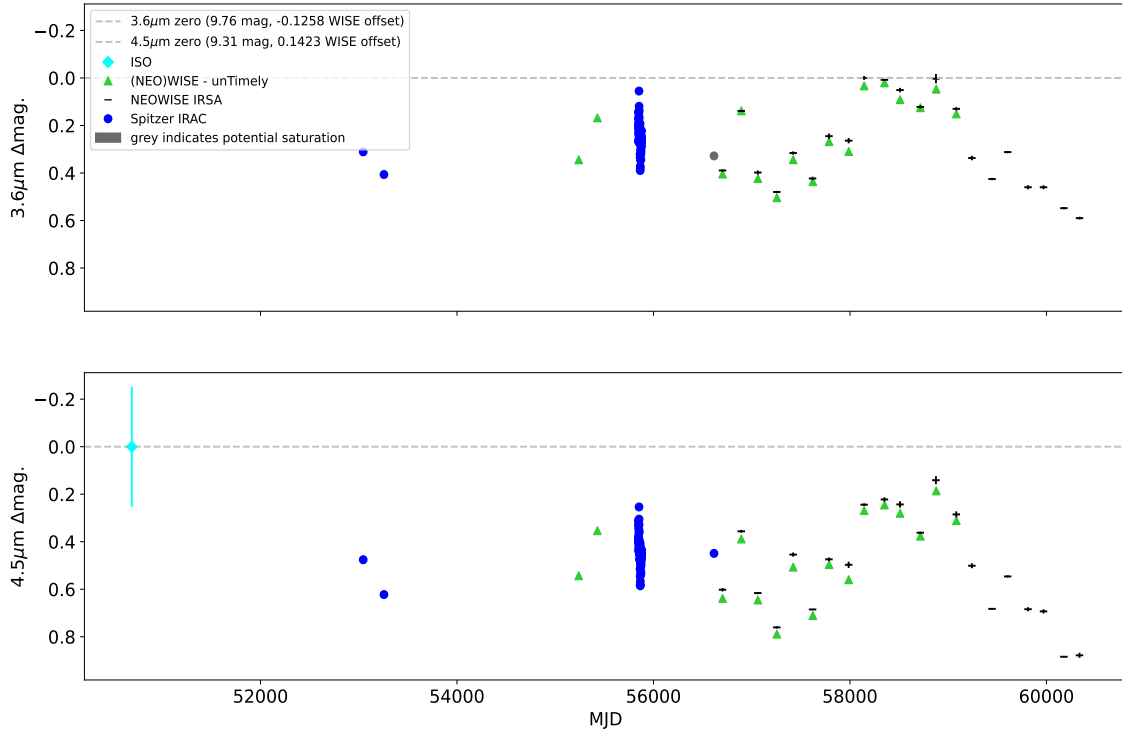


Figure 8. The 3.6 and $4.5 \mu\text{m}$ light curves of the fluctuators. We label the sources of the photometry in legend. Data that may be affected by saturation are shown with a grey color. The legends also contain the Spitzer magnitudes corresponding to $\Delta m = 0$, and the offsets added to the (NEO)WISE magnitudes to align those better to the Spitzer photometry.

been identified as fluctuators without that data on the basis of the NEOWISE data. Future work will explore how the inclusion of high-cadence observations biases the classification of the light curves.

3.5. Δt vs Δm Diagrams

To compare the timescales of the variability present in our different categories, we use Δt vs Δm plots (Mahabal et al. 2011; Findeisen et al. 2015; Guo et al. 2021; Ryan et al. 2025); which are related to the structure function (Findeisen et al. 2015; Terebey et al. 2016). We plot $|\Delta t|$ vs $|\Delta m|$ for each pair of points in the $4.5 \mu\text{m}$ light curve (Fig. 9). We combine the values of each pair of points from all the light curves within a given category. Over the irregular and sparse sampling of the light curve, these diagrams show the observed variation in magnitude over five orders of magnitude in time lag, from 0.1 days to 27 years. This large dynamic range in time comes from the different data sets used in this work; the YSOVAR data dominate for $|\Delta t| < 100$ days, the (NEO)WISE and Spitzer photometry dominate the $|\Delta t| = 100 - 10000$ day range, and data paired with the ISOCAM photometry contributes to the $|\Delta t| = 1000 - 10000$ day range.

Dividing the diagrams into three bins, < 100 days, $100 - 1000$ days, and > 1000 days, we find that there is an increase in $|\Delta m|$ with $|\Delta t|$. For all four categories, the largest values of $|\Delta m|$ occur for $|\Delta t| \geq 1000$ days. For the completed bursts, ongoing bursts, and fades, only $|\Delta t| > 100$ days values show 90th percentile of $|\Delta m| > 0.75$ mag (i.e. a factor of 2 change in flux). For the fluctuators, the $|\Delta t| < 100$ days bin has one pair of points with $|\Delta m| > 0.75$ mag, and there are many pairs close to this value. Higher amplitudes in the $3-5 \mu\text{m}$ variability at longer timescales were also found in a Spitzer and WISE study by Lee et al. (2024).

We also show the 90th percentile values of $|\Delta m|$ for the three bins. Both the completed bursts and fades show amplitudes at lags of > 1000 days that are a factor of two times higher in magnitude (i.e. a factor of 6 higher in flux) than those at shorter lags. For the ongoing bursts, the 90% limit of the > 1000 days bin is lower than that of the $100 - 1000$ days bin. This is due to the large number of points in the YSOVAR data of J18300772+0112044 that were located in the middle of burst; they are evident as a dense cluster of points in that plot (Fig. 9). For both

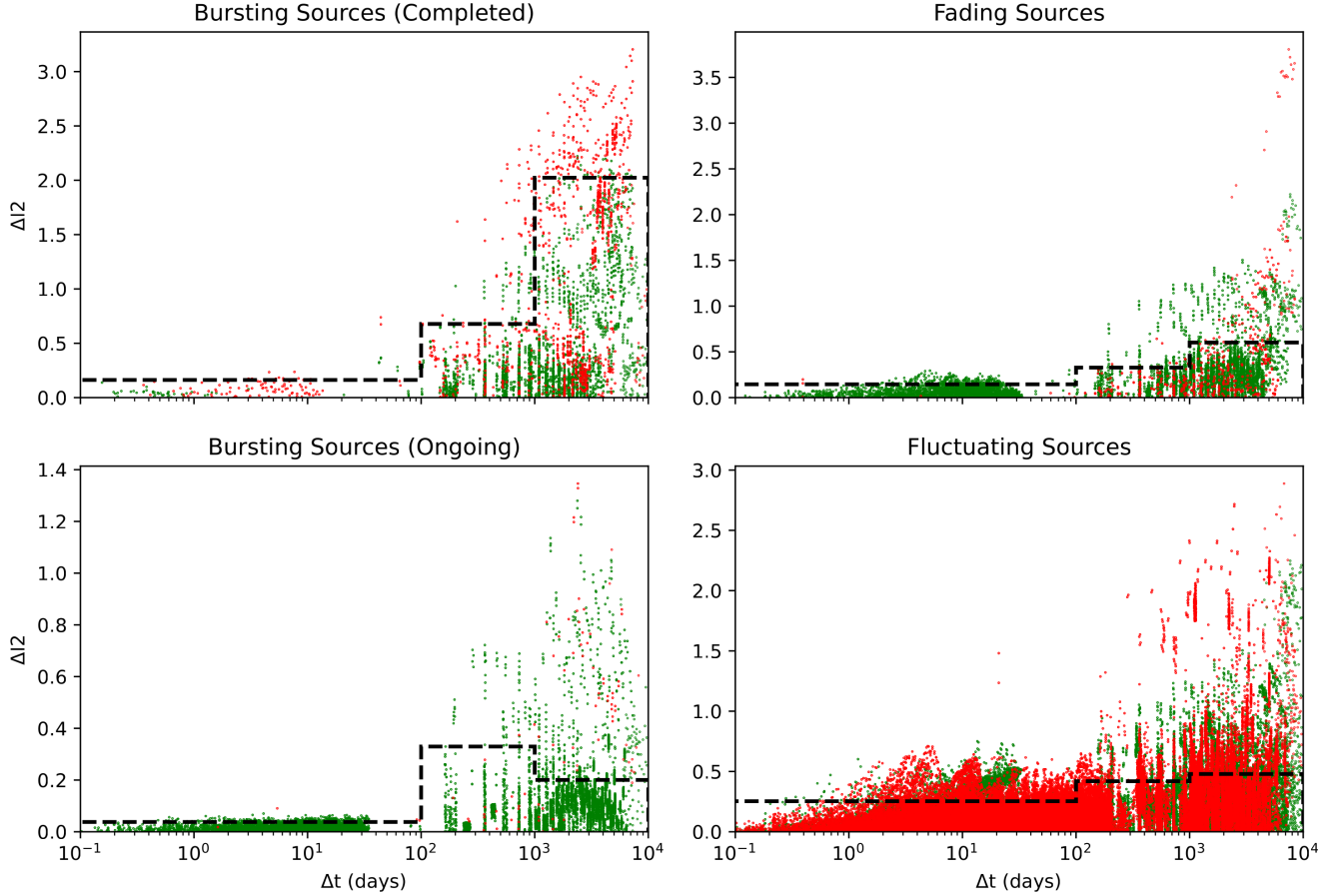


Figure 9. The $\Delta m_{4.5 \mu m}$ vs. Δt diagrams for the ISO, Spitzer and WISE data of all of the large-amplitude variables. These are separated into the four different categories, with protostars (red) and pre-ms stars with disks (green) distinguished by color. The dashed lines shows the 90th percentile of Δm for bins of 10^3 - 10^4 days, 10^2 - 10^3 days, and $< 10^2$ days.

the bursts and fades, the 90% limit for the < 100 days bin is very low (≤ 0.2 mag). Finally, the 90% limit for the fluctuators has the highest value out of all the categories in the < 100 days bin, with only a factor of two change in magnitude between them and those in the > 1000 day bin. Furthermore, the 90% limits of the $100 - 1000$ days bin and > 1000 days bin are similar. The fluctuators show the lowest degree of change across the three bins, indicating that significant variability is observed across all sampled time intervals.

3.6. Color Plots and the Role of Extinction

Colors are a diagnostic of the processes responsible for variability and, in particular, whether changes in extinction are responsible for changes in the brightness (e.g. Hillenbrand et al. 2019; Park et al. 2021). In Fig. 10, we show the Spitzer I1-I2 and WISE W1-W2 colors for the light curve of the protostar J16274709-2445353. In addition, we plot color-magnitude diagrams (hereafter: CMDs) showing the I1-I2 color vs the I2 magnitude for each point in the light curve of this protostar from the Spitzer data, and the W1-W2 color vs the W2 magnitude for each point in the light curve from the (NEO)WISE photometry. We split the Spitzer and (NEO)WISE data since differences in the Spitzer/IRAC and WISE bandpasses can result in large differences in color (see Fig. 1 for the bandpass profiles). We plot extinction vectors in the CMDs; this gives the direction of changes in the color and magnitude due to extinction. For the I1-I2 vs I2 plots, we use the tabulation of extinction laws from Chapman et al. (2009). We adopt their tabulated $1 < A_K \leq 2$ and Flaherty et al. (2007) laws; the Chapman et al. (2009) $A_K \geq 2$ law is between the two, and the laws for lower extinctions have high uncertainties and higher slopes. For the W1-W2 vs W2 CMDs, we adopt the $0.5 < A_K \leq 1$ and $A_K > 1$ extinction laws from Koenig & Leisawitz (2014). In each CMD, we plot two vectors showing

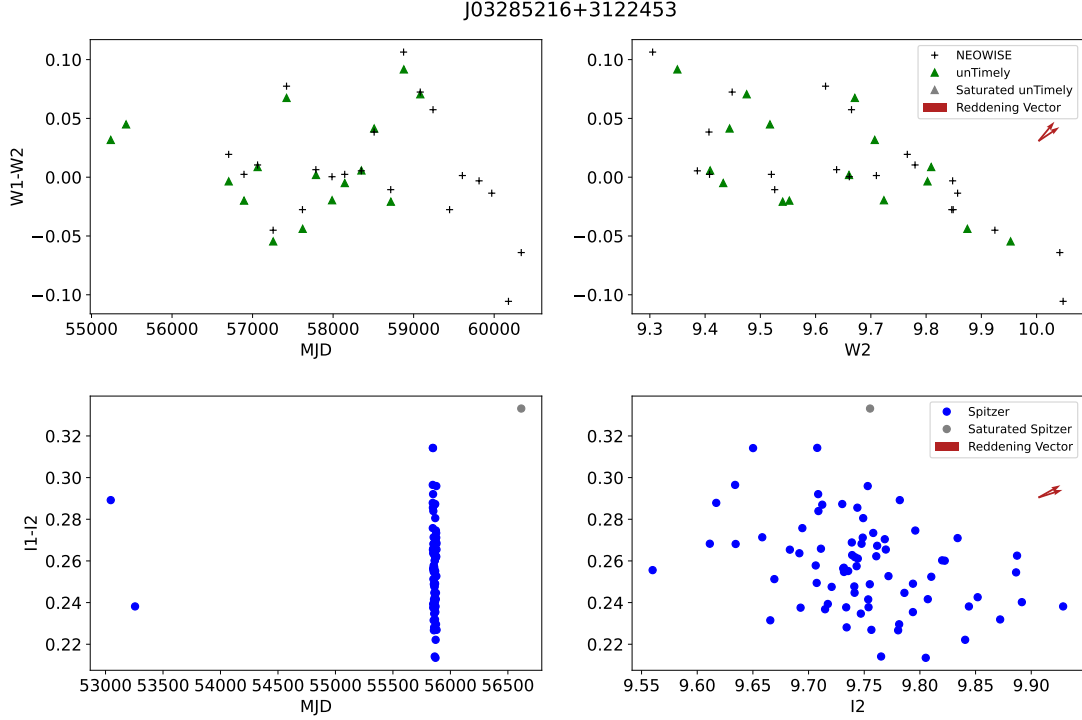


Figure 10. Left panels: color vs MJD plots; the WISE photometry is in the top panel and the Spitzer photometry is in the bottom panel. The time range covered in the plots is different. Right panels: color vs $4.5 \mu\text{m}$ mag plots. On the top row, we display the (NEO)WISE $W1-W2$ vs $W2$ diagram, while on the bottom row we show the Spitzer $I1-I2$ vs $I2$ diagram. For comparison, extinction vectors are shown for both of these plots to show the direction that extinction would shift the photometry. In the WISE plots, we show the IRSA and unTimely data separately. We also mark points that may be affected by saturation.

the different extinction laws for the moderate and high extinction regimes. The overall distribution of points in the CMDs are not aligned with these vectors, which suggests that the variations in magnitude are not due to changes in extinction.

To further assess whether changes in magnitude are consistent with variations in extinction, we calculate the $\Delta(I1 - I2)/\Delta I2$ and $\Delta(W1 - W2)/\Delta W2$ slopes for each pair of photometry points in the CMDs. We plot $|\Delta I2|$ or $|\Delta W2|$ vs these slopes in Fig. 11, comparing them to the slopes of the extinction laws used in the CMDs. For small values of $|\Delta I2|$ or $|\Delta W2|$, the slopes become dominated by the uncertainties in the colors, and the distributions spread out in slope. For variations due to extinction, we expected that the slope will be positive, i.e. increases in the $I2$ or $W2$ magnitudes will be accompanied by increasingly red colors. We find that for the bursts and fades, the points are concentrated at neutral to negative slopes for $|\Delta I2|$ and $|\Delta W2| > 0.75$ mag, ruling out reddening for most of the points. For the Spitzer data, we do find a chain of points that have the same slope as the reddening vector. On inspection of the light curve, these slopes are for non-sequential pairs of points obtained before and after the decline of the completed burst of the J05461313-0006045 protostar, and they do not seem to be following the extinction vector. We also find that for the fluctuators, slopes are concentrated at neutral to positive values, similar to the bursts and fades. Most are not consistent with extinction, although there is more scatter in these diagrams than for the bursts and fades, and there could be a prominent, but not dominant, component of the variability due to extinction.

4. DISCUSSION

In this section, we discuss the classification of protostars into the four different types of variability and assess whether they represent fundamentally different types of variability or whether they are simply the result of the sampling of our data. We then explore the implications of our work for the mechanisms responsible for YSO variability.

4.1. Classification of Accretion-Driven Outbursts

This program was initially motivated by the goal of identifying large-amplitude, accretion-driven outbursts from YSOs in the nearest 500 pc. Such outbursts, although rare, have long been thought to play an important role in mass

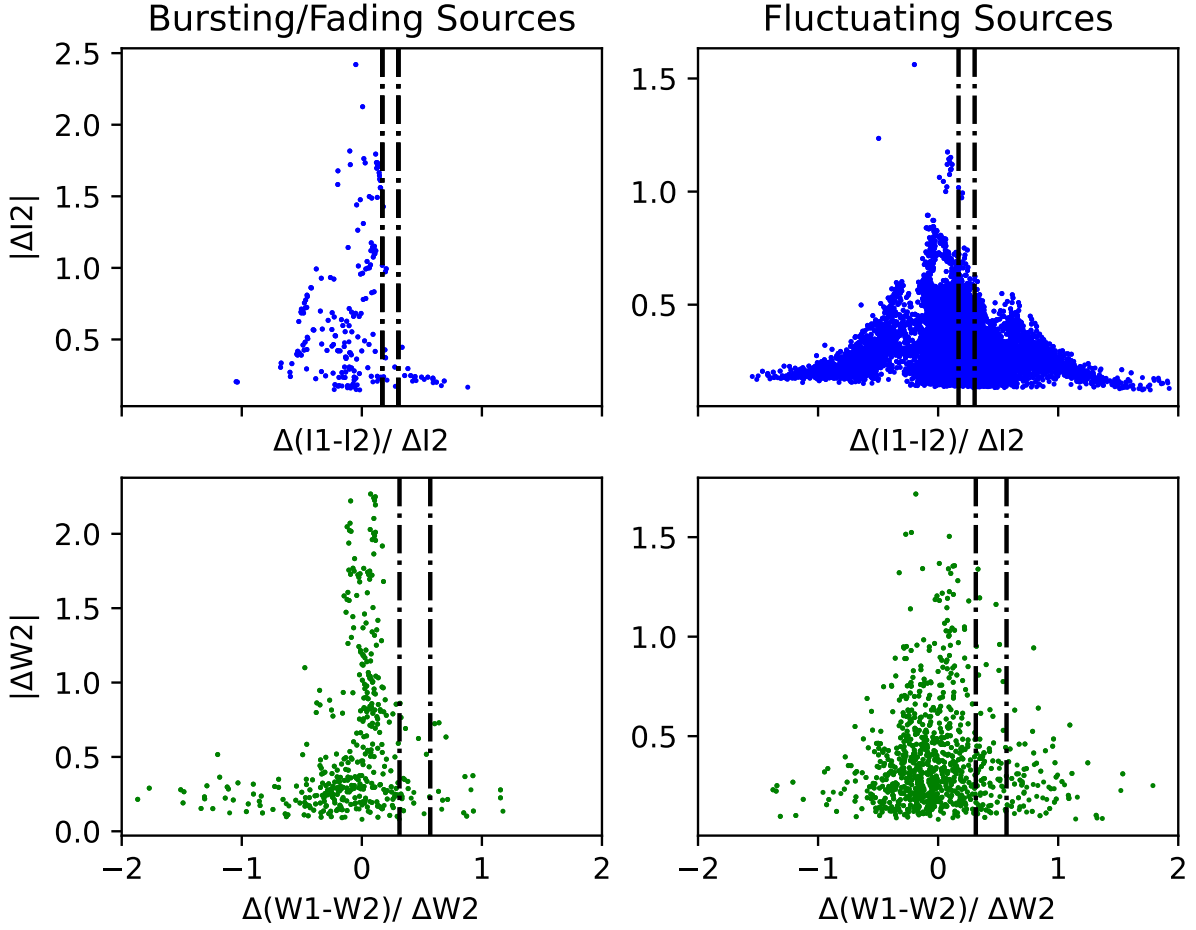


Figure 11. The change in magnitude vs the slopes between pairs of points in the CMDs. **Top:** $|\Delta I_2|$ vs $\Delta(I_1 - I_2)/\Delta I_2$ plots for the combined bursts and fades (left panel) and fluctuators (right panel). The vertical lines mark the slopes of the molecular cloud extinction laws for the Spitzer filters (Flaherty et al. 2007; Chapman et al. 2009); points found on or between these lines have the slopes bracketed by the extinction vectors in the CMD described in the text. **Bottom:** $\Delta(W_1 - W_2)/\Delta W_2$ vs $|\Delta W_2|$ plots for the combined bursts and fades (left panel) and fluctuators (right panel). Here the lines show the slopes for the extinction law found for the WISE filters for regions of moderate (right) and high (left) extinction (Koenig & Leisawitz 2014); points on or between these lines are consistent with changes due to extinction.

accretion (Hartmann & Kenyon 1996; Dunham et al. 2010a). YSO outbursts were historically divided into luminous, decades-long FU Ori outbursts and lower-amplitude EX Lupi outbursts that lasted one year or less (Fischer et al. 2022). These two categories show distinct spectroscopic signatures that imply different modes of accretion (Hartmann et al. 2016). EX Lupi outbursts exhibit bright hydrogen emission lines indicative of magnetospheric accretion, i.e. accretion from the disks to the stars via magnetic field lines (Aspin et al. 2010; Wang et al. 2023a). The near-IR spectra of FU-Ori type outbursts, in contrast, show no hydrogen lines and CO overtones in deep absorption, suggesting the stars accrete directly through disks that extend to the stellar photospheres (Connelley & Reipurth 2018; Hartmann et al. 2016). More recent work, however, has found that many long-duration bursts (> 5 yr) do show hydrogen line emission suggestive of magnetospheric accretion (Guo et al. 2021).

Since 2004, 3-8 μm studies using multi-epoch data from Spitzer and WISE/NEOWISE identified outbursts from YSOs in nearby molecular clouds with durations of a decade or more, some from protostars that are not detected at shorter wavelengths (Caratti o Garatti et al. 2011; Fischer et al. 2012; Safron et al. 2015; Fischer et al. 2019; Zakri et al. 2022). The duration of these outbursts is similar to FU Ori outbursts (Contreras Peña et al. 2025a). Confirmation of the outburst type through spectra at visible or near-IR wavelengths (i.e. $< 2.5 \mu\text{m}$) is rare. This is due in part

to the lack of a coordinated effort to obtain IR spectra of YSOs in nearby clouds, but for the most deeply embedded protostars, it is also due to our inability to obtain spectra in the $< 2.5 \mu\text{m}$ range.

Two protostellar outbursts for which there are mid-IR light curves and spectra are V2775 Ori and V1647 Ori. The outbursting protostar V2775 Ori (HOPS 223) started its burst between 2005 and 2007 and has sustained the burst through the NEOWISE data (Fig. 14, Caratti o Garatti et al. 2011; Fischer et al. 2012). It appears to be in a face-on orientation where we can observe the protostar through the outflow cavity (Furlan et al. 2016; Federman et al. 2023). The lack of hydrogen lines and the presence of deep CO and H₂O absorption features in the 1-2.5 μm spectrum of this protostar confirm that it is undergoing an FU Ori type outburst that has lasted 18 years (Fischer et al. 2012). The protostar V1647 Ori (J05461313-0006045) underwent a burst with a similar mid-IR amplitude to V2775 Ori that lasted 16 years (Fig. 5, Muzerolle et al. 2005; Kulkarni et al. 2024). In contrast to V2775 Ori, V1647 Ori showed Br- γ emission in its near-IR spectrum indicating magnetospheric (i.e. EX Lupi type) accretion (Aspin & Reipurth 2009). These two cases demonstrate that protostars showing similar 3-8 μm light curves in the sparsely sampled data available, can show distinct near-IR spectra. The similarities in the light curves of these two protostars may be in part due to the incomplete sampling. V1647 Ori may have had multiple episodes of high luminosity over the last 60 years, similar to YSOs classified as fluctuators (Ninan et al. 2013). Given this uncertain landscape and our incomplete light curves, we avoid the classification of our YSOs into the standard categories of FU Ori and EX Lupi bursts based on their light curves.

4.2. Bursts and Fades as Accretion-Driven Outbursts

We interpret the completed bursts, ongoing bursts, and fades as long-duration ($> 5 \text{ yr}$), accretion-driven outbursts sampled at different points in their light curves. In this interpretation, the ongoing bursts are outbursts that were not completed by the final epoch of NEOWISE, and the fades are bursts that started before the ISOCAM observations in 1997. This is supported by the similar Δt vs Δm diagrams of these sources, with the highest amplitudes found at the longest timescales (Fig. 9). We note that our classification of the light curves is provisional and dependent on incomplete sampling. Furthermore, accretion likely continues, although at a lower level, before and after the bursts (e.g. Zakri et al. 2022). Due to variations in this "quiescent" accretion rate, the pre- and post-burst levels may be different and variable.

The observed color variations support that the bursts and fades are parts of accretion-drive outbursts. Zakri et al. (2022) found that during the $\Delta I2 \geq 2 \text{ mag}$ mid-IR outbursts of Class 0 protostars, the I1-I2 colors increased by 0.2 – 0.3 mag as the outbursts peaked. They argued that the color changes were inconsistent with variations in the observed flux due to extinction, and that the outbursts must be due to changes in luminosity driven by variations in accretion. Other outbursts ascribed to accretion bursts show a range of W1-W2 color changes: small shifts to the red (Park et al. 2021; Siwak et al. 2023), little change in the colors (Hillenbrand et al. 2018; Wang et al. 2023b), and finally shifts to the blue that are too small to be due to extinction (Hillenbrand et al. 2019).

In Sec. 3.6, we find that the observed changes in the $\Delta(I2 - I1)/\Delta I2$ and $\Delta(W2 - W1)/\Delta W2$ slopes during our bursts and fades are inconsistent with changes due to variations in the extinction. The bursts and fades show slopes clustered around zero for $\Delta I2$ or $\Delta W2 \geq 0.75 \text{ mag}$ (Fig. 11). The observed changes are consistent with models of protostars and pre-ms stars with disks which show increases in luminosity are accompanied by small or positive (i.e. increasingly red) changes in the 3.6-4.5 colors (Megeath et al. 2012; Hillenbrand & Rodriguez 2022; Fischer et al. 2024). We conclude that the observed color changes are consistent with those observed toward other outbursts and models of outbursts.

Interpreting bursts and fades as parts of outbursts, our light curves include the beginnings and/or ends of outbursts toward 13 YSOs: four completed bursts, three ongoing bursts, and six fades. Since the completed bursts contain both the initial rise and the ending decay, we observe in total 7 ± 2.6 rises and 10 ± 3.3 decays (uncertainties are \sqrt{N}). These numbers are equal within the uncertainties. Our numbers are consistent with a simple interpretation that we are observing outbursts where the rise and decay times are less than the 27 year span of our light curves.

Due to the regular sampling of the NEOWISE photometry, our decays are better sampled than our rises. Out of ten decays found in the completed bursts and fades, four completed bursts and one fade showed rapid declines that lasted $\leq 2 \text{ years}$, while the others show declines extending over more than a decade. In comparison, the rises are typically sampled over three, widely spaced, epochs: ISO in 1997, Spitzer in 2004, and WISE in 2010. Nevertheless, we find a 13-year rise between the ISOCAM and WISE data for J06473562-0622413. In addition, the rise to the maximum flux of J16271383-2443318 is partially sampled by NEOWISE, and lasts six years. Overall, the rises are typically shorter,

with 1/7 rises being longer than a decade and 5/10 decays being longer than a decade. Contreras Peña et al. (2025b) also find longer durations for decays compared to rises.

For the completed bursts, we can constrain the duration of the outbursts from the light curves. The duration of the J05461313-0006405 (V1647 Ori) outburst was 16 years, where the onset was measured in visible light data and the decline was detected by NEOWISE. The J05462569+0023416 burst was a span of 10-17 years, where the uncertainty comes from the poor constraints on the date of the rise. The duration of the J16271758-2405139 burst was 6-16 years where the uncertainty comes from both the times of the rise and that of the decline. In total, the completed bursts have durations between 6-17 years. For the ongoing bursts, we can only estimate lower limits to their durations. The duration of the J16264216-2431031 outburst is ≥ 10 years where we take the initial time as the first detection of the YSO in outburst by WISE. J05362461-0622413 reached a maximum in 2010, after a slow rise that lasted ≥ 13 years; thus this outburst also has a duration of ≥ 14 years. J16271383-2443318 rose within 1 year to an initial maximum in 2013, implying a duration of ≥ 11 years. Finally, J18300772 rose between 1997 and 2004, giving it a duration of ≥ 20 years. Thus, the ongoing bursts require durations greater than 13-20 years.

Constraints on the durations can also be estimated for the fades using the time between their initial measurement and the point when they appear to have returned to their pre-burst luminosity. For J19025867-3707361, the fade has finished by 2004, consistent with a duration ≥ 7 years. J05464312+0000525 and J32938708+311309 both return to their assumed pre-burst levels by 2013, implying durations of ≥ 16 years. For J03290473+3111349 and J16265196-2430396 the fades end by 2014, requiring a duration of ≥ 17 years. Finally, the fade of J05465358+0000061 ends in 2015, requiring a duration of ≥ 18 years. Thus, fades are consistent with outbursts with durations of ≥ 7 years to ≥ 18 years. In summary, when interpreting the light curves of completed bursts, ongoing bursts, and fades as observations of outbursts observed at different phases of their evolution, the observed outbursts have durations as low as 6 years, and in other cases, longer than 20 years. Most are consistent with durations between 10-20 years, with durations that vary from burst to burst.

4.3. Fluctuating Protostars

In addition to the 13 YSOs showing bursts and fades, we find 26 YSOs (13 protostars and 13 pre-ms stars with disks) showing large-amplitude fluctuations. Unlike outbursts, where there is a sustained interval of high luminosity that exceeds 5 years, fluctuators show variations over a range of timescales, from dips in luminosity that last many years, to consecutive large peaks each lasting a few years, to rapid variations on timescales of a month (see Sec. 3.4). The variety of behaviors included in this category suggest that this variability is driven by distinct processes operating on different timescales, or at least similar processes occurring at different radii in the disks of these YSOs. This is demonstrated by the $\Delta m_{4.5 \mu m}$ vs Δt plot for fluctuators in Fig. 9. Although the largest variations are apparent on $\Delta t > 1000$ days, the 90th percentile limit is comparatively constant across all timescales for fluctuators, with significantly higher values at $\Delta t < 100$ days than the bursts or fades.

The observed slopes in the changes of the photometry, i.e. $\Delta(I1 - I2)/\Delta I2$ and $\Delta(W1 - W2)/\Delta W2$ in Fig. 11, are broader than those of the bursts and fades. Although the points with $\Delta I2$ or $\Delta W2$ values ≥ 1 mag cluster around a slope of zero, similar to the bursts and fades, there is a broader distribution of slopes for the fluctuators. In this distribution, a number of points consistent with extinction. We conclude that the variations in the light curves are primarily due to variations in the mass accretion rate, as is the case for the bursts and fades, but that variations in the extinction contribute more to the fluctuators than bursts or fades.

Although we typically conceptualize accretion-driven, large-amplitude variability as episodes of high accretion rates punctuating long periods of a lower level, quiescent accretion, fluctuators show no clear quiescent level. Instead, most show continuous and/or repetitive variations over the 27 years covered in the light curves, and particularly over the 12 year period covered by NEOWISE, for which the light curves are sampled regularly twice a year. In this way, these sources do not fall into the typical categories of large-amplitude variables. They lack the sustained intervals of high luminosity characteristics of FU Ori and V1647 Ori bursts as well as the mid-IR burst and fades in our sample and others (Zakri et al. 2022). The level of variation in these bands is much larger than that observed in the W1 and W2 bands for outbursts of Ex-Lupi during the NEOWISE mission (Wang et al. 2023a).

We also find that there is significant variability during the bursts (Figs. 5 and 6). We require this variability to be less than half of the burst amplitude, or they are classified as fluctuators. The incomplete sampling of the light curves during the bursts, however, may omit variations that could result in the reclassification of YSOs as fluctuators. For example, we classify V1647 Ori (J05461313-0006045) as a burst; however, at visible wavelengths it underwent a large

decline in 2006 before returning to the previous level in 2008; [Aspin et al. \(2009\)](#) suggest that half of the decline was due to a decrease in the source luminosity and the other half was due to an increase in extinction from the formation of dust. This decline occurred during a gap in the Spitzer coverage. If our light curve did show a 3-8 μm decline to pre-burst levels, the first rise in 2003 and decline in 2006 would be similar to the shorter duration variations of fluctuators, while its sustained high luminosity between 2009 and 2017 would be classified as a burst.

Some of the fluctuators may also be undergoing bursts where the initial rise or final fade are not within our 27 year time frame. Supporting this picture, the variations in the fluctuators are comparable to the variability observed toward some of the ongoing bursts (Sec. 3.2). Furthermore, the typical minimum to maximum variations of the fluctuators are between 1-0.75 mag, close to the 0.75 mag cutoff for large-amplitude variability, suggesting that there could be many more fluctuators just below this threshold, with variations similar to those measured during bursts. The presence of fluctuations during bursts hints that states of elevated accretion may be unstable. In general, the nature of the fluctuators needs to be a focus of future studies. These must explore the relationship between the sampling of the light curve and classification, and they must explore the connection between bursts and fluctuations.

5. COMPARISON WITH OTHER STUDIES

The NEOWISE and Spitzer light curves in this work were previously examined by other studies. Spitzer studies used the photometry from the warm-mission YSOVAR program and the cryo-mission data obtained in 2004 (Sec. 2.3, [Rebull et al. 2014](#)). In the combined studies of the Ophiuchus and NGC 1333 regions ([Günther et al. 2014](#); [Rebull et al. 2015](#)), two large-amplitude variables in the NGC 1333 region, 032851.01+311818.5 and 032859.54+312146.7, are also found in our program as fluctuators (Table 3).

[Park et al. \(2021\)](#) used the NEOWISE photometry to determine the lightcurves of 5400 YSOs in nearby star forming regions. We note that the classification scheme is different than the one used here. They classify the light curves as linear, periodic, curved, or stochastic. The stochastic variables they subdivide into bursts, drops, or irregulars. In contrast to our definitions, they define bursts and drops as events of brightening or fading that last a few epochs relative to a stable baseline, and they set a threshold in $\Delta W2$ of three times the standard deviation. Of our 39 variable YSOs, 37 are in their catalog, and 31 are classified as variables: one linear, seven curved, three bursts, and the remainder are irregulars. Fifteen of the 37 YSOs show variations of 0.75 mag or more in W2 in the NEOWISE photometry alone. Of these, we classify two as bursts, one as a fade, and 12 as fluctuators. [Park et al. \(2021\)](#) classify these same YSOs as one burst, two curved, and 12 irregulars. Overall, the 12 fluctuators are more likely to be identified as large-amplitude variables with the NEOWISE data alone; these are classified as 1 curved and 11 irregulars. Thus, there is a close correspondence between the fluctuators and irregulars. One of the fluctuators is the protostar V371 Ser, or EC 53, which is tabulated as an eruptive variable by [Park et al. \(2021\)](#).

Recently, [Contreras Peña et al. \(2025a\)](#) published the Outbursting YSO Catalogue, or OYCAT. We find three sources in common with OYCAT. The completed burst and protostar J05461313-0006045, or V1647 Ori, is classified in OYCAT as a PVM (i.e. a peculiar/v1647 Ori/MNor) eruptive class based on its spectrum and as an intermediate light curve (i.e. duration between that of an FU Ori and EX Lupi type source based on the light curve). The ongoing burst and protostar J05473657+0020062 (Appendix A) is classified in OYCAT as no burst detected (based on the light curve), but with an FUOr-like spectrum ([Connelley & Reipurth 2018](#)). In the ISOCAM and Spitzer data, we see the rise of this FU-Ori like outburst extending from 1997 to 2016 (Figs 12 and 13).

Finally, the fluctuator and protostar J05460363-0014492 (HOPS 315) is classified in OYCAT as a PVM eruptive class with an intermediate light curve class. J05460363-0014492 was recently found to have SiO gas lines and crystalline silicate features in absorption in its JWST MIRI MRS spectrum; these are likely seen in absorption against the emission generated around the mid-plane of a rapidly accreting disk ([McClure et al. 2025](#)). It also shows Br- γ line and CO overtones in emission ([Contreras Peña et al. 2023](#)). The light curve of this source shows that it was rising during the MIRI observations, implying an increase in the accretion rate (Fig. 8, [Contreras Peña et al. 2023](#)).

6. SUMMARY

We report a study combining ISOCAM 6.75 μm , Spitzer/IRAC 3.6 and 4.5 μm , and (NEO)WISE 3.5 and 4.5 μm photometry to construct 3-8 μm light curves extending up to 27 years. For each source, we create 3.6 μm light curves from the IRAC 3.6 μm and WISE 3.5 μm bands, and 4.5 μm light curves from the IRAC 4.5 μm , WISE 4.6 μm and ISOCAM 6.7 μm band. The IRAC photometry includes data from the cryo and warm-missions. We use IRAC 5.8 μm and 8 μm photometry from the cryo-mission to cross-calibrate changes in the ISOCAM photometry to the IRAC 4.5 μm data. With the inclusion of the ISOCAM photometry, the 4.5 μm light curves extend from 1997 to 2024.

Out of the 221 YSOs with ISOCAM, Spitzer and (NEO)WISE photometry extending either from 1997 to 2020 or 1997 to 2024, we find 39 YSOs with large-amplitude variability, defined as exhibiting at least a factor of two variation in flux over the light curve (or a magnitude change of 0.75 mag). We classify the light curves of these large-amplitude variables into four categories: i.) completed bursts showing a rise of a factor of two or more in flux, a sustained high 3-8 μm flux for ≥ 5 year, and then a decline to pre-rise levels, ii.) ongoing bursts showing a factor of two or more rise and then sustained high flux to the final epoch, iii.) fades showing a sustained decline of a factor of two or more in flux over the light curve, and iv.) fluctuators showing shorter timescale variations without a sustained, high-flux phase or sustained decline. From an analysis of the light curves, we report the following:

1. We find completed bursts towards four YSOs (one protostar and three pre-ms stars with disks), ongoing bursts towards three YSOs (one protostar and two pre-ms stars with disks), and fades for six YSOs (three protostars and three pre-ms stars with disks). The remaining 26 YSOs with high-amplitude variations are classified as fluctuators, 13 of which are protostars and 13 pre-ms stars with disks.
2. Thirteen of the 39 YSOs appear to sample YSO outbursts either in their entirety (the 4 completed bursts) or incompletely (the 9 ongoing bursts and fades). The amplitudes in the 4.5 μm light curves range from our limit of 0.75 mag up to 3.3 mag, and the durations may be as short as 6 years, or extend to more than 20 years, with all but one having durations > 10 yrs. The rises and declines of the outbursts can be either rapid (1-2 years) or slow (over a decade).
3. The most common type of large-amplitude variable are fluctuators. This category contains a variety of behaviors: rapid variations over day to month scales, repetitive peaks separated by a few years, and dips extending several years. The maximum $\Delta m_{4.5}$ values of the fluctuators cluster between 0.75 and 1 mag, lower than the bursts and fades, but they show much higher amplitude variations than bursts and fades at time intervals of < 100 days.
4. Changes in the $I1 - I2$ color with $I2$ and $W1 - W2$ with $W2$ suggest that bursts and fades are primarily driven by changes in the luminosity of the central YSO due to episodes of rapid mass accretion. For fluctuators, the variations in fluxes also appear to be primarily driven by variations in the accretion rate, although with contributions from variations in extinction.
5. Significant variations in the 3-8 μm fluxes are present during outbursts. This suggests that high accretion rates may often be unstable and that there may be a connection between the fluctuators and outbursts. Given their prevalence in our sample, understanding the mechanism driving the fluctuators and their connection to outbursts is a central question in the study of YSO variability.

REFERENCES

Antoniucci, S., Giannini, T., Li Causi, G., & Lorenzetti, D. 2014, ApJ, 782, 51, doi: [10.1088/0004-637X/782/1/51](https://doi.org/10.1088/0004-637X/782/1/51)

Aspin, C., & Reipurth, B. 2009, AJ, 138, 1137, doi: [10.1088/0004-6256/138/4/1137](https://doi.org/10.1088/0004-6256/138/4/1137)

Aspin, C., Reipurth, B., Herczeg, G. J., & Capak, P. 2010, ApJL, 719, L50, doi: [10.1088/2041-8205/719/1/L50](https://doi.org/10.1088/2041-8205/719/1/L50)

Aspin, C., Reipurth, B., Beck, T. L., et al. 2009, ApJL, 692, L67, doi: [10.1088/0004-637X/692/2/L67](https://doi.org/10.1088/0004-637X/692/2/L67)

Audard, M., Ábrahám, P., Dunham, M. M., et al. 2014, in Protostars and Planets VI, ed. H. Beuther, R. S. Klessen, C. P. Dullemond, & T. Henning, 387–410, doi: [10.2458/azu_uapress_9780816531240-ch017](https://doi.org/10.2458/azu_uapress_9780816531240-ch017)

Blommaert, J., Siebenmorgen, R., Coulais, A., et al., eds. 2003, ESA Special Publication, Vol. 1262, The ISO Handbook Volume II: CAM - The ISO Camera (v 2.0)

Bontemps, S., André, P., Kaas, A. A., et al. 2001, A&A, 372, 173, doi: [10.1051/0004-6361:20010474](https://doi.org/10.1051/0004-6361:20010474)

Briceño, C., Vivas, A. K., Hernández, J., et al. 2004, ApJL, 606, L123, doi: [10.1086/421395](https://doi.org/10.1086/421395)

Caratti o Garatti, A., García Lopez, R., Scholz, A., et al. 2011, A&A, 526, L1, doi: [10.1051/0004-6361/201016146](https://doi.org/10.1051/0004-6361/201016146)

Cesarsky, C. J., Abergel, A., Agnese, P., et al. 1996, A&A, 315, L32

Chapman, N. L., Mundy, L. G., Lai, S.-P., & Evans, II, N. J. 2009, ApJ, 690, 496, doi: [10.1088/0004-637X/690/1/496](https://doi.org/10.1088/0004-637X/690/1/496)

Connelley, M. S., & Reipurth, B. 2018, ApJ, 861, 145, doi: [10.3847/1538-4357/aaba7b](https://doi.org/10.3847/1538-4357/aaba7b)

Contreras Peña, C., Herczeg, G. J., Ashraf, M., et al. 2023, MNRAS, 521, 5669, doi: [10.1093/mnras/stad820](https://doi.org/10.1093/mnras/stad820)

Contreras Peña, C., Lee, J.-E., Herczeg, G., et al. 2025a, *Journal of Korean Astronomical Society*, 58, 209, doi: [10.5303/JKAS.2025.58.2.209](https://doi.org/10.5303/JKAS.2025.58.2.209)

Contreras Peña, C., Lee, J.-E., Lee, H.-G., et al. 2025b, *ApJ*, 987, 23, doi: [10.3847/1538-4357/add25f](https://doi.org/10.3847/1538-4357/add25f)

Cutri, R. M., Mainzer, A., Conrow, T., et al. 2015, Explanatory Supplement to the NEOWISE Data Release Products, Explanatory Supplement to the NEOWISE Data Release Products

Dunham, M. M., Evans, N. J., I., Terebey, S., Dullemond, C. P., & Young, C. H. 2010a, in *Astronomical Society of the Pacific Conference Series*, Vol. 432, *New Horizons in Astronomy: Frank N. Bash Symposium 2009*, ed. L. M. Stanford, J. D. Green, L. Hao, & Y. Mao, 197

Dunham, M. M., Evans, Neal J., I., Terebey, S., Dullemond, C. P., & Young, C. H. 2010b, *ApJ*, 710, 470, doi: [10.1088/0004-637X/710/1/470](https://doi.org/10.1088/0004-637X/710/1/470)

Dunham, M. M., & Vorobyov, E. I. 2012, *ApJ*, 747, 52, doi: [10.1088/0004-637X/747/1/52](https://doi.org/10.1088/0004-637X/747/1/52)

Dunham, M. M., Allen, L. E., Evans, II, N. J., et al. 2015, *ApJS*, 220, 11, doi: [10.1088/0067-0049/220/1/11](https://doi.org/10.1088/0067-0049/220/1/11)

Enoch, M. L., Evans, II, N. J., Sargent, A. I., & Glenn, J. 2009, *ApJ*, 692, 973, doi: [10.1088/0004-637X/692/2/973](https://doi.org/10.1088/0004-637X/692/2/973)

Evans, Neal J., I., Dunham, M. M., Jørgensen, J. K., et al. 2009, *ApJS*, 181, 321, doi: [10.1088/0067-0049/181/2/321](https://doi.org/10.1088/0067-0049/181/2/321)

Fazio, G. G., Hora, J. L., Allen, L. E., et al. 2004, *ApJS*, 154, 10, doi: [10.1086/422843](https://doi.org/10.1086/422843)

Federman, S., Megeath, S. T., Tobin, J. J., et al. 2023, *ApJ*, 944, 49, doi: [10.3847/1538-4357/ac9f4b](https://doi.org/10.3847/1538-4357/ac9f4b)

Findeisen, K., Cody, A. M., & Hillenbrand, L. 2015, *ApJ*, 798, 89, doi: [10.1088/0004-637X/798/2/89](https://doi.org/10.1088/0004-637X/798/2/89)

Fischer, W. J., Hillenbrand, L. A., Herczeg, G. J., et al. 2022, arXiv e-prints, arXiv:2203.11257, doi: [10.48550/arXiv.2203.11257](https://doi.org/10.48550/arXiv.2203.11257)

Fischer, W. J., Hillenbrand, L. A., Herczeg, G. J., et al. 2023, in *Astronomical Society of the Pacific Conference Series*, Vol. 534, *Protostars and Planets VII*, ed. S. Inutsuka, Y. Aikawa, T. Muto, K. Tomida, & M. Tamura, 355, doi: [10.48550/arXiv.2203.11257](https://doi.org/10.48550/arXiv.2203.11257)

Fischer, W. J., Safron, E., & Megeath, S. T. 2019, *ApJ*, 872, 183, doi: [10.3847/1538-4357/ab01dc](https://doi.org/10.3847/1538-4357/ab01dc)

Fischer, W. J., Megeath, S. T., Tobin, J. J., et al. 2012, *ApJ*, 756, 99, doi: [10.1088/0004-637X/756/1/99](https://doi.org/10.1088/0004-637X/756/1/99)

Fischer, W. J., Megeath, S. T., Furlan, E., et al. 2017, *ApJ*, 840, 69, doi: [10.3847/1538-4357/aa6d69](https://doi.org/10.3847/1538-4357/aa6d69)

Fischer, W. J., Battersby, C., Johnstone, D., et al. 2024, *AJ*, 167, 82, doi: [10.3847/1538-3881/ad188b](https://doi.org/10.3847/1538-3881/ad188b)

Flaherty, K. M., DeMarchi, L., Muzerolle, J., et al. 2016, *ApJ*, 833, 104, doi: [10.3847/1538-4357/833/1/104](https://doi.org/10.3847/1538-4357/833/1/104)

Flaherty, K. M., Muzerolle, J., Rieke, G., et al. 2013, *AJ*, 145, 66, doi: [10.1088/0004-6256/145/3/66](https://doi.org/10.1088/0004-6256/145/3/66)

Flaherty, K. M., Pipher, J. L., Megeath, S. T., et al. 2007, *ApJ*, 663, 1069, doi: [10.1086/518411](https://doi.org/10.1086/518411)

Forbrich, J., Reid, M. J., Menten, K. M., et al. 2017, *ApJ*, 844, 109, doi: [10.3847/1538-4357/aa7aa4](https://doi.org/10.3847/1538-4357/aa7aa4)

Furlan, E., Fischer, W. J., Ali, B., et al. 2016, *ApJS*, 224, 5, doi: [10.3847/0067-0049/224/1/5](https://doi.org/10.3847/0067-0049/224/1/5)

Grosso, N., Hamaguchi, K., Principe, D. A., & Kastner, J. H. 2020, *A&A*, 638, L4, doi: [10.1051/0004-6361/202038185](https://doi.org/10.1051/0004-6361/202038185)

Günther, H. M., Cody, A. M., Covey, K. R., et al. 2014, *AJ*, 148, 122, doi: [10.1088/0004-6256/148/6/122](https://doi.org/10.1088/0004-6256/148/6/122)

Guo, Z., Lucas, P. W., Contreras Peña, C., et al. 2021, *MNRAS*, 504, 830, doi: [10.1093/mnras/stab882](https://doi.org/10.1093/mnras/stab882)

Gutermuth, R. A., Megeath, S. T., Myers, P. C., et al. 2009, *ApJS*, 184, 18, doi: [10.1088/0067-0049/184/1/18](https://doi.org/10.1088/0067-0049/184/1/18)

Gutermuth, R. A., Myers, P. C., Megeath, S. T., et al. 2008, *ApJ*, 674, 336, doi: [10.1086/524722](https://doi.org/10.1086/524722)

Hartmann, L., Herczeg, G., & Calvet, N. 2016, *ARA&A*, 54, 135, doi: [10.1146/annurev-astro-081915-023347](https://doi.org/10.1146/annurev-astro-081915-023347)

Hartmann, L., & Kenyon, S. J. 1996, *ARA&A*, 34, 207, doi: [10.1146/annurev.astro.34.1.207](https://doi.org/10.1146/annurev.astro.34.1.207)

Hartmann, L., Tobin, J. J., Sheehan, P., Kounkel, M., & Zhao, C. 2025, *MNRAS*, 541, 4025, doi: [10.1093/mnras/staf1220](https://doi.org/10.1093/mnras/staf1220)

Hillenbrand, L. A., Reipurth, B., Connelley, M., Cutri, R. M., & Isaacson, H. 2019, *AJ*, 158, 240, doi: [10.3847/1538-3881/ab4e16](https://doi.org/10.3847/1538-3881/ab4e16)

Hillenbrand, L. A., & Rodriguez, A. C. 2022, *Research Notes of the American Astronomical Society*, 6, 6, doi: [10.3847/2515-5172/ac4807](https://doi.org/10.3847/2515-5172/ac4807)

Hillenbrand, L. A., Contreras Peña, C., Morrell, S., et al. 2018, *ApJ*, 869, 146, doi: [10.3847/1538-4357/aaf414](https://doi.org/10.3847/1538-4357/aaf414)

Kaas, A. A., Olofsson, G., Bontemps, S., et al. 2004, *A&A*, 421, 623, doi: [10.1051/0004-6361:20035775](https://doi.org/10.1051/0004-6361:20035775)

Koenig, X. P., & Leisawitz, D. T. 2014, *ApJ*, 791, 131, doi: [10.1088/0004-637X/791/2/131](https://doi.org/10.1088/0004-637X/791/2/131)

Kryukova, E., Megeath, S. T., Gutermuth, R. A., et al. 2012, *AJ*, 144, 31, doi: [10.1088/0004-6256/144/2/31](https://doi.org/10.1088/0004-6256/144/2/31)

Kulkarni, C. S., Behling, T., Burns-Watson, N., et al. 2024, *Research Notes of the American Astronomical Society*, 8, 64, doi: [10.3847/2515-5172/ad2f40](https://doi.org/10.3847/2515-5172/ad2f40)

Lee, S., Lee, J.-E., Contreras Peña, C., et al. 2024, *ApJ*, 962, 38, doi: [10.3847/1538-4357/ad14f8](https://doi.org/10.3847/1538-4357/ad14f8)

Mahabal, A. A., Djorgovski, S. G., Drake, A. J., et al. 2011, *Bulletin of the Astronomical Society of India*, 39, 387, doi: [10.48550/arXiv.1111.0313](https://doi.org/10.48550/arXiv.1111.0313)

Mahoney, W. A., Garcia, L. J., Jr., J. H., et al. 2010, in Observatory Operations: Strategies, Processes, and Systems III, ed. D. R. Silva, A. B. Peck, & B. T. Soifer, Vol. 7737, International Society for Optics and Photonics (SPIE), 77371W, doi: [10.1117/12.857814](https://doi.org/10.1117/12.857814)

Mainzer, A., Bauer, J., Cutri, R. M., et al. 2014, *ApJ*, 792, 30, doi: [10.1088/0004-637X/792/1/30](https://doi.org/10.1088/0004-637X/792/1/30)

Mairs, S., Lee, S., Johnstone, D., et al. 2024, *ApJ*, 966, 215, doi: [10.3847/1538-4357/ad35b6](https://doi.org/10.3847/1538-4357/ad35b6)

McClure, M. K., van't Hoff, M., Francis, L., et al. 2025, *Nature*, 643, 649, doi: [10.1038/s41586-025-09163-z](https://doi.org/10.1038/s41586-025-09163-z)

McNeil, J. W., Reipurth, B., & Meech, K. 2004, IAUC, 8284, 1

Megeath, S. T., Gutermuth, R., Muzerolle, J., et al. 2012, *AJ*, 144, 192, doi: [10.1088/0004-6256/144/6/192](https://doi.org/10.1088/0004-6256/144/6/192)

—. 2016, *AJ*, 151, 5, doi: [10.3847/0004-6256/151/1/5](https://doi.org/10.3847/0004-6256/151/1/5)

Meisner, A. M., Caselden, D., Schlafly, E. F., & Kiwy, F. 2023, *AJ*, 165, 36, doi: [10.3847/1538-3881/aca2ab](https://doi.org/10.3847/1538-3881/aca2ab)

Morales-Calderón, M., Stauffer, J. R., Hillenbrand, L. A., et al. 2011, *ApJ*, 733, 50, doi: [10.1088/0004-637X/733/1/50](https://doi.org/10.1088/0004-637X/733/1/50)

Muzerolle, J., Megeath, S. T., Flaherty, K. M., et al. 2005, *ApJL*, 620, L107, doi: [10.1086/428832](https://doi.org/10.1086/428832)

Narang, M., Manoj, P., Tyagi, H., et al. 2024, *ApJL*, 962, L16, doi: [10.3847/2041-8213/ad1de3](https://doi.org/10.3847/2041-8213/ad1de3)

Ninan, J. P., Ojha, D. K., Bhatt, B. C., et al. 2013, *ApJ*, 778, 116, doi: [10.1088/0004-637X/778/2/116](https://doi.org/10.1088/0004-637X/778/2/116)

Offner, S. S. R., & McKee, C. F. 2011, *ApJ*, 736, 53, doi: [10.1088/0004-637X/736/1/53](https://doi.org/10.1088/0004-637X/736/1/53)

Olofsson, G., Huldtgren, M., Kaas, A. A., et al. 1999, *A&A*, 350, 883

Olofsson, G., Kaas, A. A., Bontemps, S., et al. 2000, in ESA Special Publication, Vol. 445, Star Formation from the Small to the Large Scale, ed. F. Favata, A. Kaas, & A. Wilson, 201

Park, W., Lee, J.-E., Contreras Peña, C., et al. 2021, *ApJ*, 920, 132, doi: [10.3847/1538-4357/ac1745](https://doi.org/10.3847/1538-4357/ac1745)

Persi, P., Marenzi, A. R., Olofsson, G., et al. 2000, *A&A*, 357, 219

Pokhrel, R., Gutermuth, R. A., Betti, S. K., et al. 2020, *ApJ*, 896, 60, doi: [10.3847/1538-4357/ab92a2](https://doi.org/10.3847/1538-4357/ab92a2)

Pokhrel, R., Megeath, S. T., Gutermuth, R. A., et al. 2023, *ApJS*, 266, 32, doi: [10.3847/1538-4365/acbfac](https://doi.org/10.3847/1538-4365/acbfac)

Poppenhaeger, K., Cody, A. M., Covey, K. R., et al. 2015, *AJ*, 150, 118, doi: [10.1088/0004-6256/150/4/118](https://doi.org/10.1088/0004-6256/150/4/118)

Reach, W. T., Megeath, S. T., Cohen, M., et al. 2005, *PASP*, 117, 978, doi: [10.1086/432670](https://doi.org/10.1086/432670)

Rebull, L. M., Cody, A. M., Covey, K. R., et al. 2014, *AJ*, 148, 92, doi: [10.1088/0004-6256/148/5/92](https://doi.org/10.1088/0004-6256/148/5/92)

Rebull, L. M., Stauffer, J. R., Cody, A. M., et al. 2015, *AJ*, 150, 175, doi: [10.1088/0004-6256/150/6/175](https://doi.org/10.1088/0004-6256/150/6/175)

Rodrigo, C., Solano, E., & Bayo, A. 2012, SVO Filter Profile Service Version 1.0, IVOA Working Draft 15 October 2012, doi: [10.5479/ADS/bib/2012ivoa.rept.1015R](https://doi.org/10.5479/ADS/bib/2012ivoa.rept.1015R)

Ryan, B. W., Stokes-Geddes, H., & Froebrich, D. 2025, *MNRAS*, 543, 1133, doi: [10.1093/mnras/staf1495](https://doi.org/10.1093/mnras/staf1495)

Safron, E. J., Fischer, W. J., Megeath, S. T., et al. 2015, *ApJL*, 800, L5, doi: [10.1088/2041-8205/800/1/L5](https://doi.org/10.1088/2041-8205/800/1/L5)

Samus, N. N. 2004, IAUC, 8354, 1

Scholz, A., Froebrich, D., & Wood, K. 2013, *MNRAS*, 430, 2910, doi: [10.1093/mnras/stt091](https://doi.org/10.1093/mnras/stt091)

Siwak, M., Hillenbrand, L. A., Kóspál, Á., et al. 2023, *MNRAS*, 524, 5548, doi: [10.1093/mnras/stad2135](https://doi.org/10.1093/mnras/stad2135)

Stauffer, J., Cody, A. M., Baglin, A., et al. 2014, *AJ*, 147, 83, doi: [10.1088/0004-6256/147/4/83](https://doi.org/10.1088/0004-6256/147/4/83)

Stetson, P. B. 1987, *PASP*, 99, 191, doi: [10.1086/131977](https://doi.org/10.1086/131977)

Terebey, S., Cody, A. M., Rebull, L. M., & Stauffer, J. R. 2016, in IAU Symposium, Vol. 314, Young Stars & Planets Near the Sun, ed. J. H. Kastner, B. Stelzer, & S. A. Metchev, 209–210, doi: [10.1017/S1743921315006353](https://doi.org/10.1017/S1743921315006353)

Vorobyov, E. I., & Basu, S. 2006, *The Astrophysical Journal*, 650, 956, doi: [10.1086/507320](https://doi.org/10.1086/507320)

Wang, M.-T., Herczeg, G. J., Liu, H.-G., et al. 2023a, *ApJ*, 957, 113, doi: [10.3847/1538-4357/acf2f4](https://doi.org/10.3847/1538-4357/acf2f4)

Wang, T., Li, J., N. Mace, G., et al. 2023b, *ApJ*, 957, 8, doi: [10.3847/1538-4357/acf92e](https://doi.org/10.3847/1538-4357/acf92e)

Wright, E. L., Eisenhardt, P. R. M., Mainzer, A. K., et al. 2010, *AJ*, 140, 1868, doi: [10.1088/0004-6256/140/6/1868](https://doi.org/10.1088/0004-6256/140/6/1868)

Zakri, W., Megeath, S. T., Fischer, W. J., et al. 2022, *ApJL*, 924, L23, doi: [10.3847/2041-8213/ac46ae](https://doi.org/10.3847/2041-8213/ac46ae)

1 In this paper, we remember the contributions of co-author WJF, who tragically passed away at the height of his
2 abilities during the work on this paper. This paper uses observations from the Spitzer Space Telescope, operated
3 by JPL/Caltech under a contract with NASA, and the Wide-field Infrared Survey Explorer, a joint project of the
4 University of California, Los Angeles, and JPL/Caltech, funded by NASA. It is also based on observations with ISO,
5 an ESA project with instruments funded by ESA Member States (especially the PI countries: France, Germany, the
6 Netherlands and the United Kingdom) and with the participation of ISAS and NASA. It makes use of the NASA/IPAC
7 Infrared Science Archive, operated by JPL/Caltech under a contract with NASA. S.T.M. and R.A.G. were supported
8 by the NASA ADAP grant 80NSSC19K0591, and S.T.M. was supported by the NASA ADAP grant 80NSSC20K0454.
9 R.P. was supported by the NASA ADAP grant 80NSSC18K1564. N.B-W's work was supported by the summer REU
10 program at the University of Toledo. This research has made use of the SVO Filter Profile Service "Carlos Rodrigo",
11 funded by MCIN/AEI/10.13039/501100011033/ through grant PID2023-146210NB-I00

J05473657+0020062

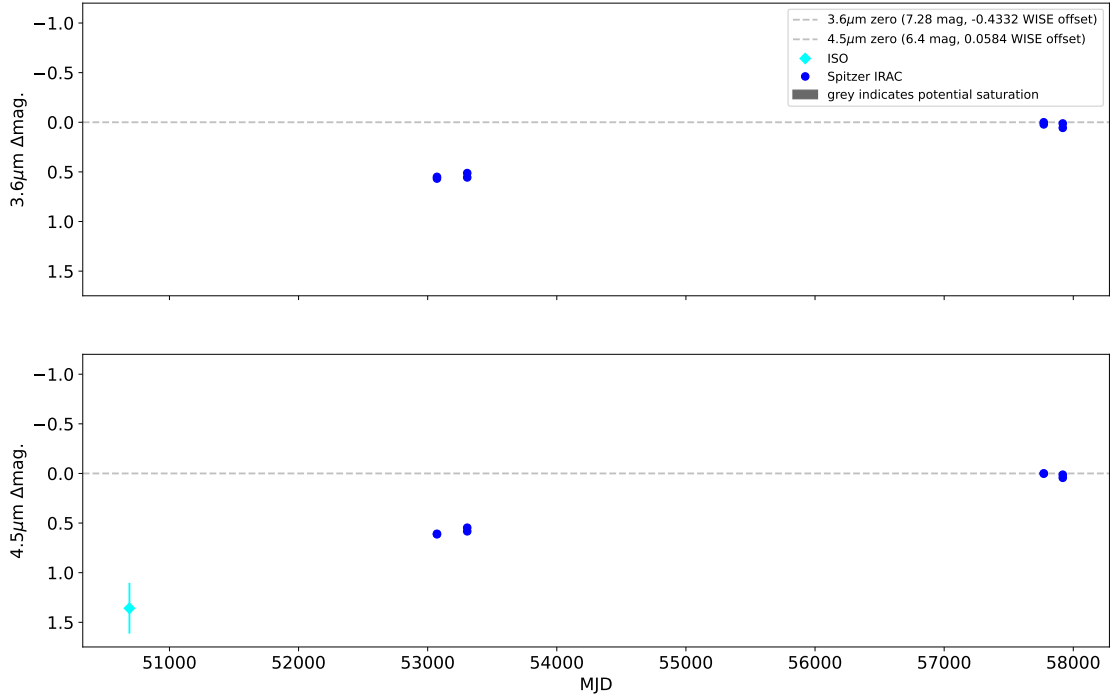


Figure 12. The light curves of the Orion protostar J05473657+0020062, or HOPS 364.

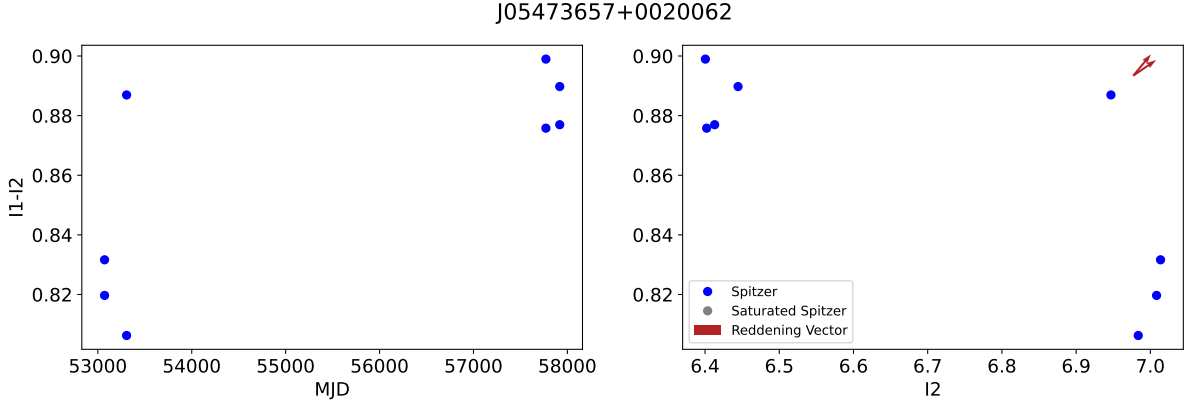


Figure 13. The CMD of the Orion protostar J05473657+0020062, or HOPS 364.

7. APPENDIX A

In Figure 12, we show the light curve of J05473657+0020062 (HOPS 364), which shows a gradual burst in the ISO and Spitzer photometry. Due to extended nebulosity coincident with this protostar, there are no WISE or NEOWISE detections. For this reason, we do not include this source in our analysis. This protostar shows an FU Ori like spectrum in the near-IR (Connelley & Reipurth 2018).

We also show the light curve of v2775 Ori (HOPS 223), which also shows an FU Ori like spectrum (Fischer et al. 2012). This is not included in the main text due to the lack of an ISO observation, and is put here for comparison with the other light curves.

HOPS223

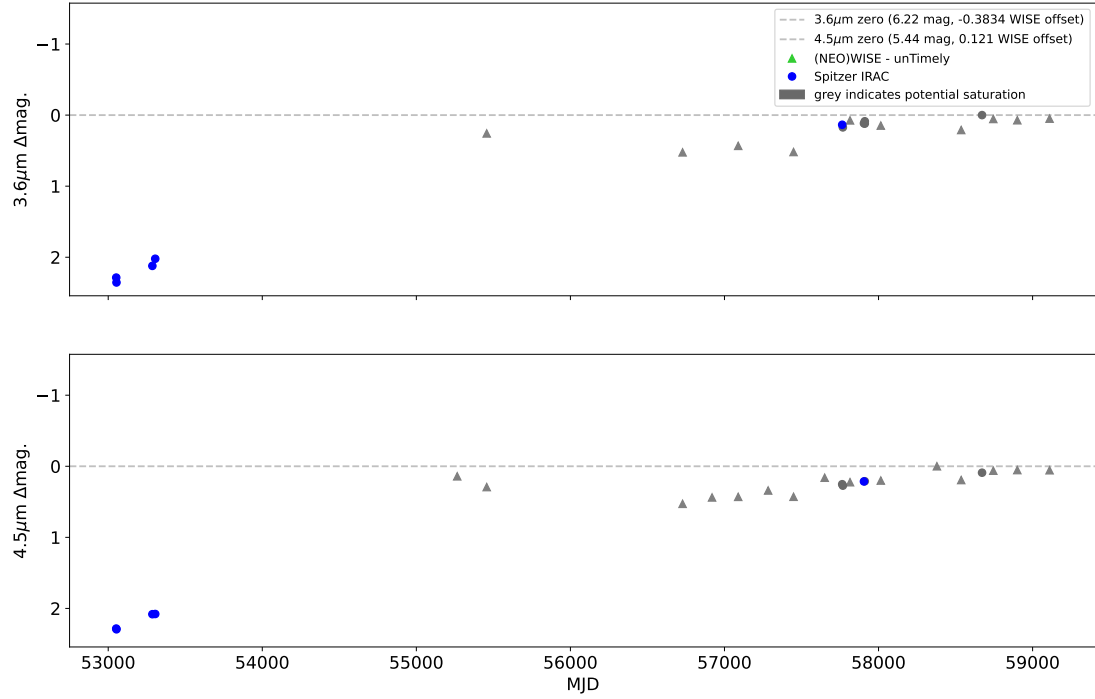


Figure 14. The light curve of the Orion protostar v2775 Ori, or HOPS 223. The light curves shows the ongoing burst from this protostar, which was first discovered by [Caratti o Garatti et al. \(2011\)](#) and studied by [Fischer et al. \(2012\)](#)

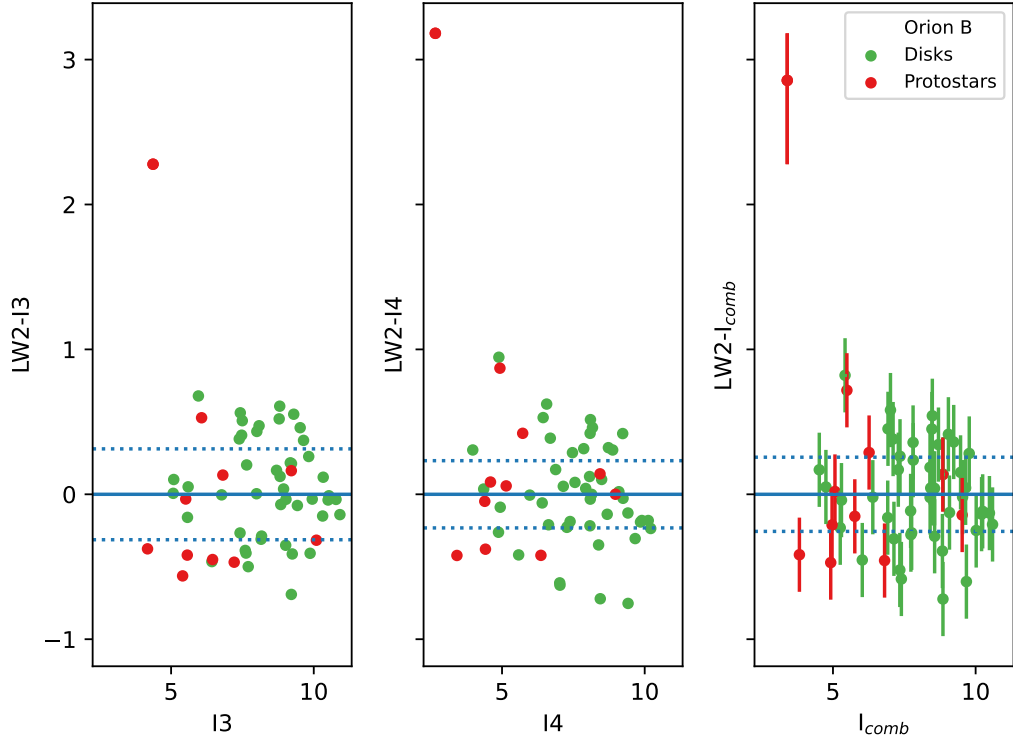
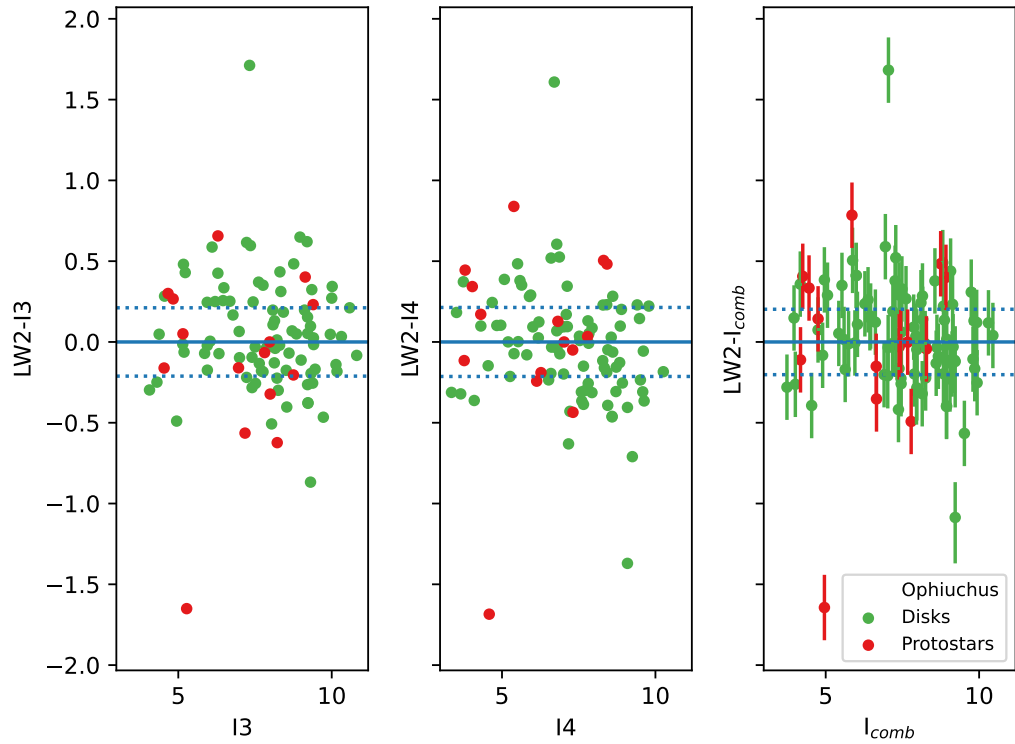
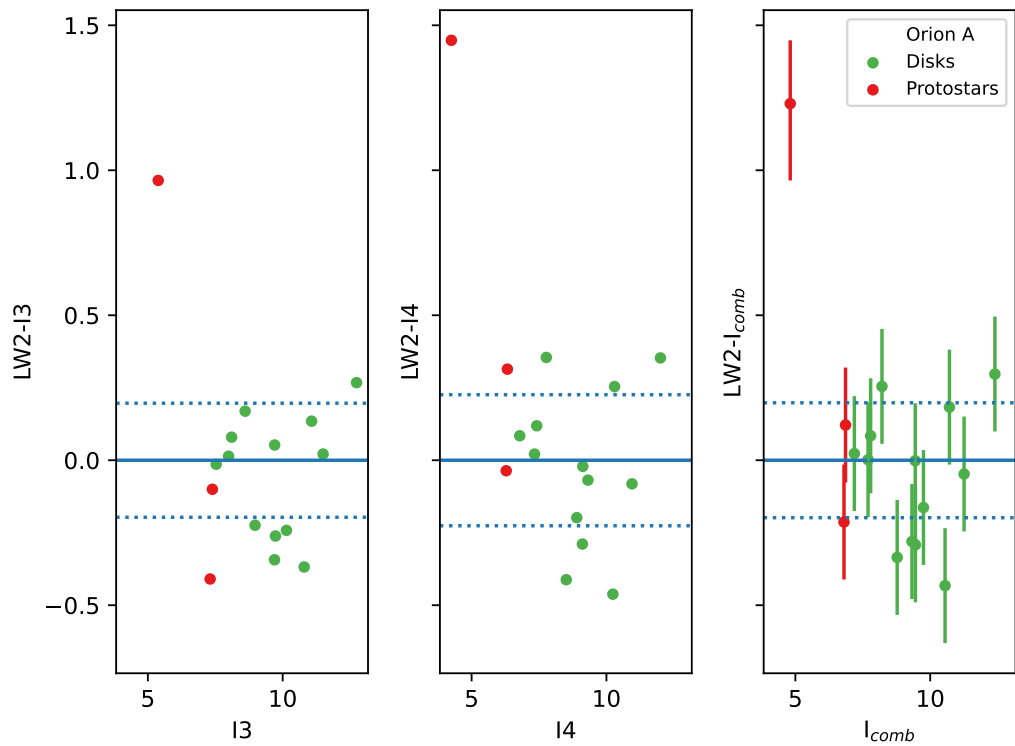


Figure 15. Difference between ISO magnitude (6.7 μ m) and Spitzer magnitude versus Spitzer magnitude for YSOs in the Orion B field. Leftmost uses the 5.8 μ m magnitude for Spitzer, center: 8 μ m, and right: the two combined.



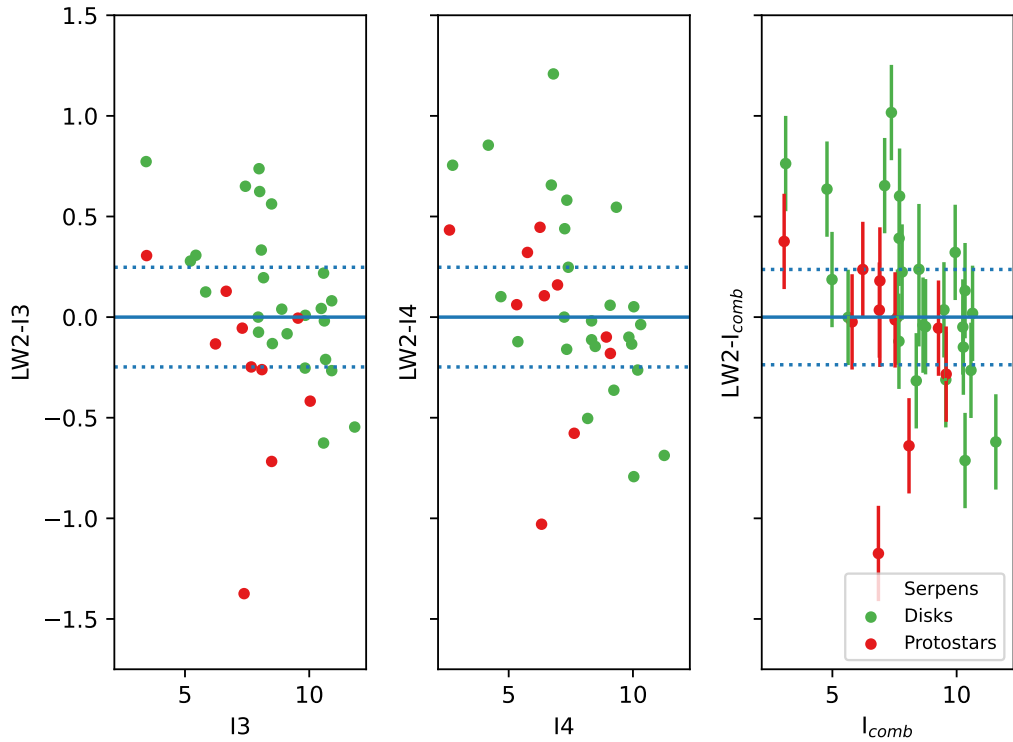


Figure 15. Serpens

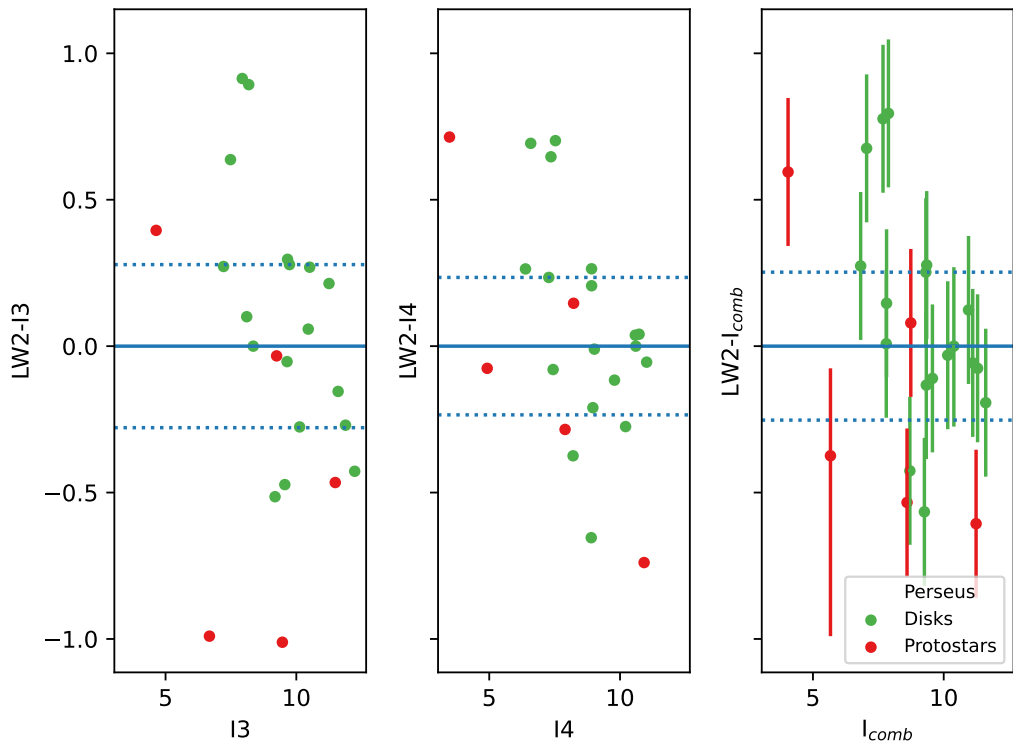
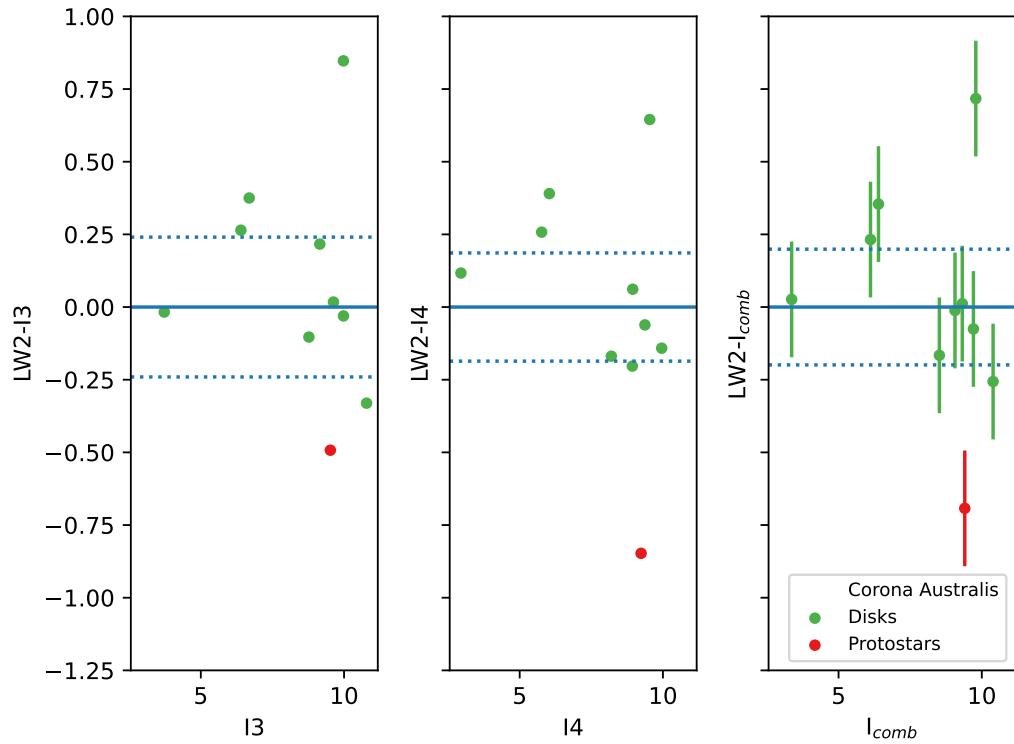
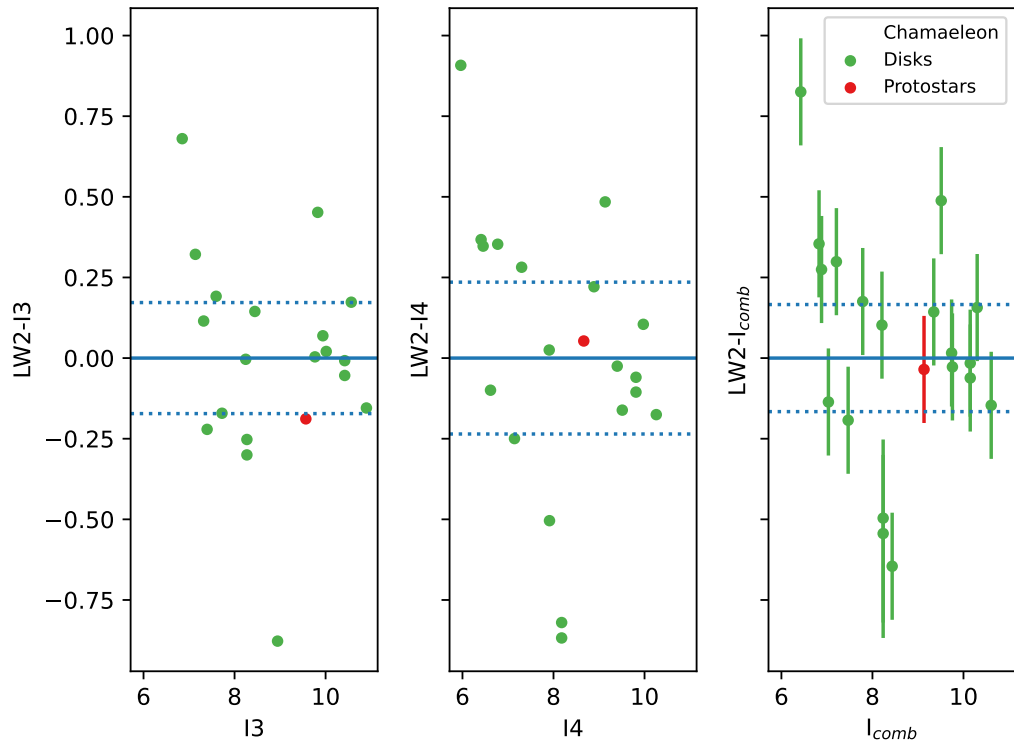


Figure 15. NGC 1333



J05461313-0006045

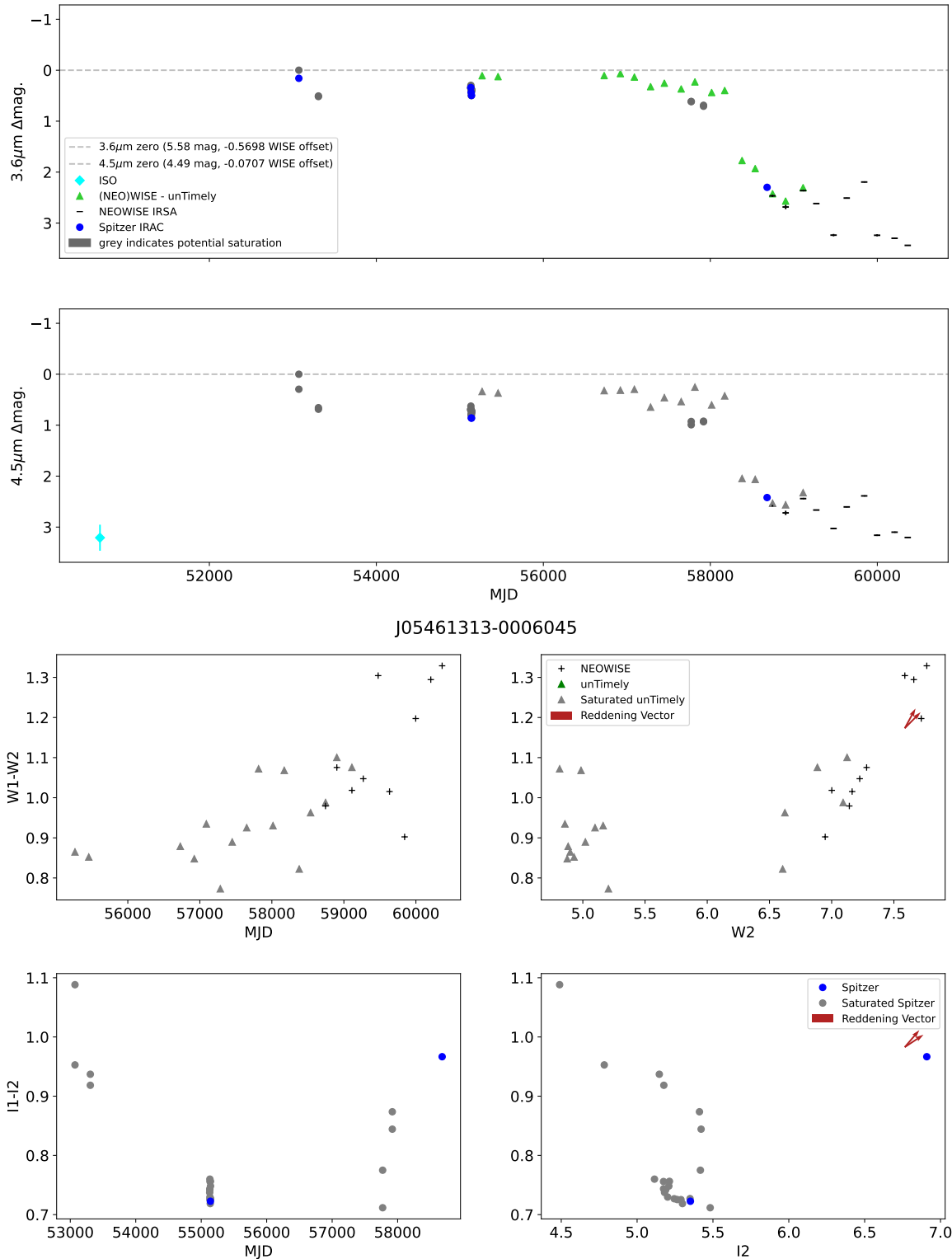


Figure 16. Top two panels: $3.6\mu\text{m}$ and $4.5\mu\text{m}$ light curves of the ongoing bursts. The magnitudes corresponding to a zero Δmag in the light curves and the offsets applied to the WISE photometry are given in the legend. Bottom four panels: clockwise from upper left, the $W1-W2$ vs MJD, $W1-W2$ vs $4.5\mu\text{m}$ magnitude, $I1-I2$ vs $4.5\mu\text{m}$ magnitude, and $I1-I2$ vs MJD diagrams.

J05462569+0023416

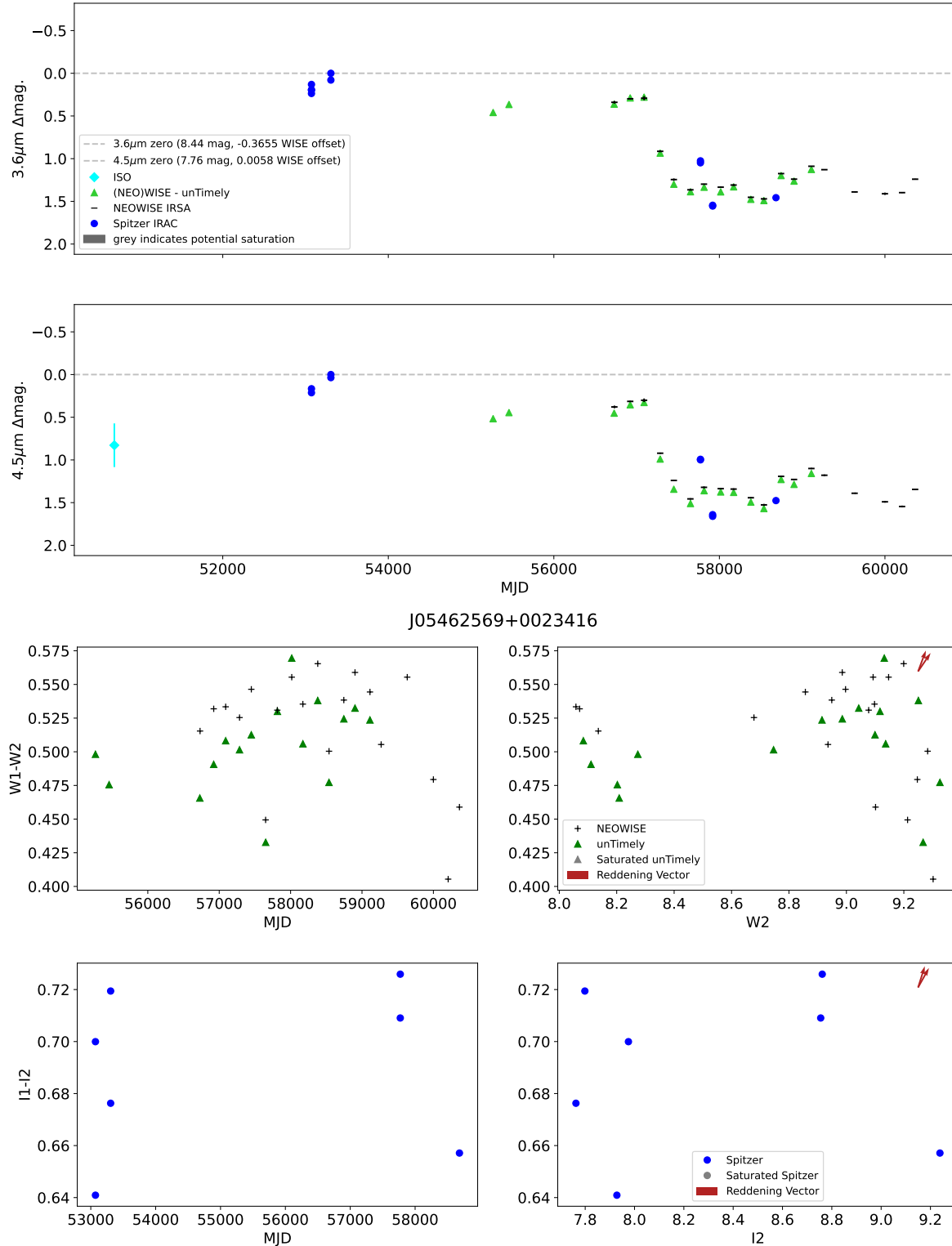


Figure 16. See above.

J16271758-2405139

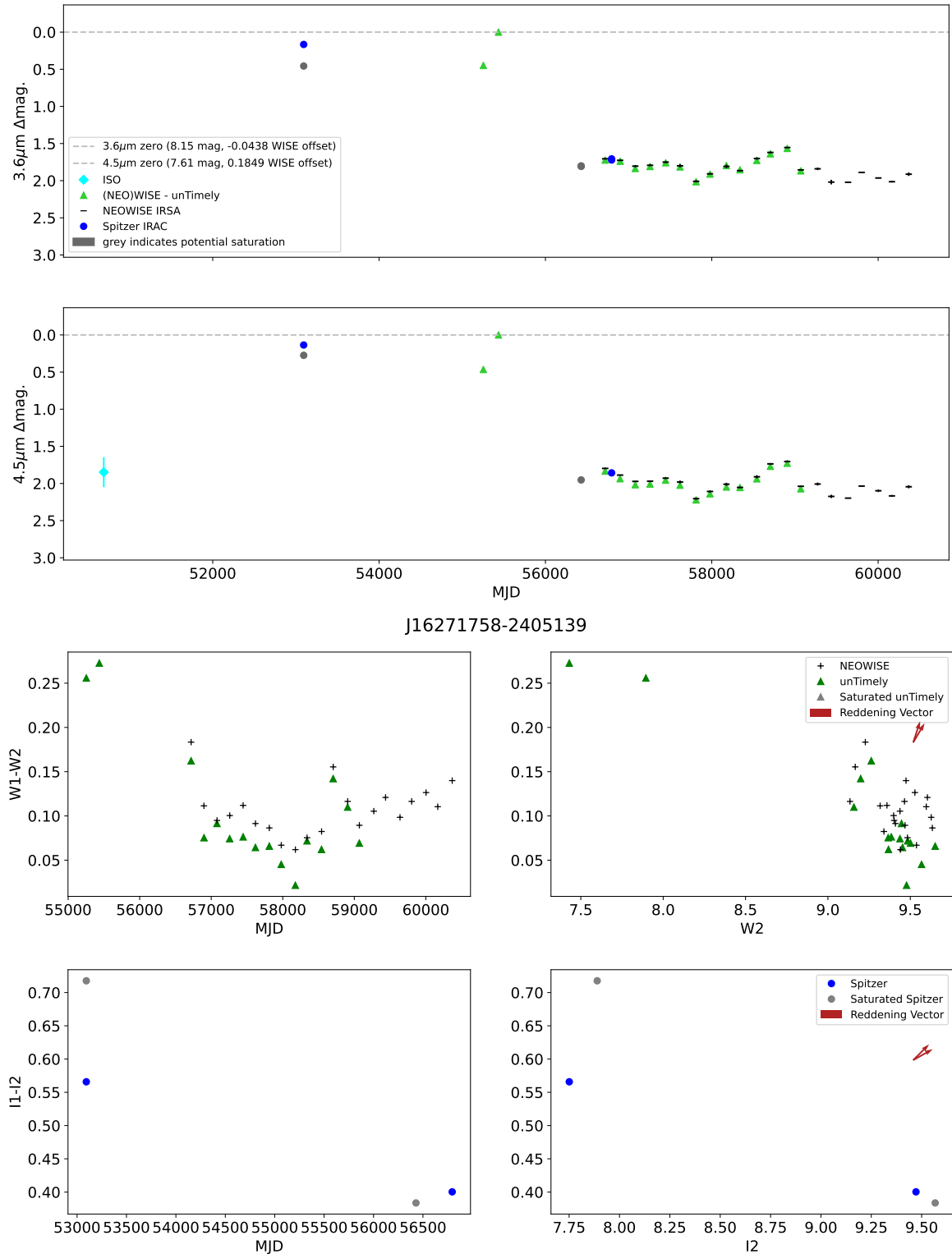


Figure 16. See above.

J16264216-2431031

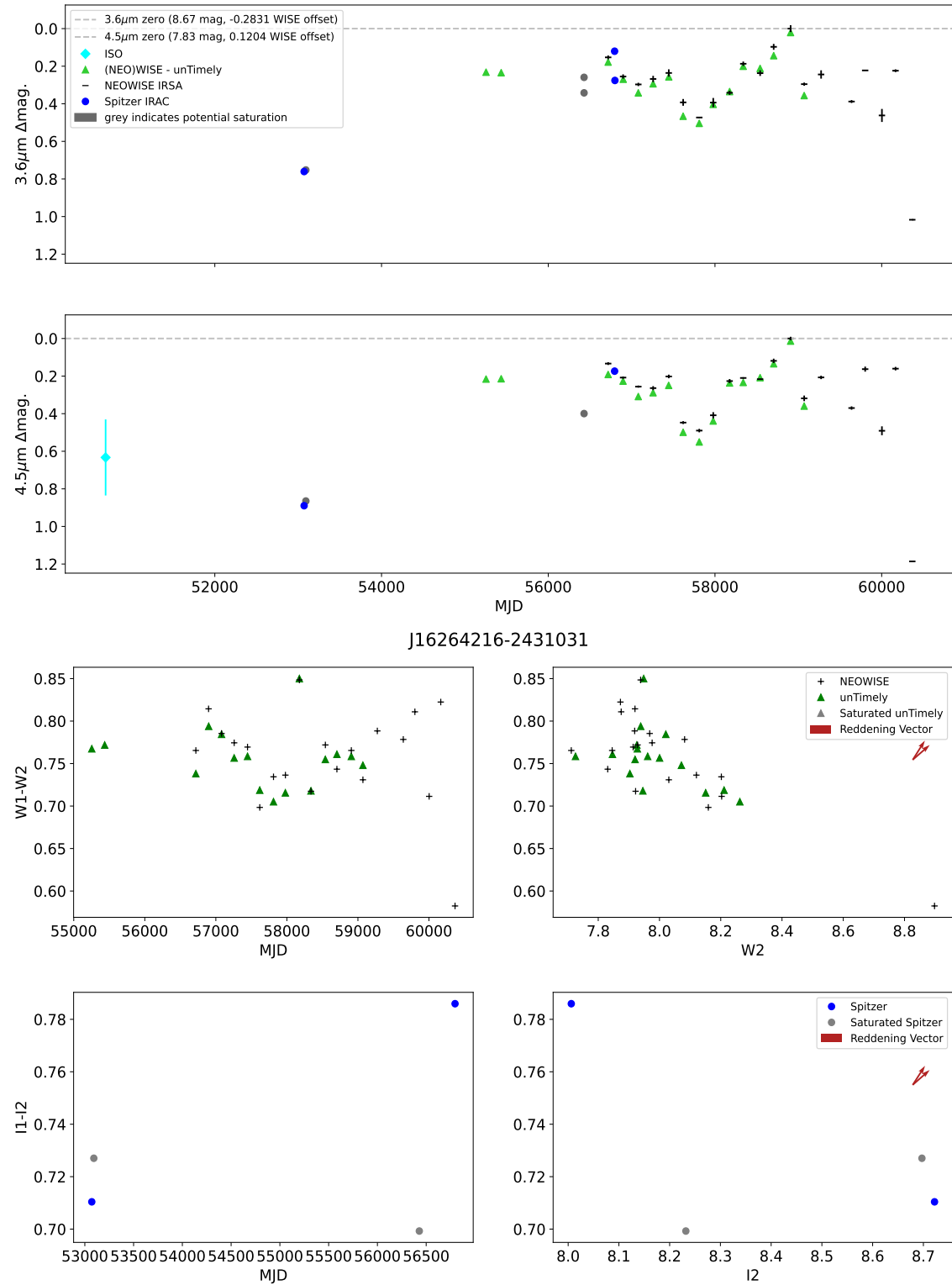


Figure 17. See above

J05362461-0622413

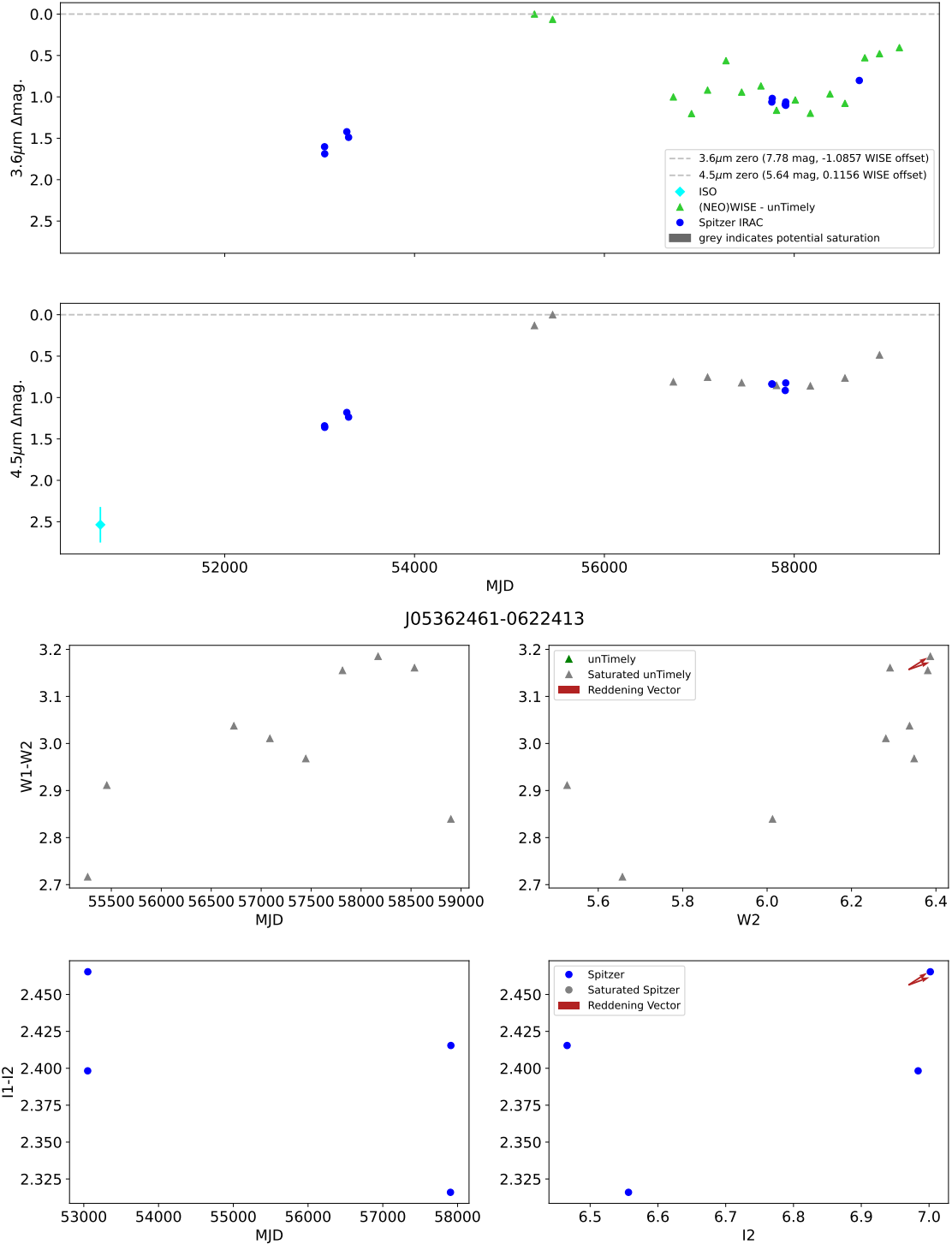


Figure 18. Top two panels: 3.6 and $4.5\mu\text{m}$ light curves of the ongoing bursts. The magnitudes corresponding to a zero Δmag in the light curves and the offsets applied to the WISE photometry are given in the legend. Bottom four panels: clockwise from upper left, the $W1-W2$ vs MJD, $W1-W2$ vs $4.5\mu\text{m}$ magnitude, $I1-I2$ vs $4.5\mu\text{m}$ magnitude, and $I1-I2$ vs MJD diagrams.

J16271383-2443318

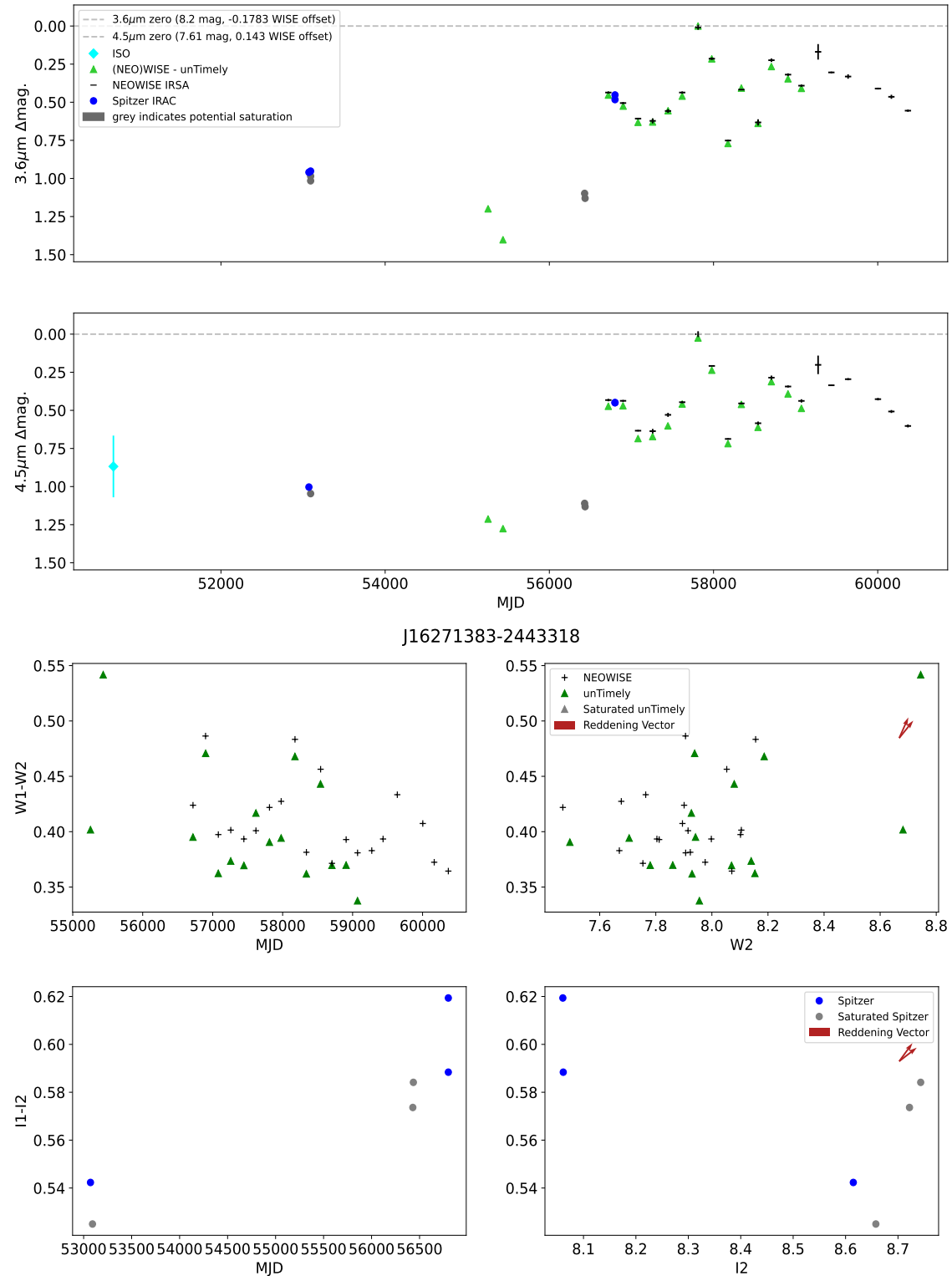


Figure 17. See above

J18300772+0112044

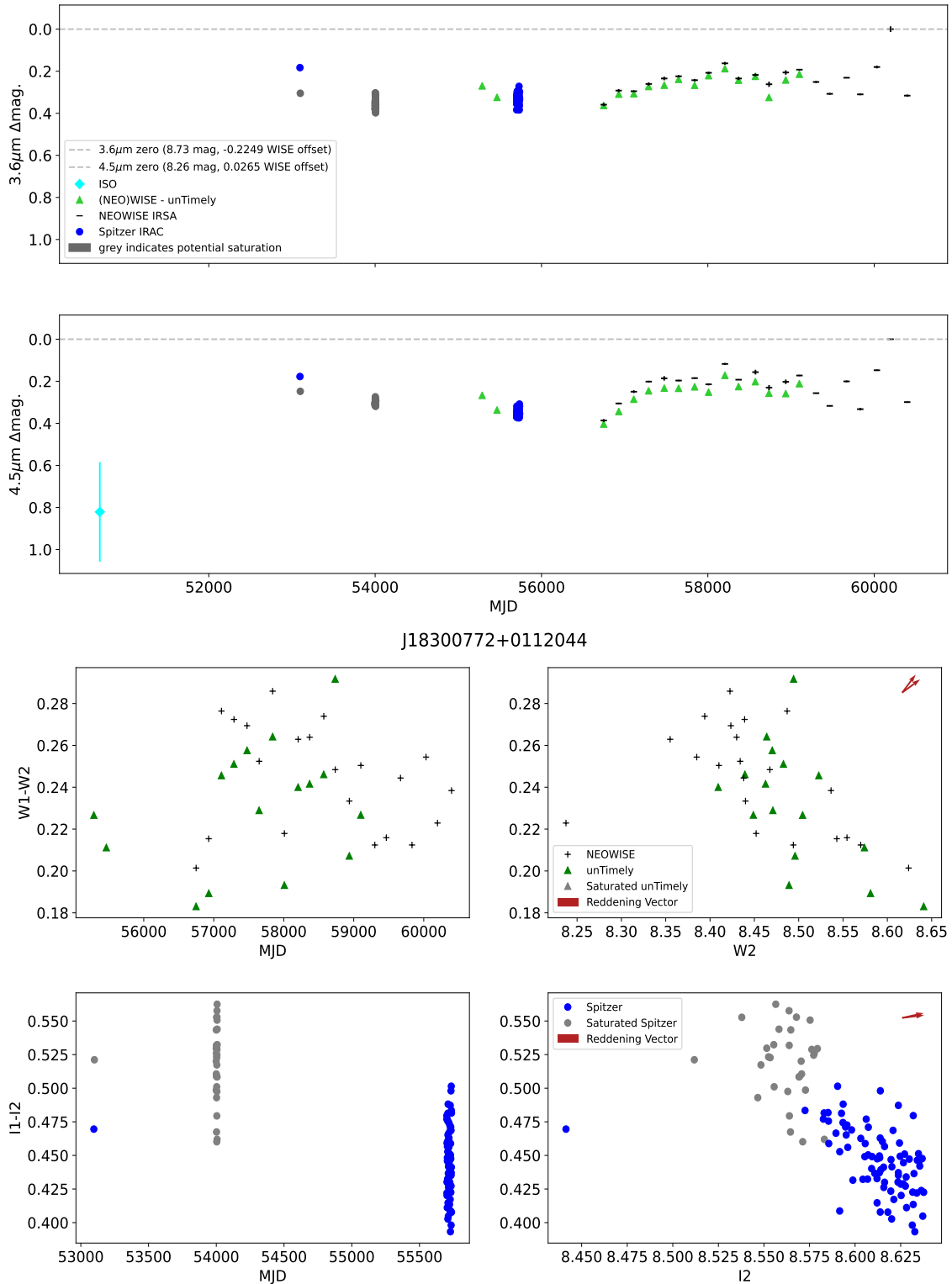


Figure 17. See above

J03283708+3113309

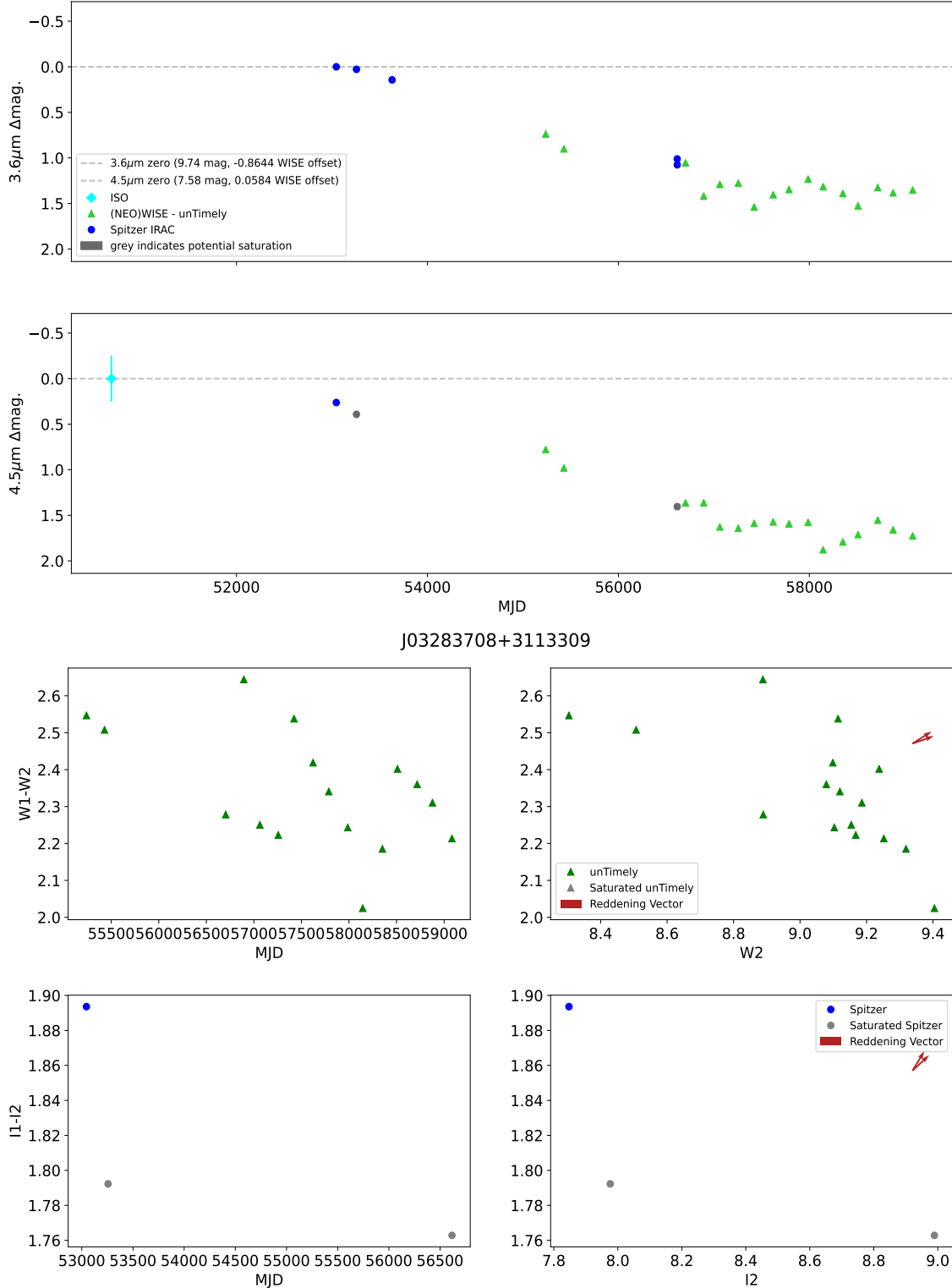


Figure 18. Top two panels: 3.6 and $4.5\mu\text{m}$ light curves of the fading YSOs. The magnitudes corresponding to a zero $\Delta\text{mag.}$ in the light curves and the offsets applied to the WISE photometry are given in the legend. Bottom four panels: clockwise from upper left, the $W1-W2$ vs MJD, $W1-W2$ vs $4.5\mu\text{m}$ magnitude, $I1-I2$ vs $4.5\mu\text{m}$ magnitude, and $I1-I2$ vs MJD diagrams.

J03290473+3111349

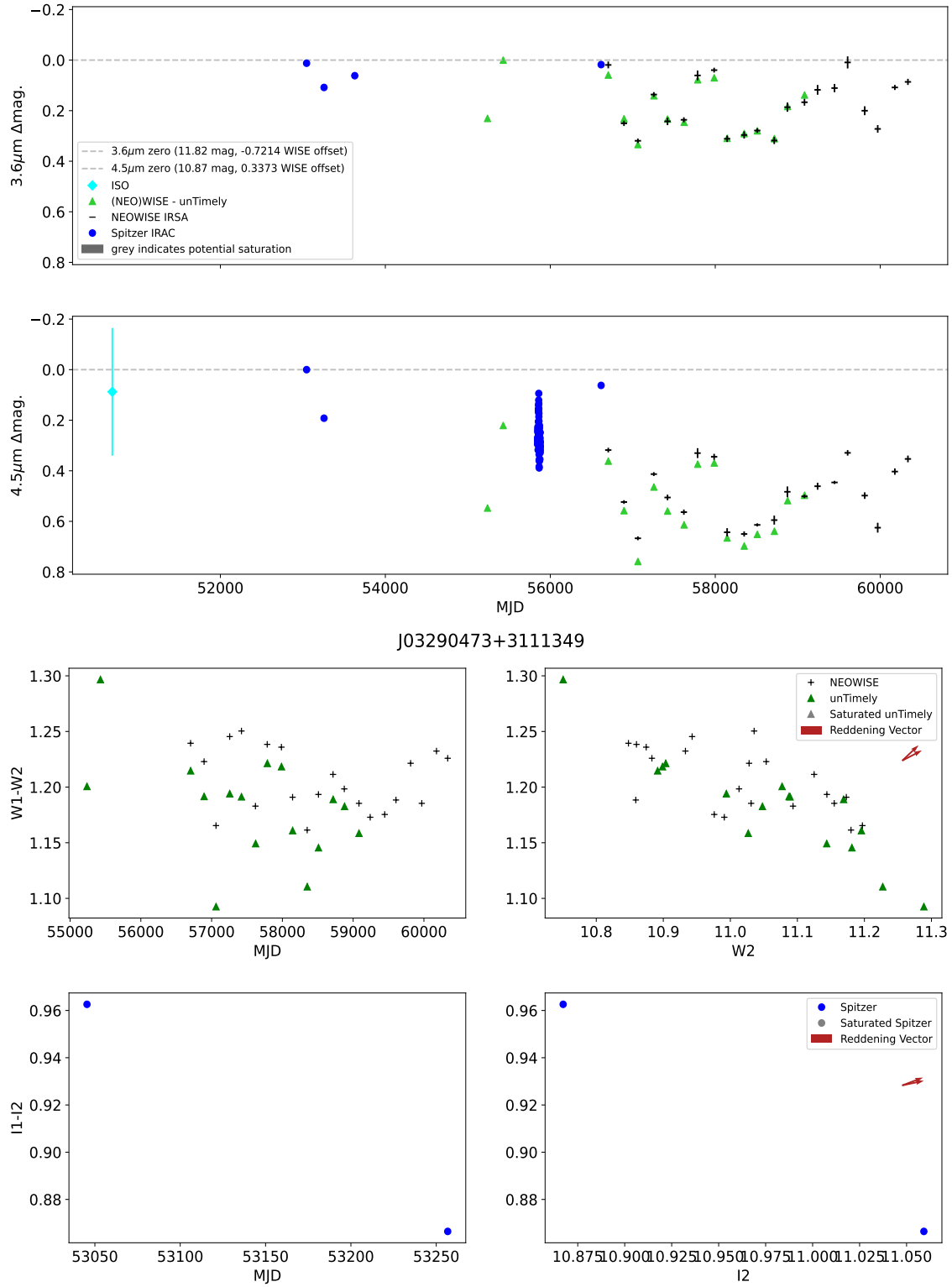


Figure 18. See above.

J05465358+0000061

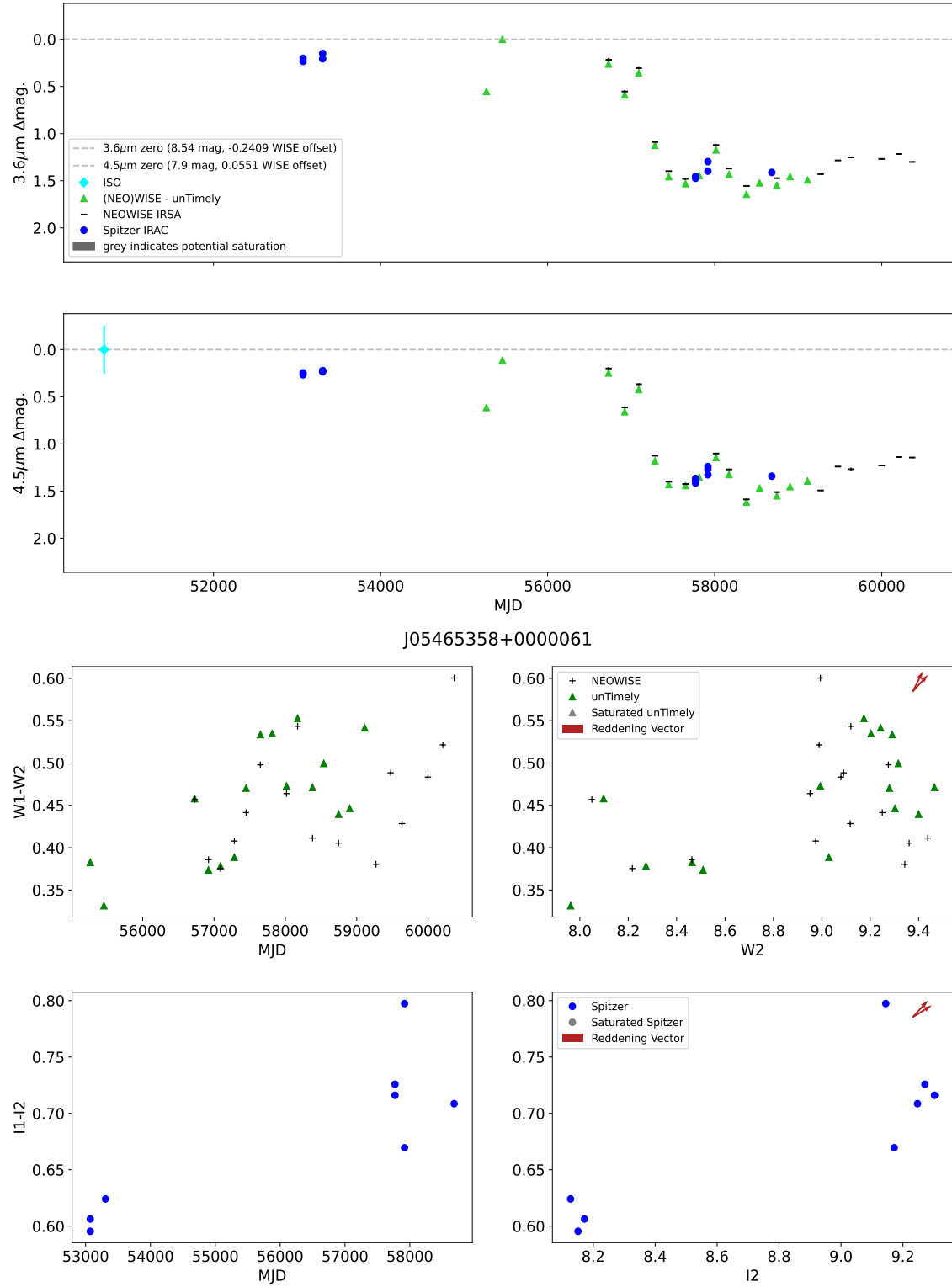


Figure 18. See above.

J05464312+0000525

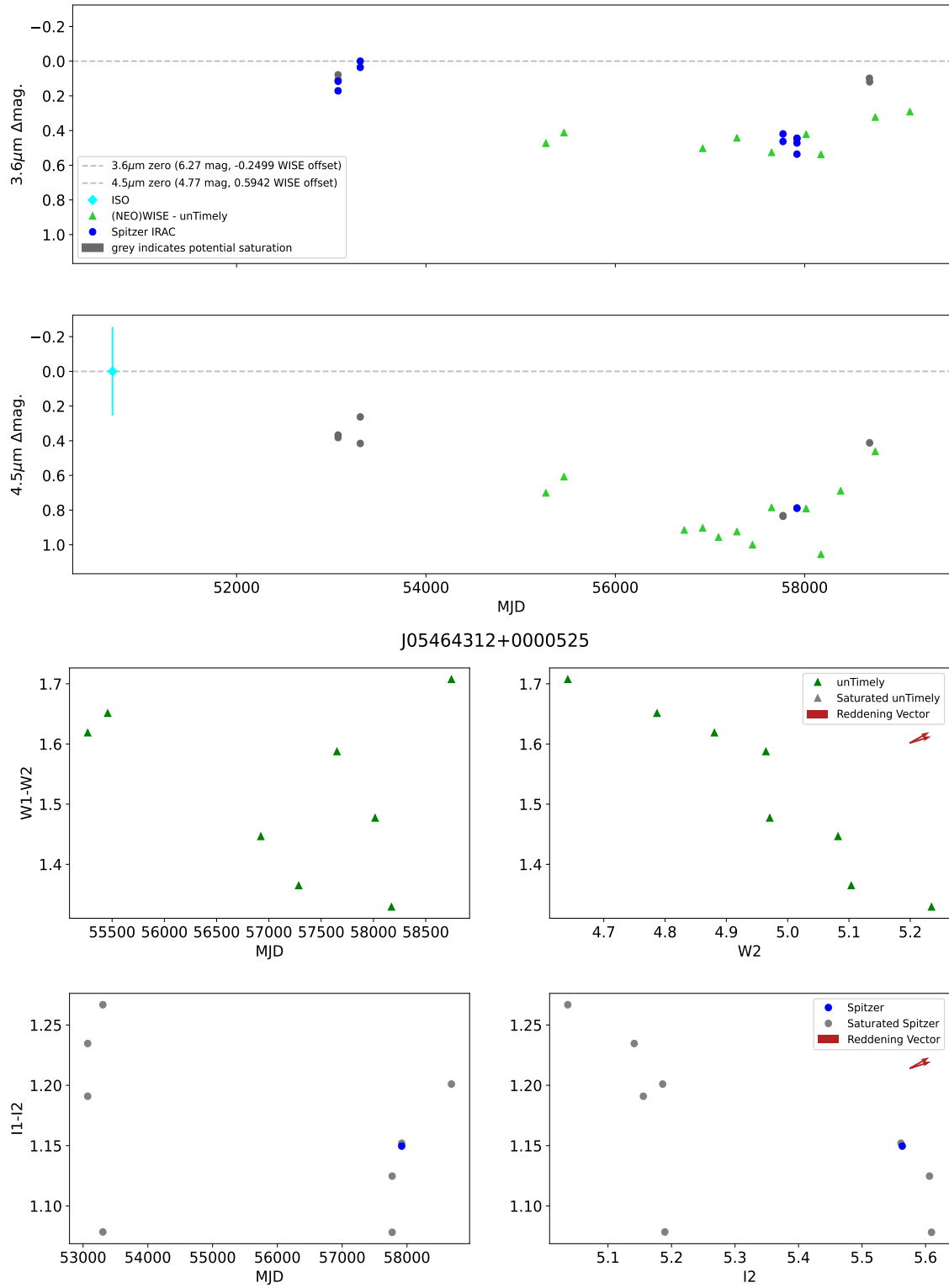


Figure 18. See above.

J16265196-2430396

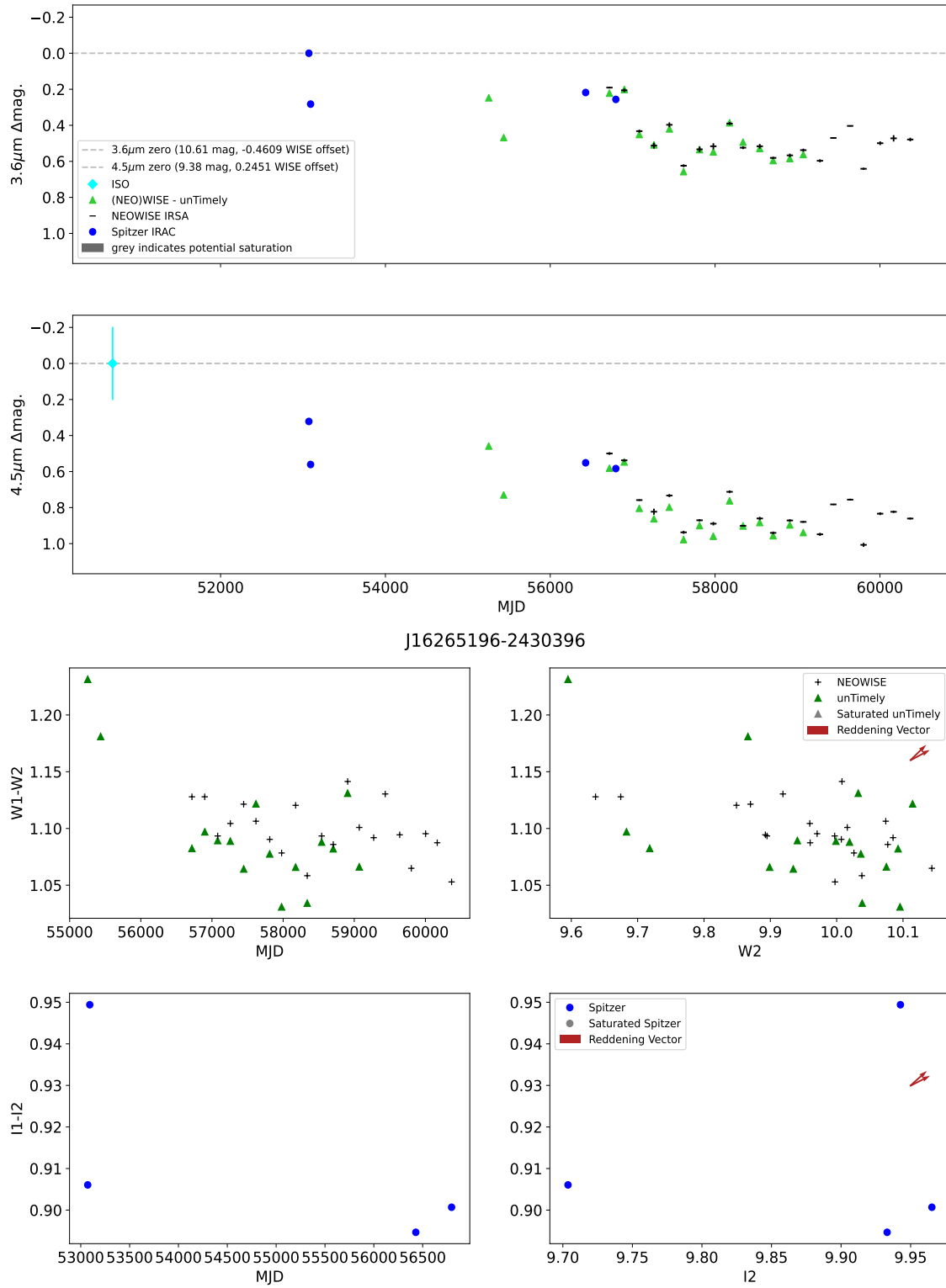


Figure 18. See above.

J19025867-3707361

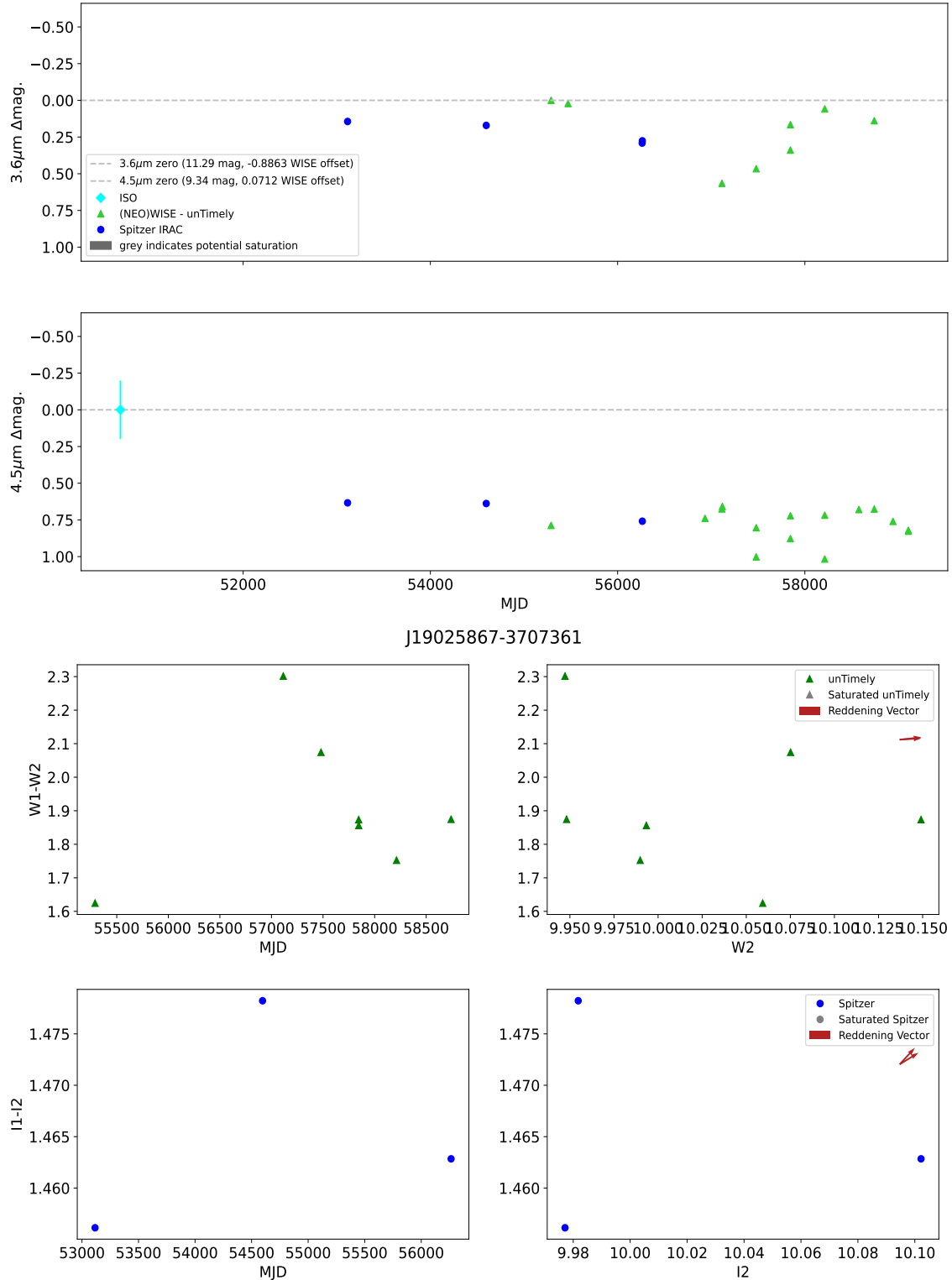


Figure 18. See above.

J03285955+3121467

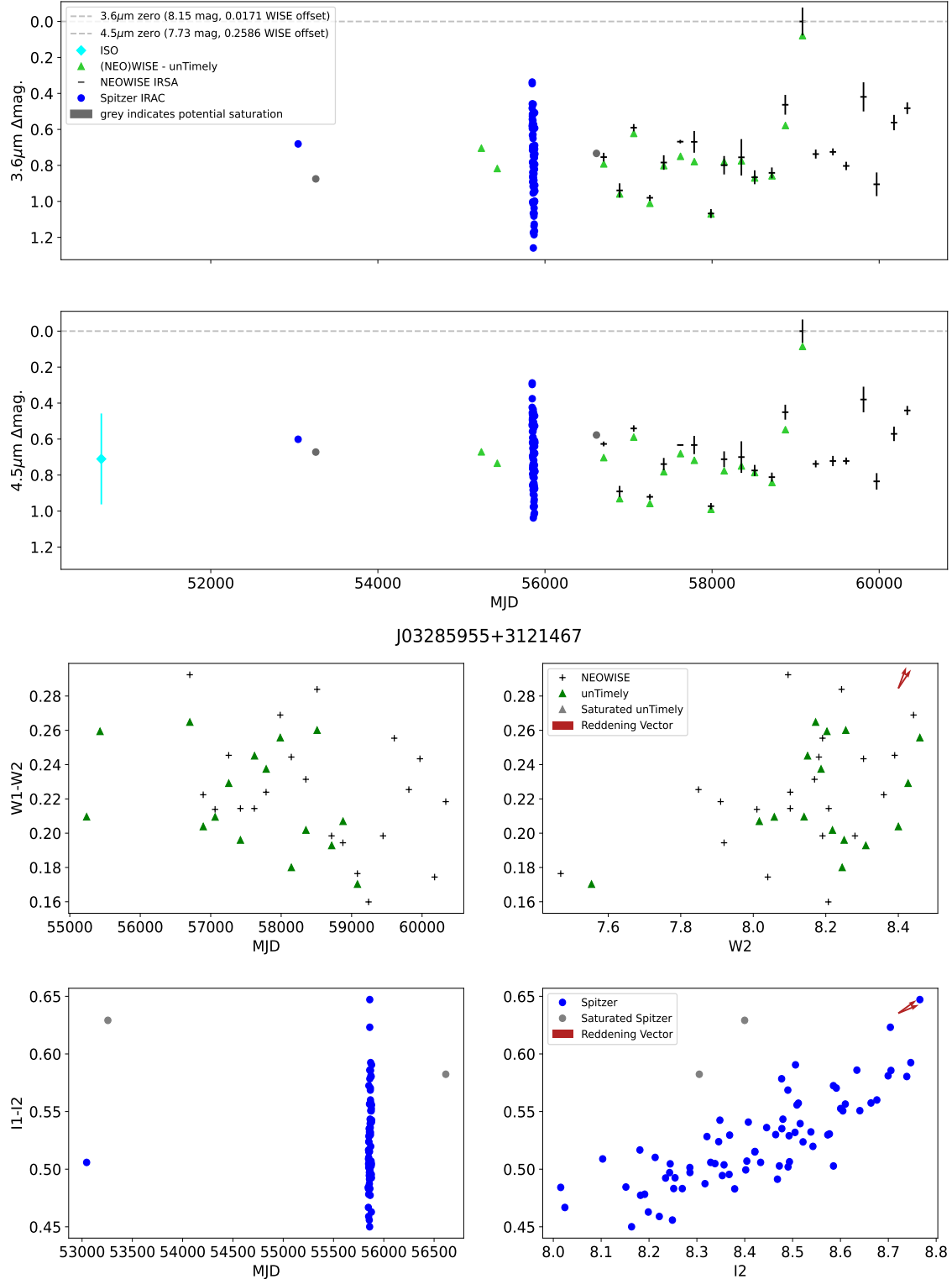


Figure 19. Top two panels: 3.6 and 4.5 μ m light curves of the fluctuating YSOs. The magnitudes corresponding to a zero Δ mag in the light curves and the offsets applied to the WISE photometry are given in the legend. Bottom four panels: clockwise from upper left, the W1-W2 vs MJD, W1-W2 vs 4.5 μ m magnitude, I1-I2 vs 4.5 μ m magnitude, and I1-I2 vs MJD diagrams.

J03283452+3107055

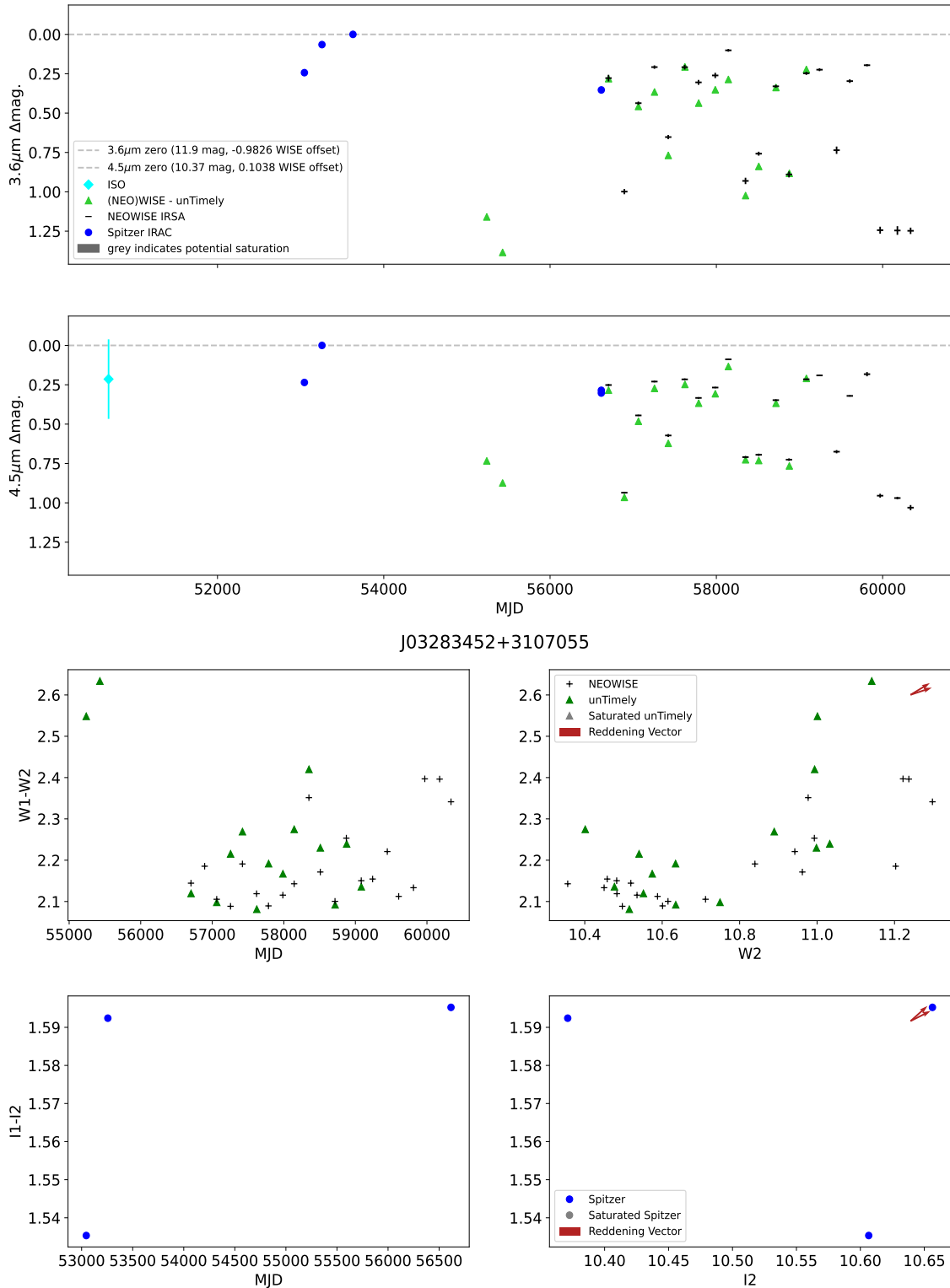


Figure 19. See above.

J03285102+3118184

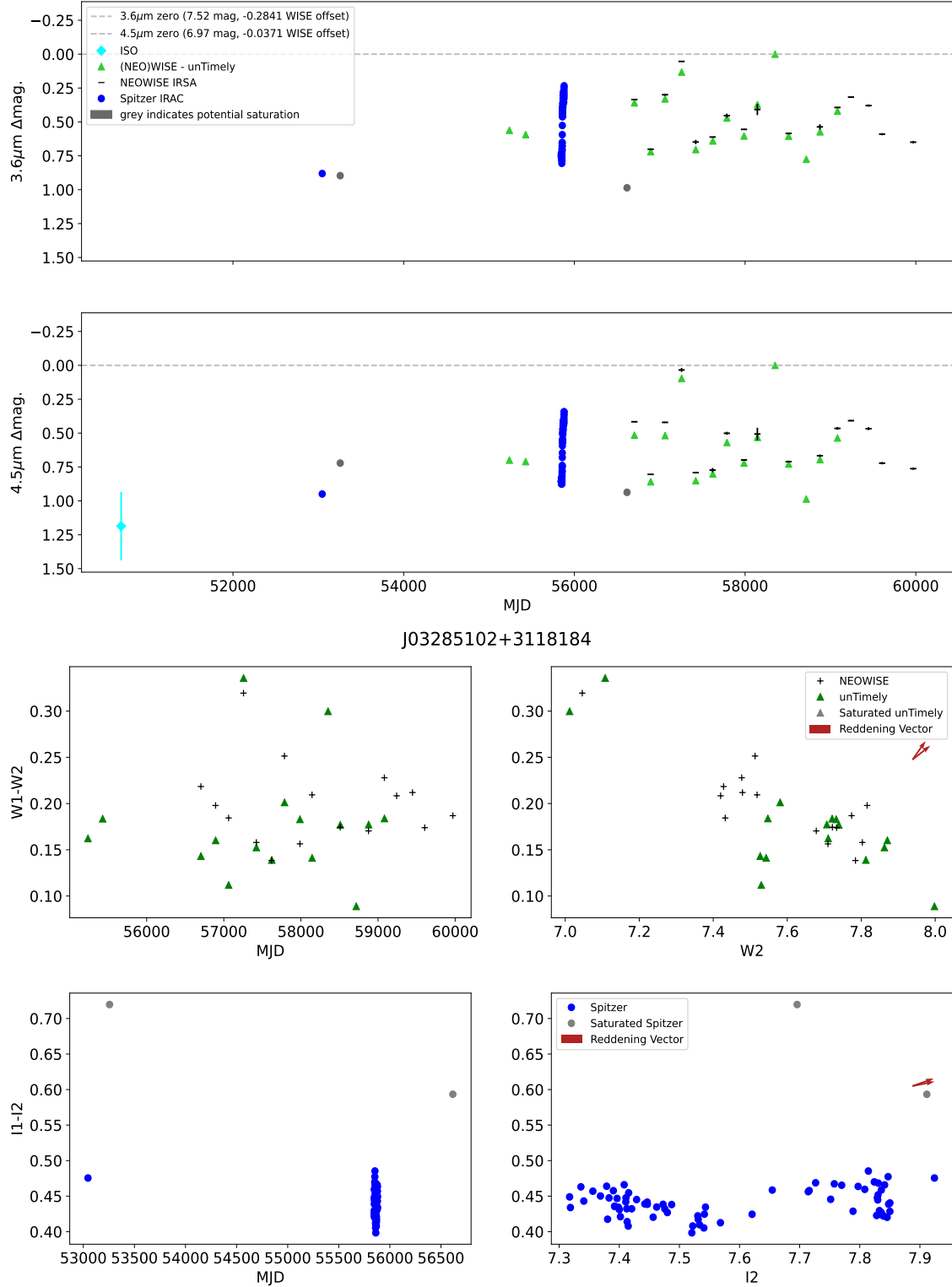


Figure 19. See above.

J03292042+3118343

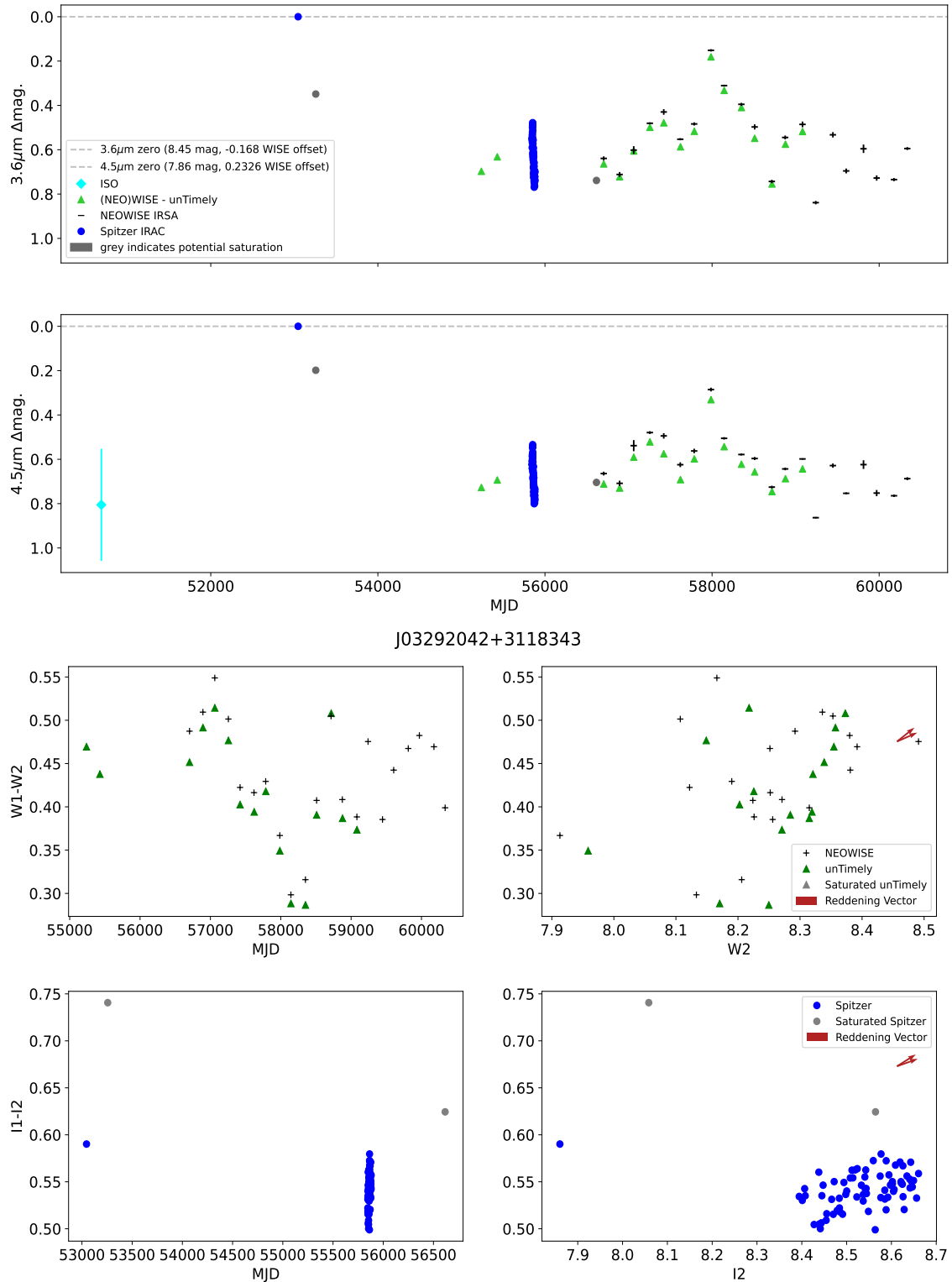


Figure 19. See above.

J03284529+3105419

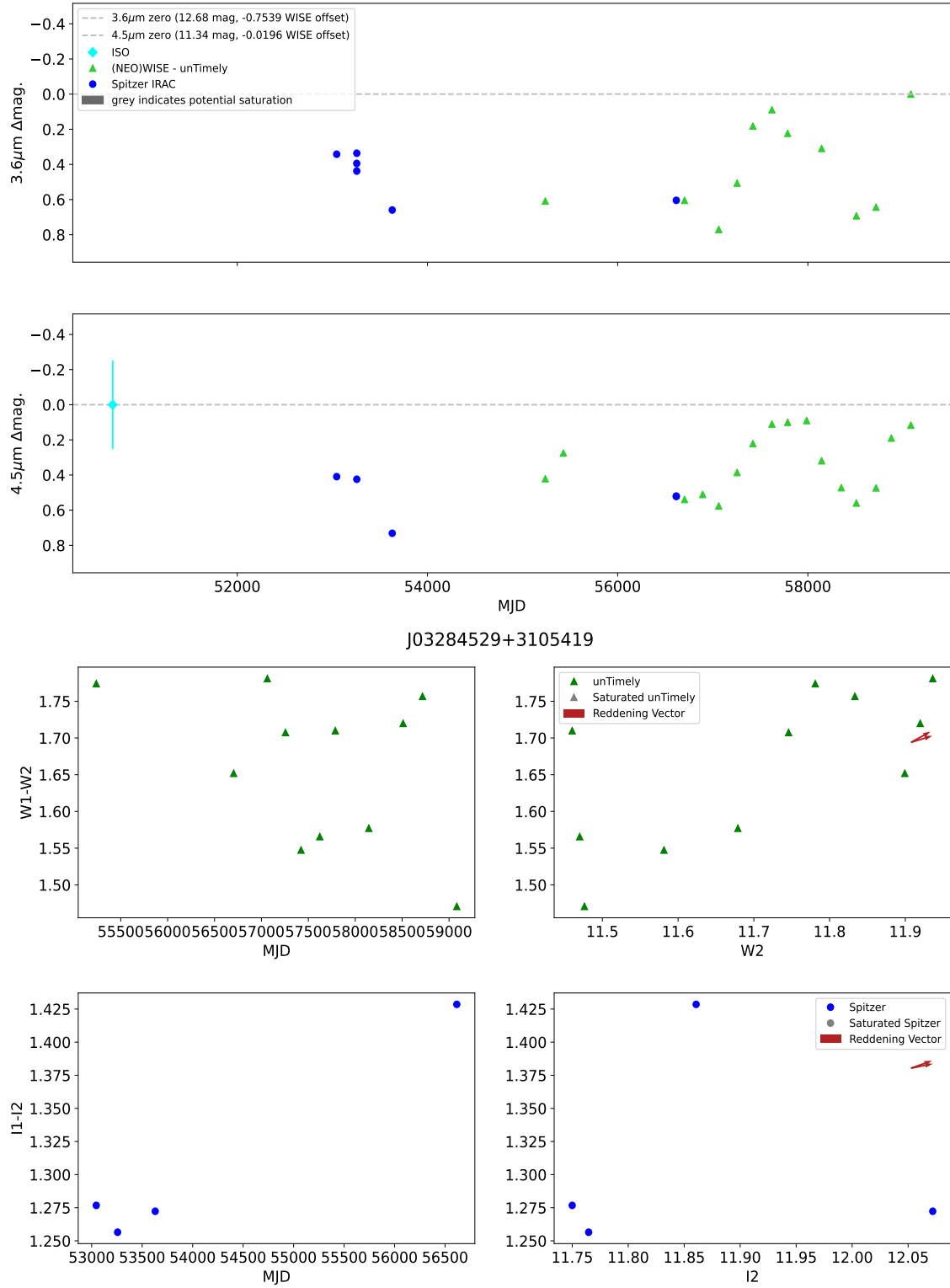


Figure 19. See above.

J03285120+3119549

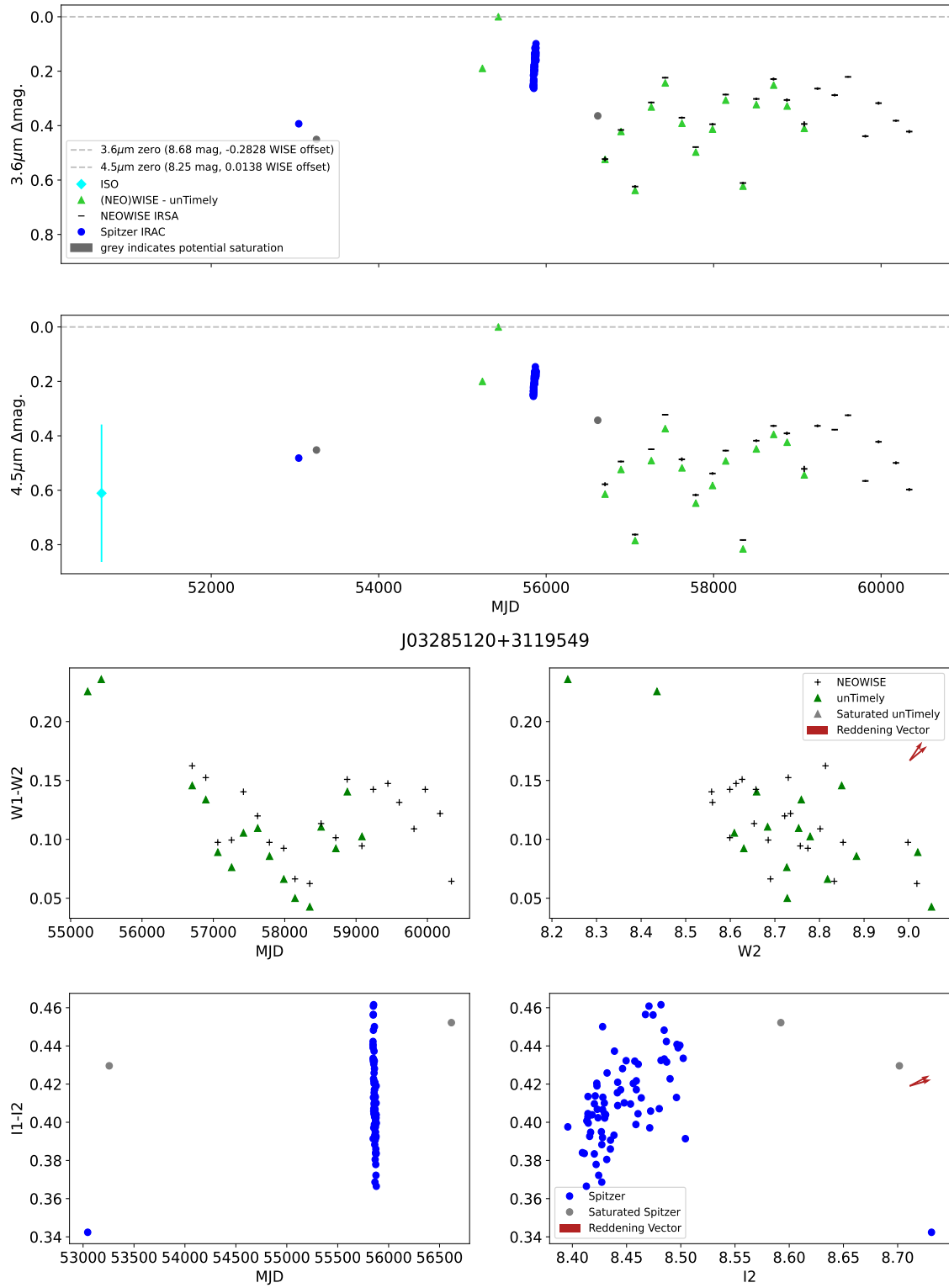


Figure 19. See above.

J03285216+3122453

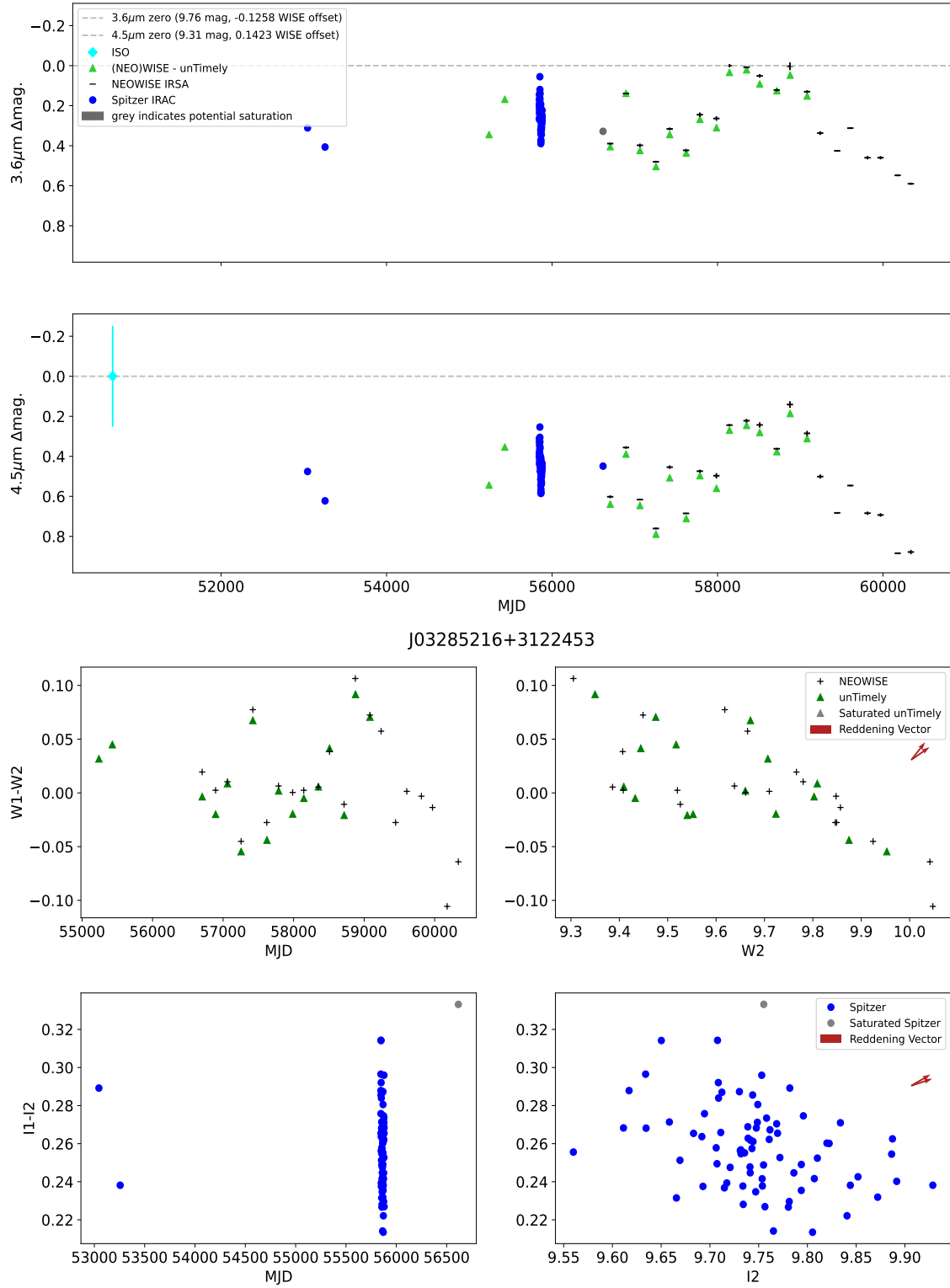
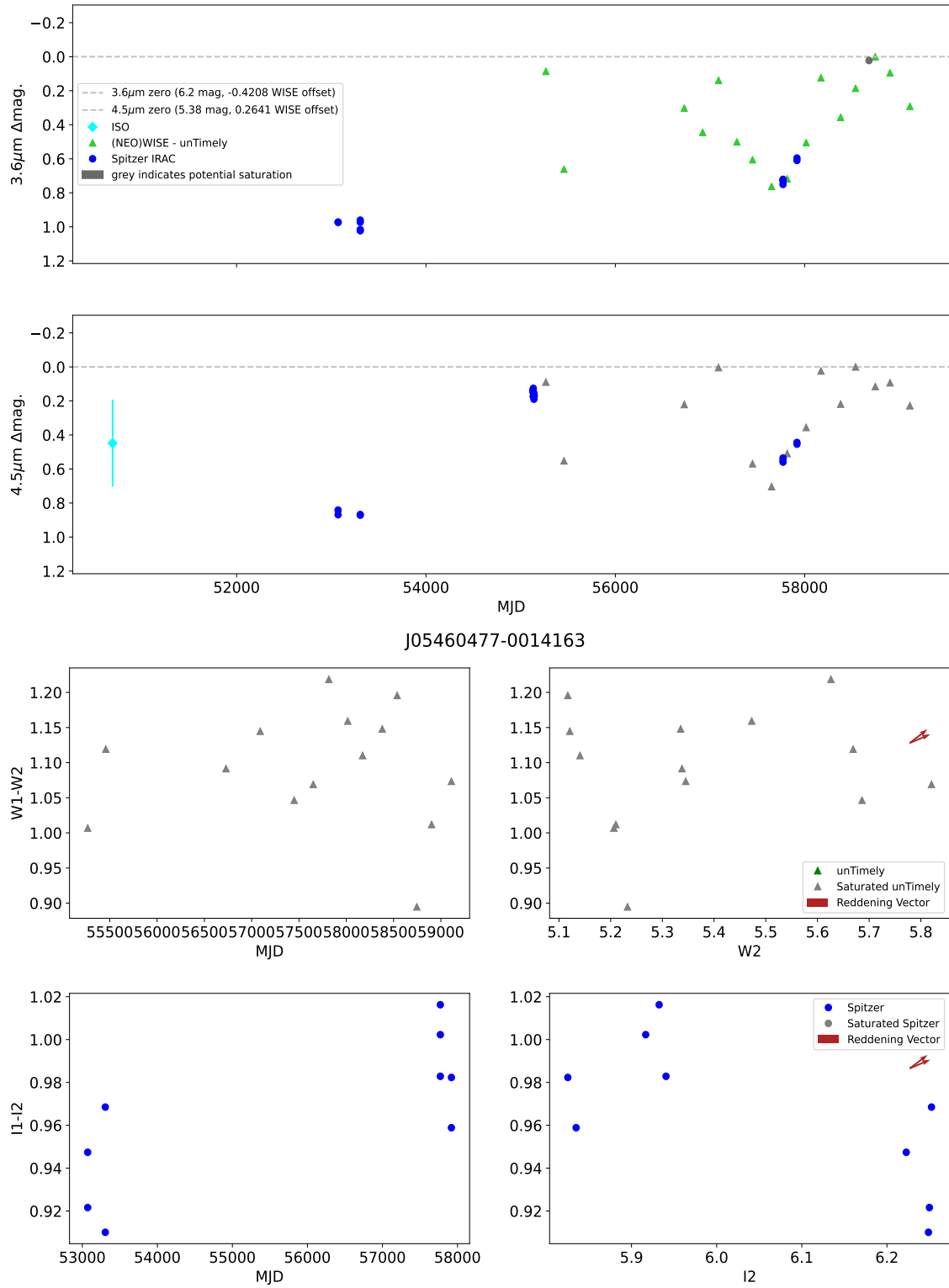


Figure 19. See above.

J05460477-0014163

**Figure 19.** See above.

J05460363-0014492

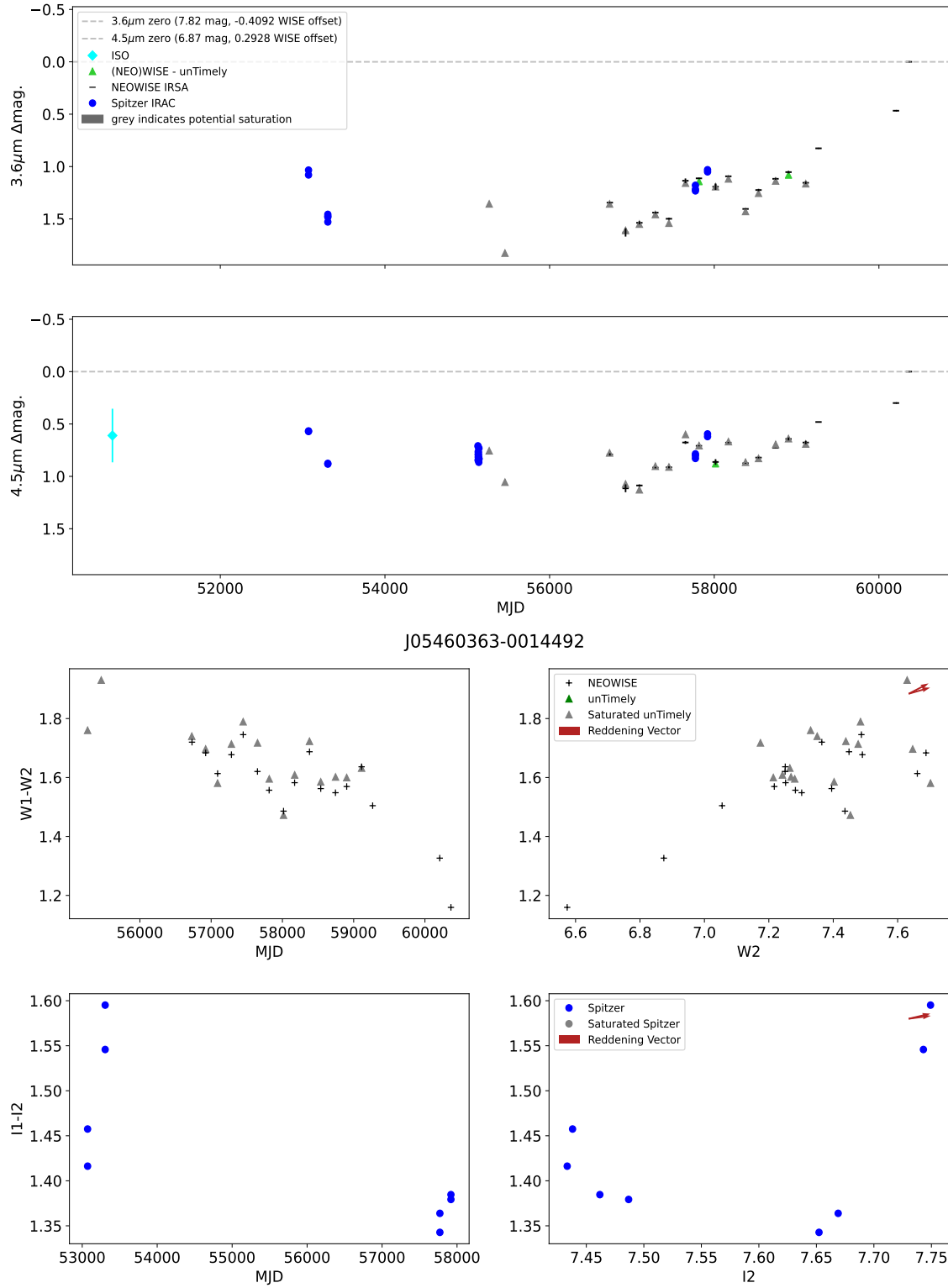


Figure 19. See above.

J05405172-0226486

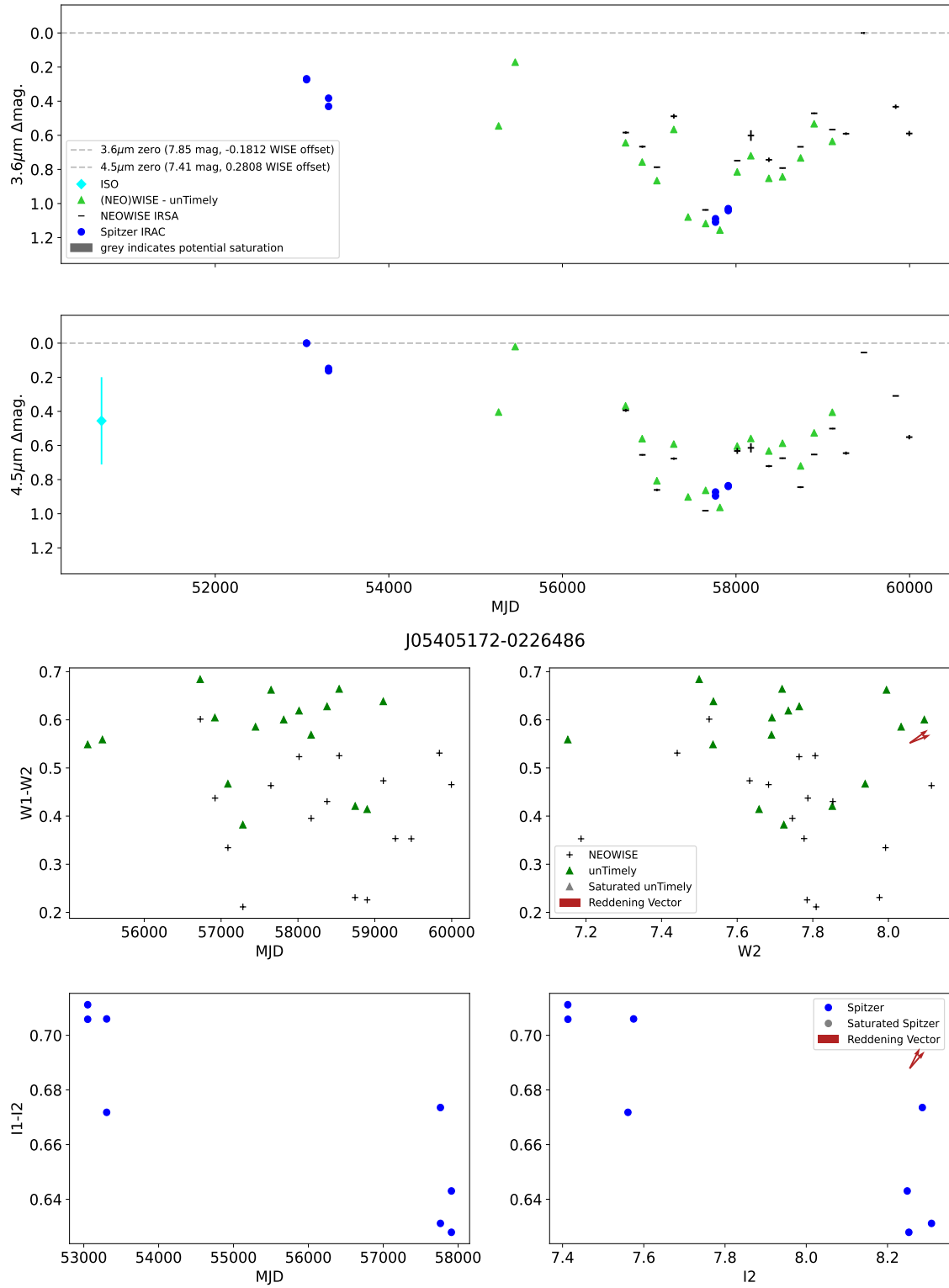


Figure 19. See above.

J05413972-0202241

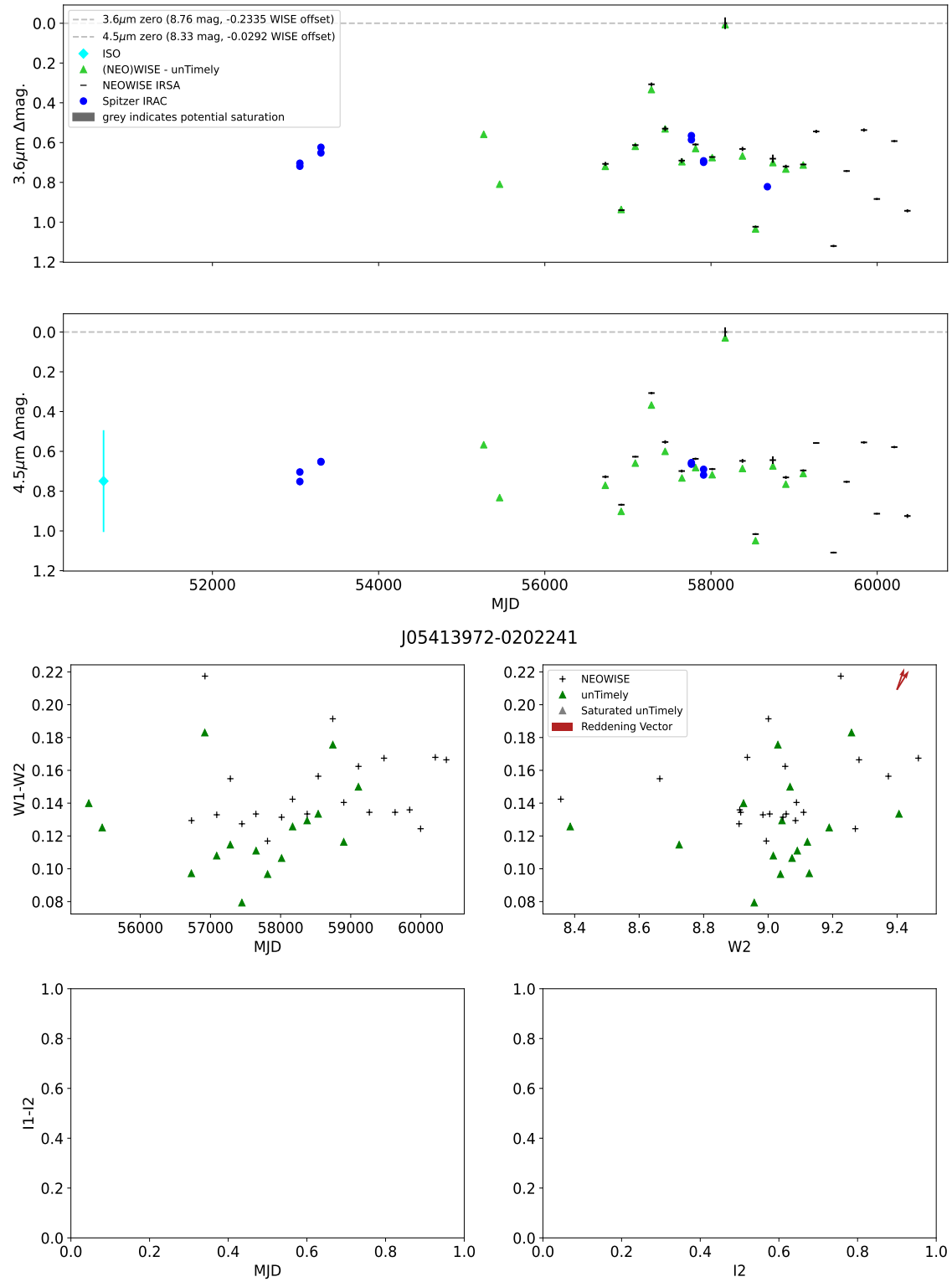


Figure 19. See above.

J05471062+0021141

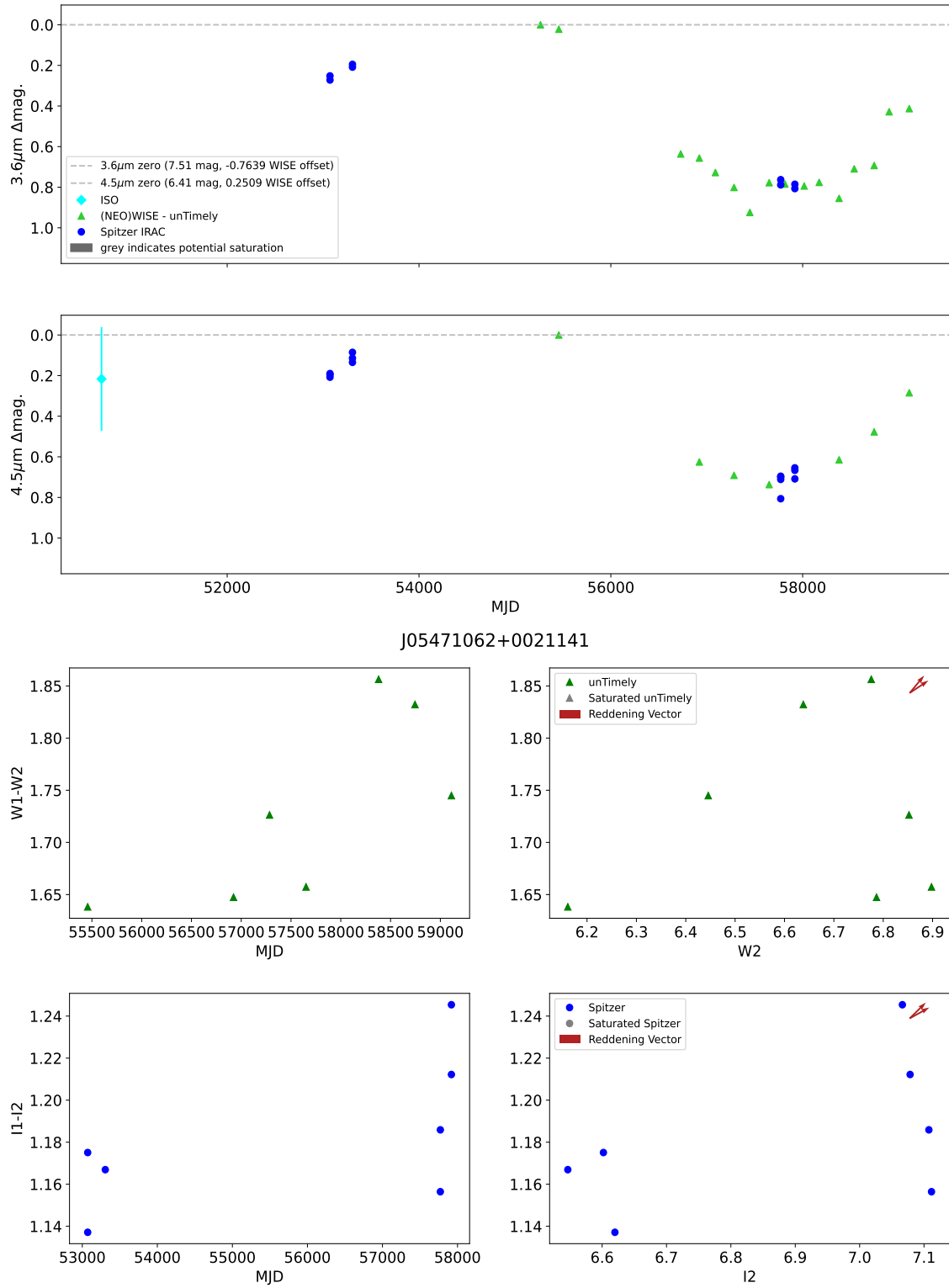


Figure 19. See above.

J05455630+0007085

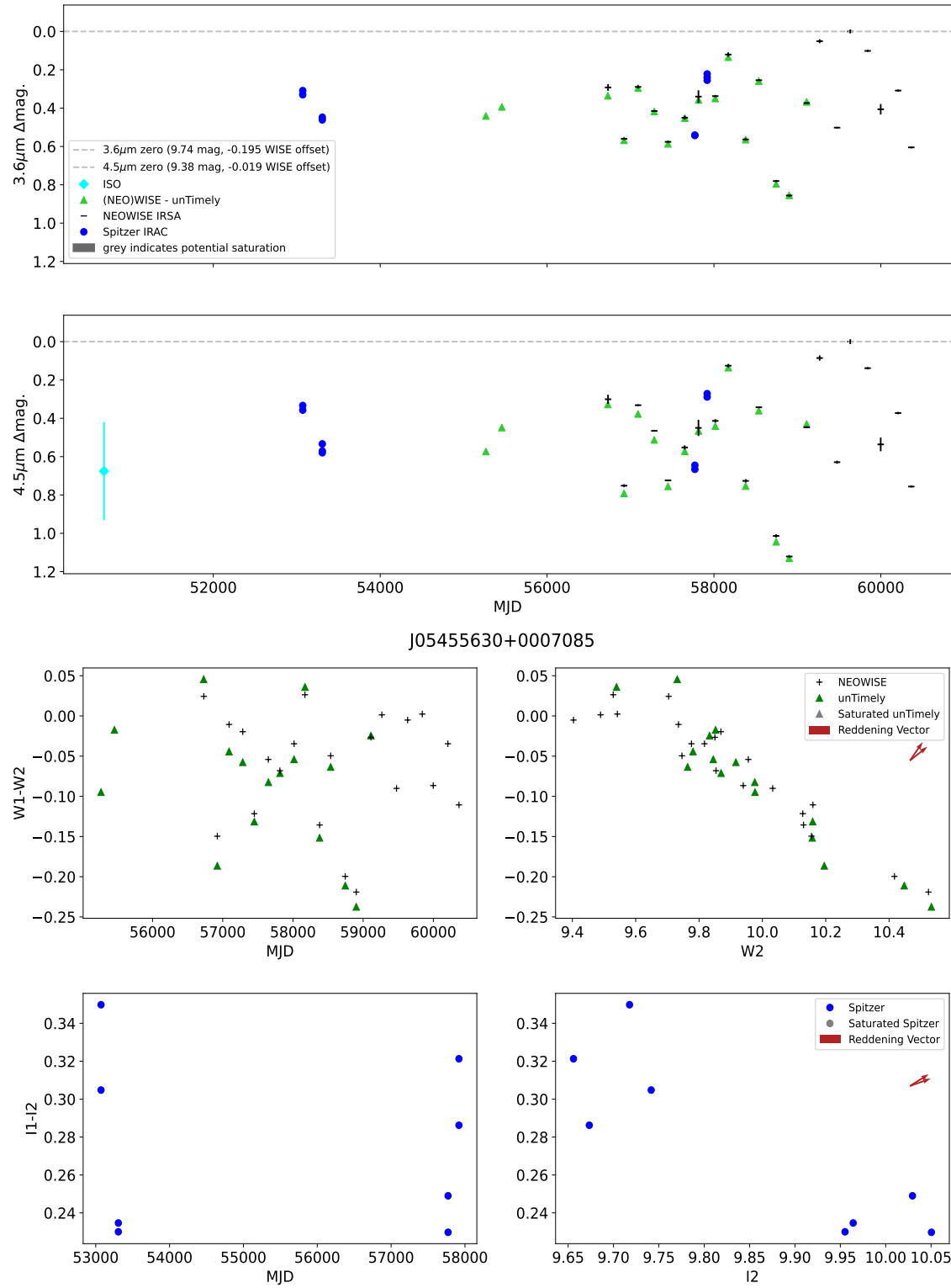


Figure 19. See above.

J05415555-0223405

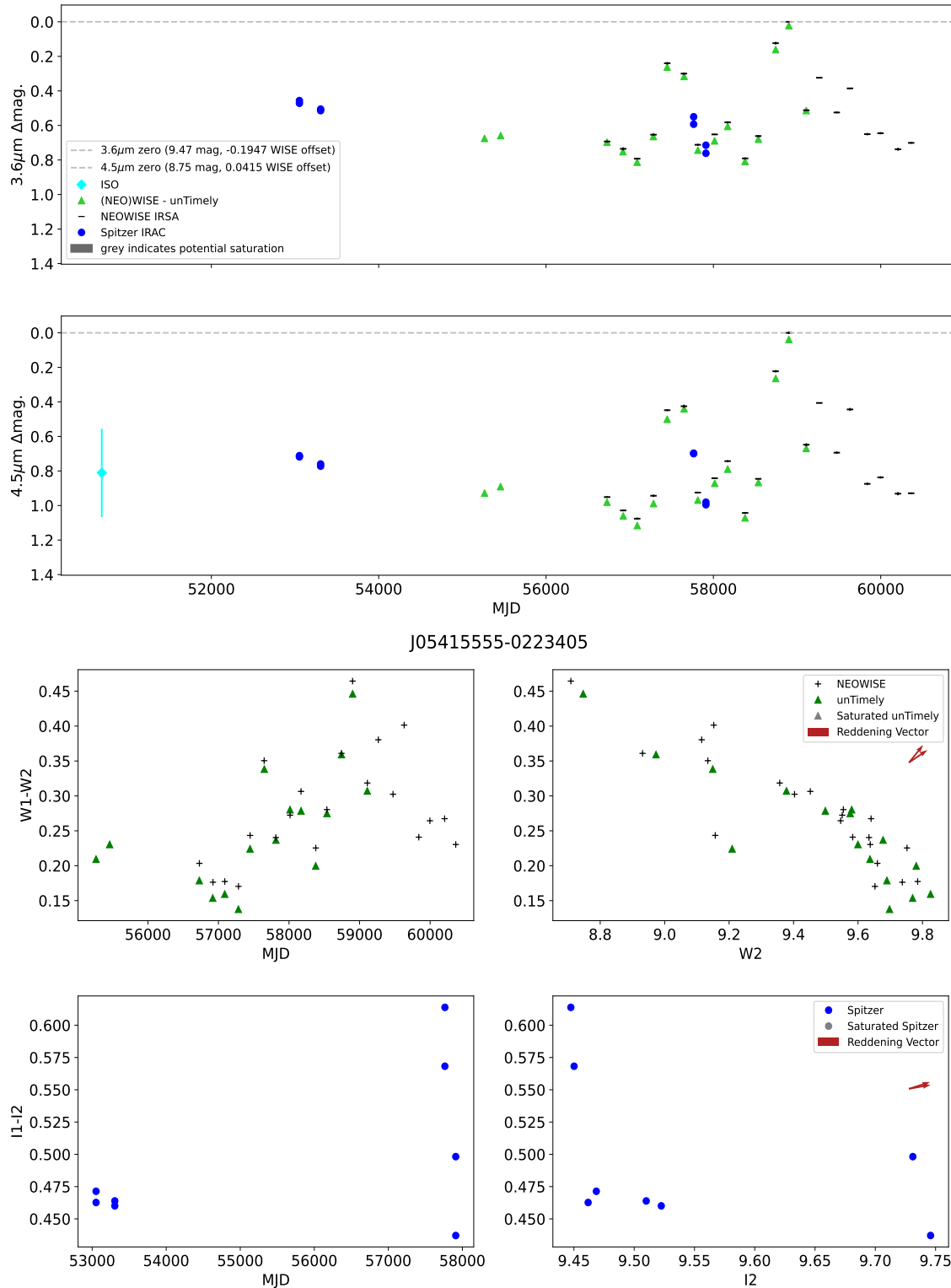


Figure 19. See above.

J05464741+0012594

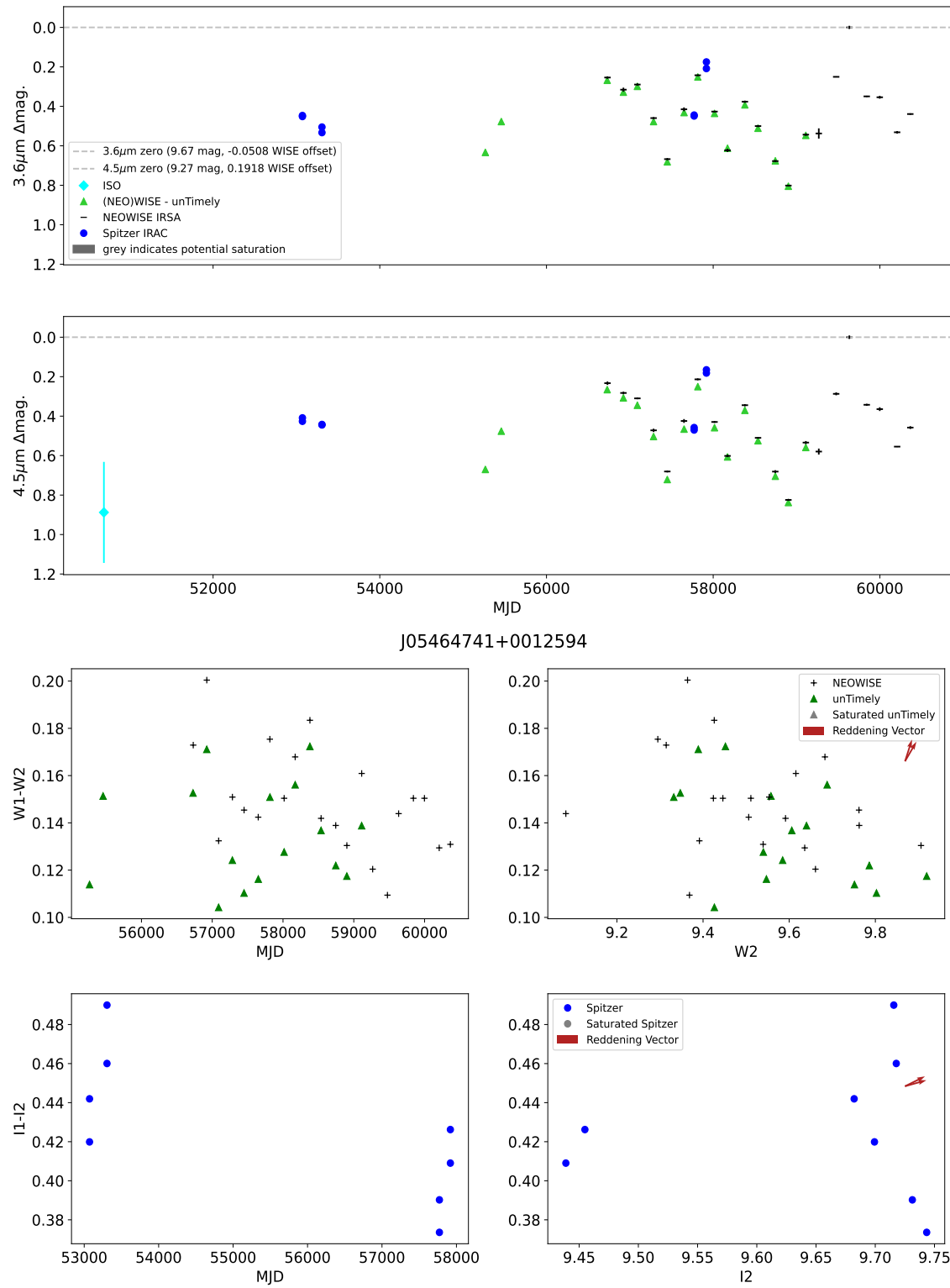


Figure 19. See above.

J16272180-2429536

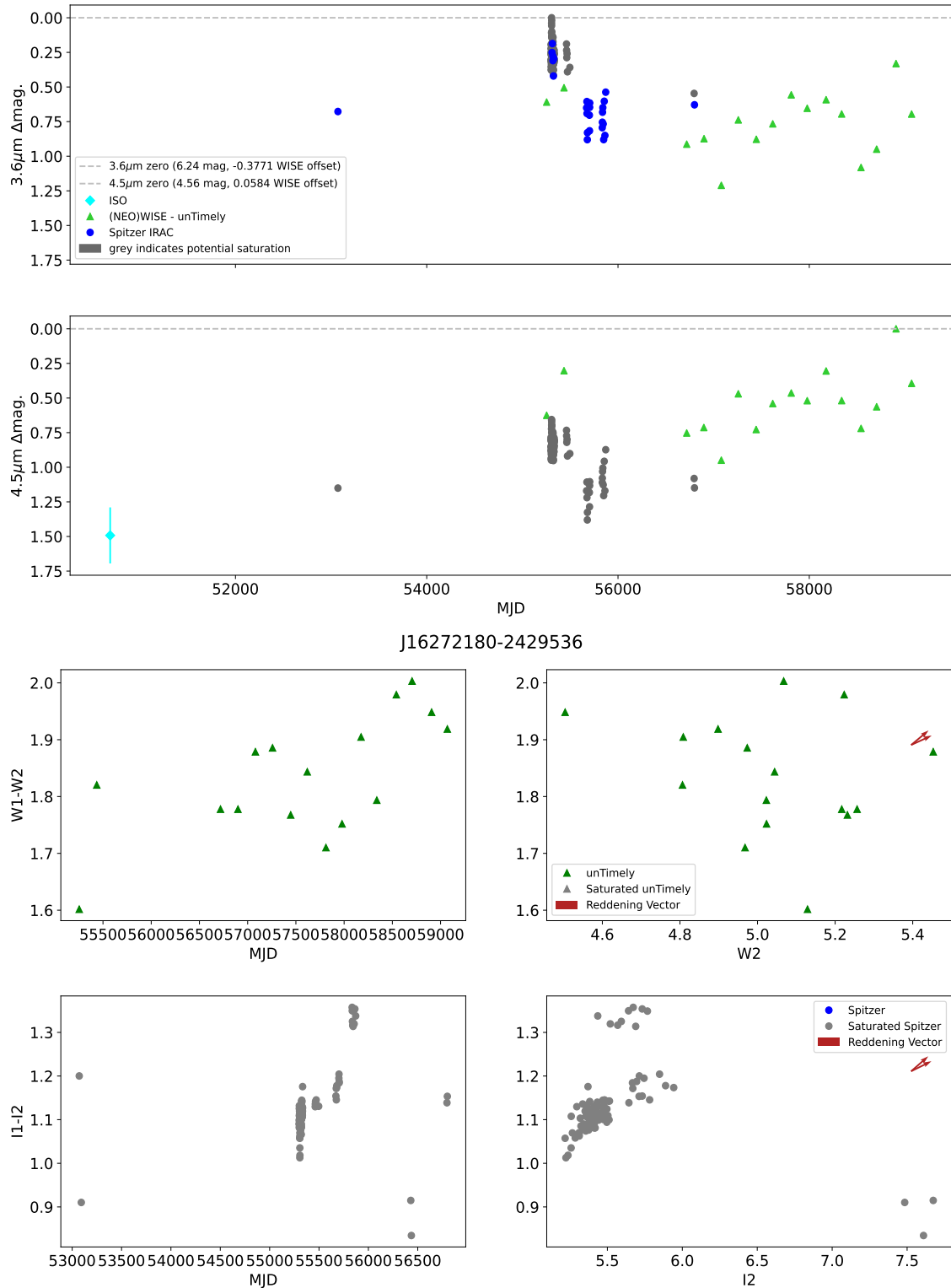


Figure 19. See above.

J16264421-2434487

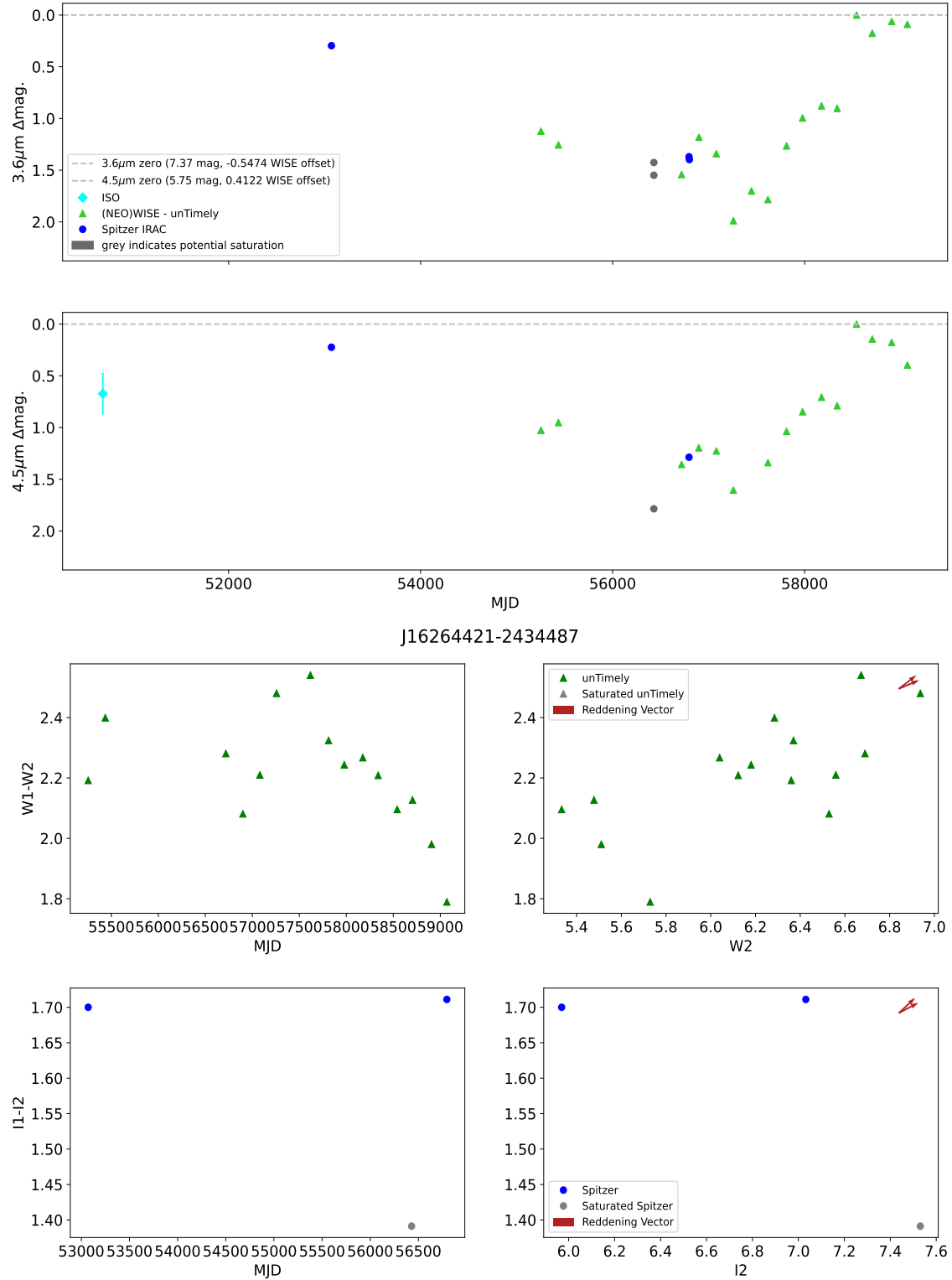


Figure 19. See above.

J16274162-2446450

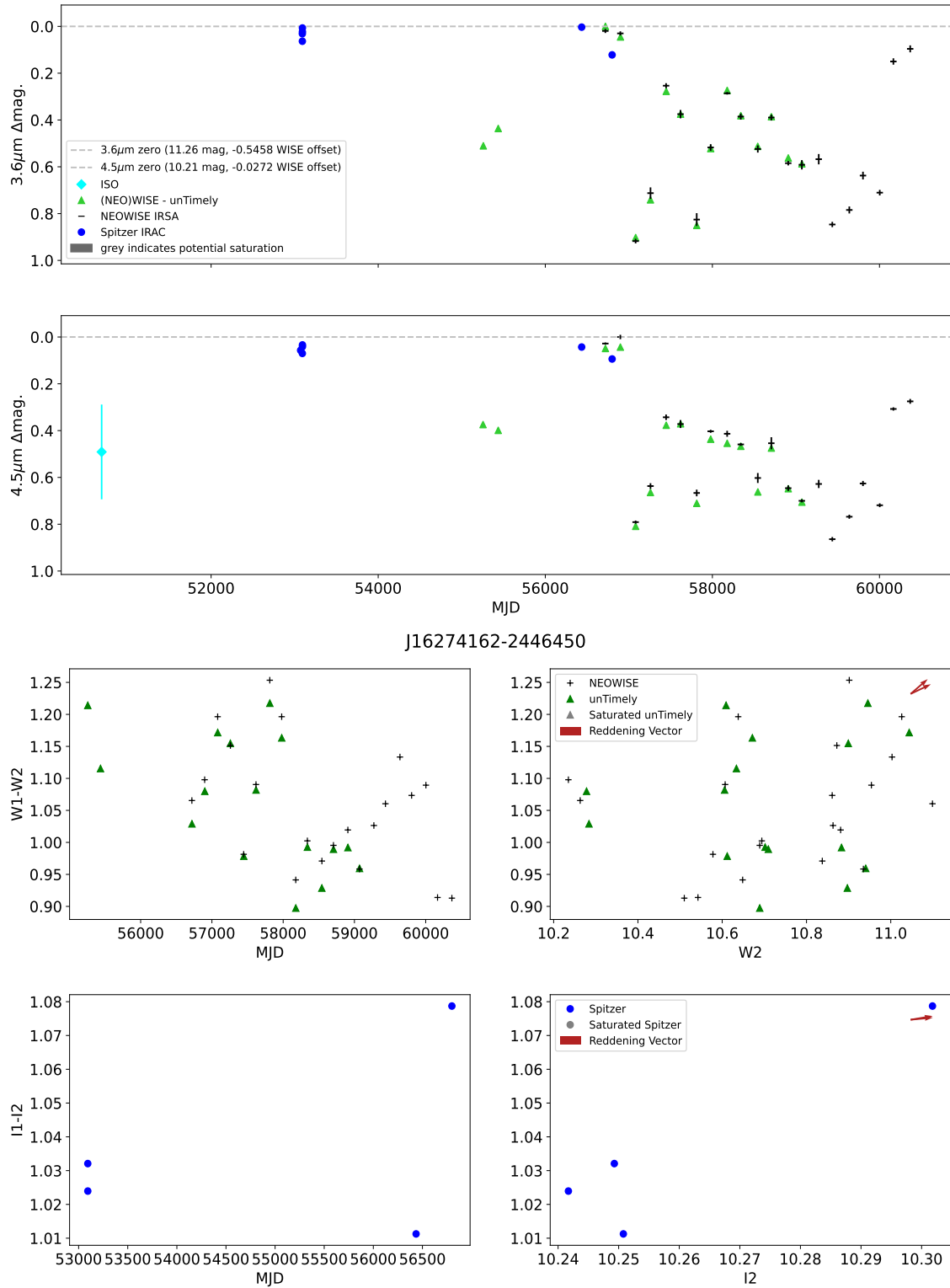


Figure 19. See above.

J16264048-2427146

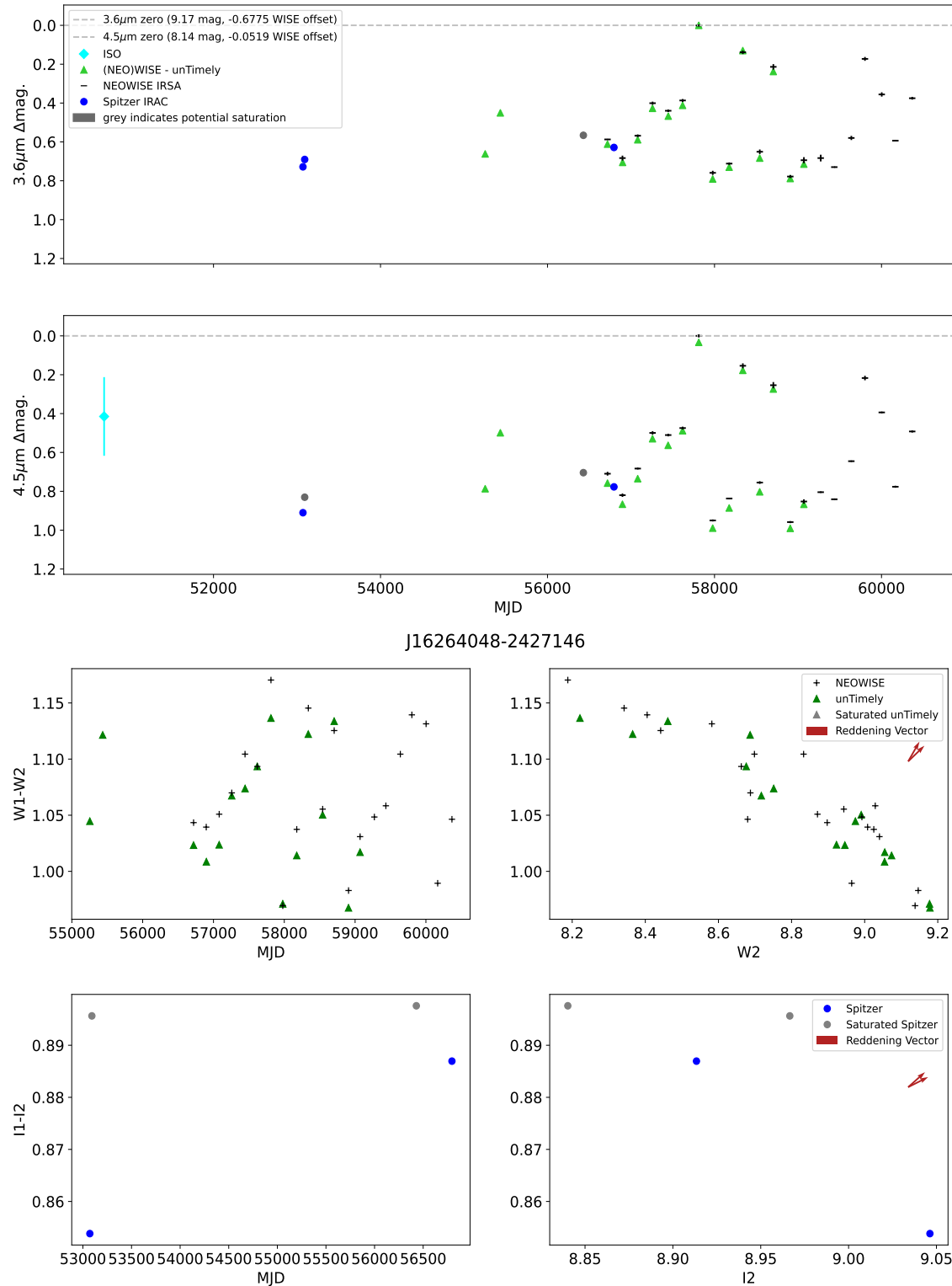


Figure 19. See above.

J16262755-2441538

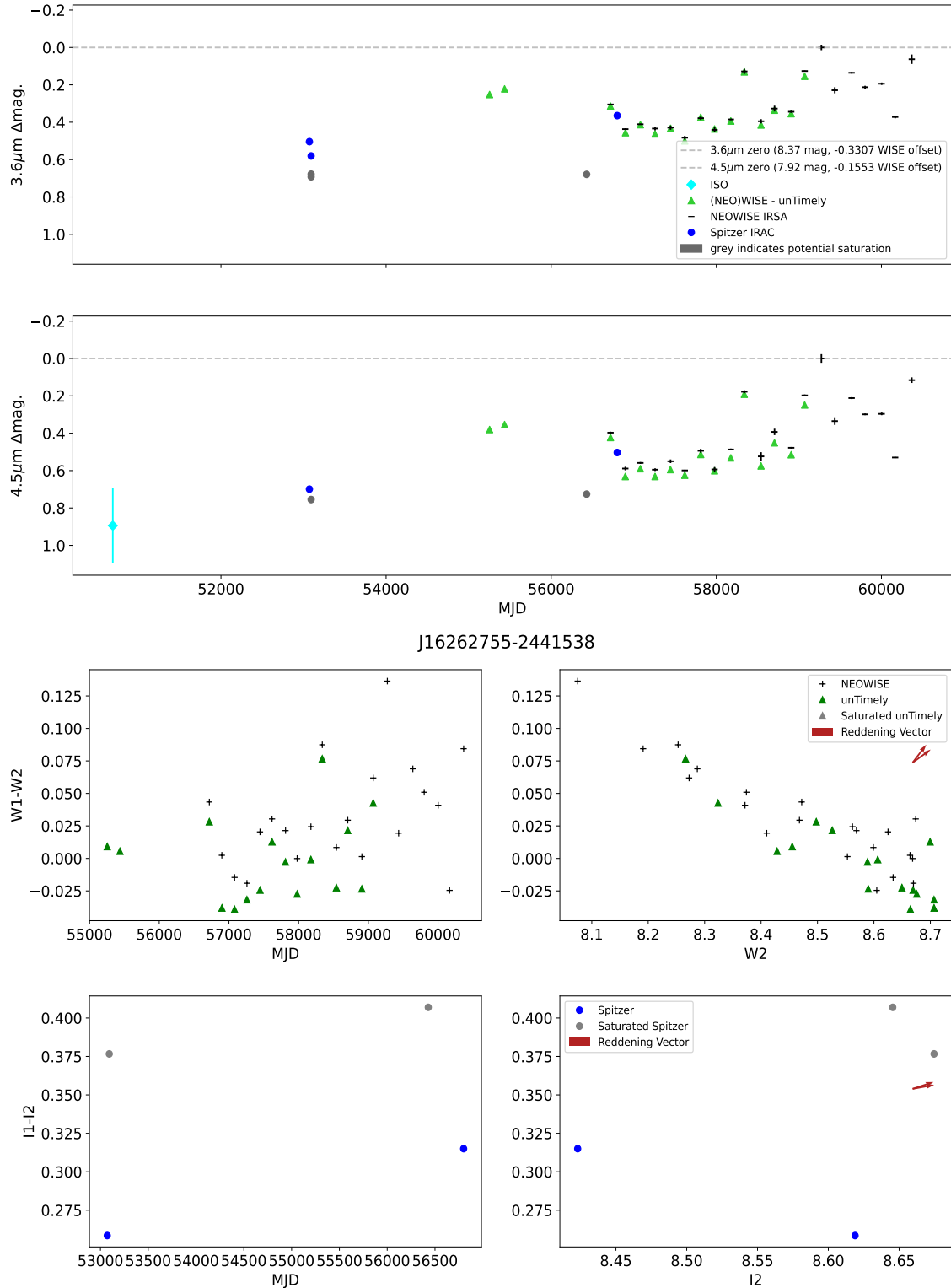
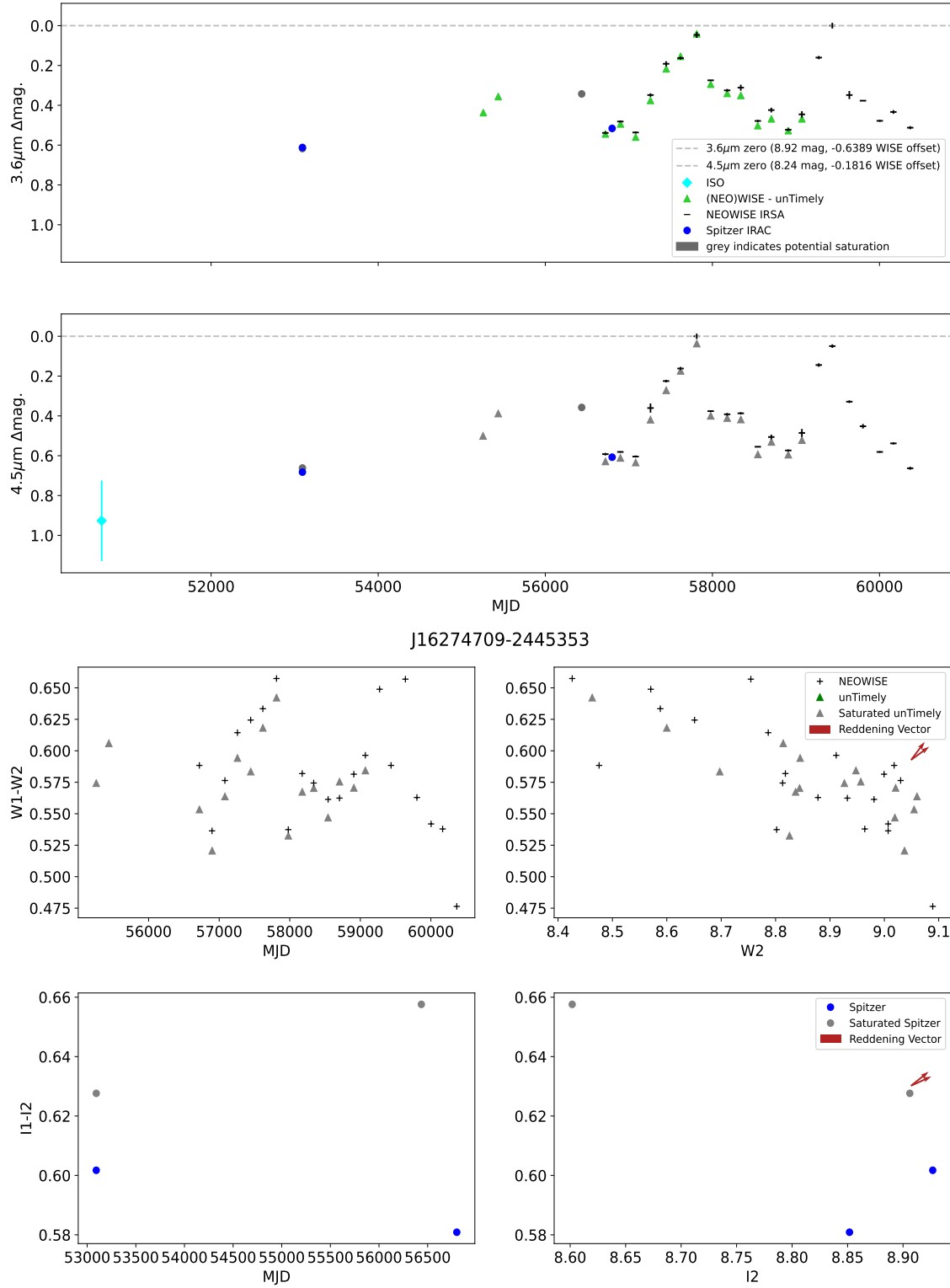


Figure 19. See above.

J16274709-2445353

**Figure 19.** See above.

J18295117+0116404

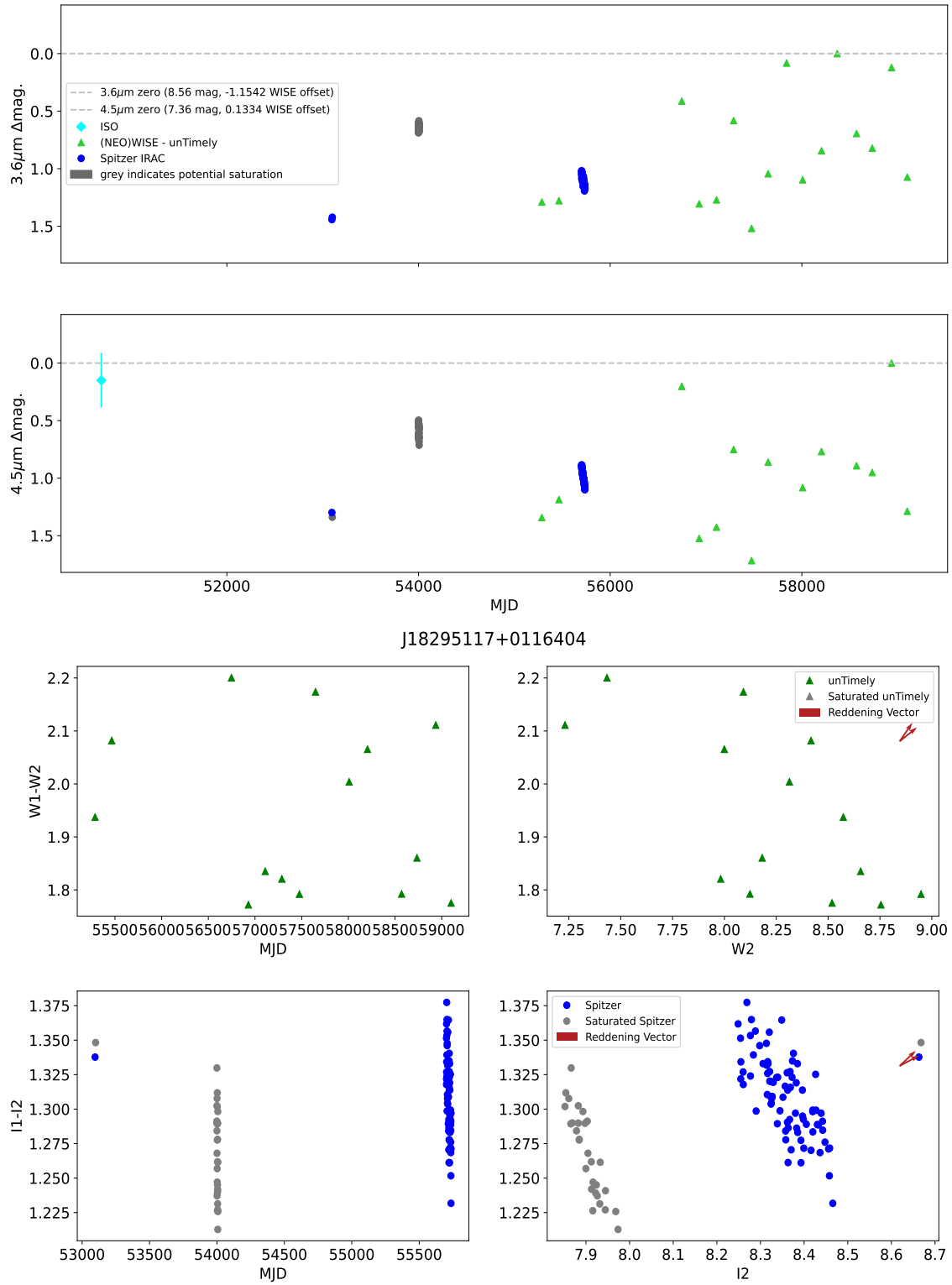


Figure 19. See above.

J18295954+0111583

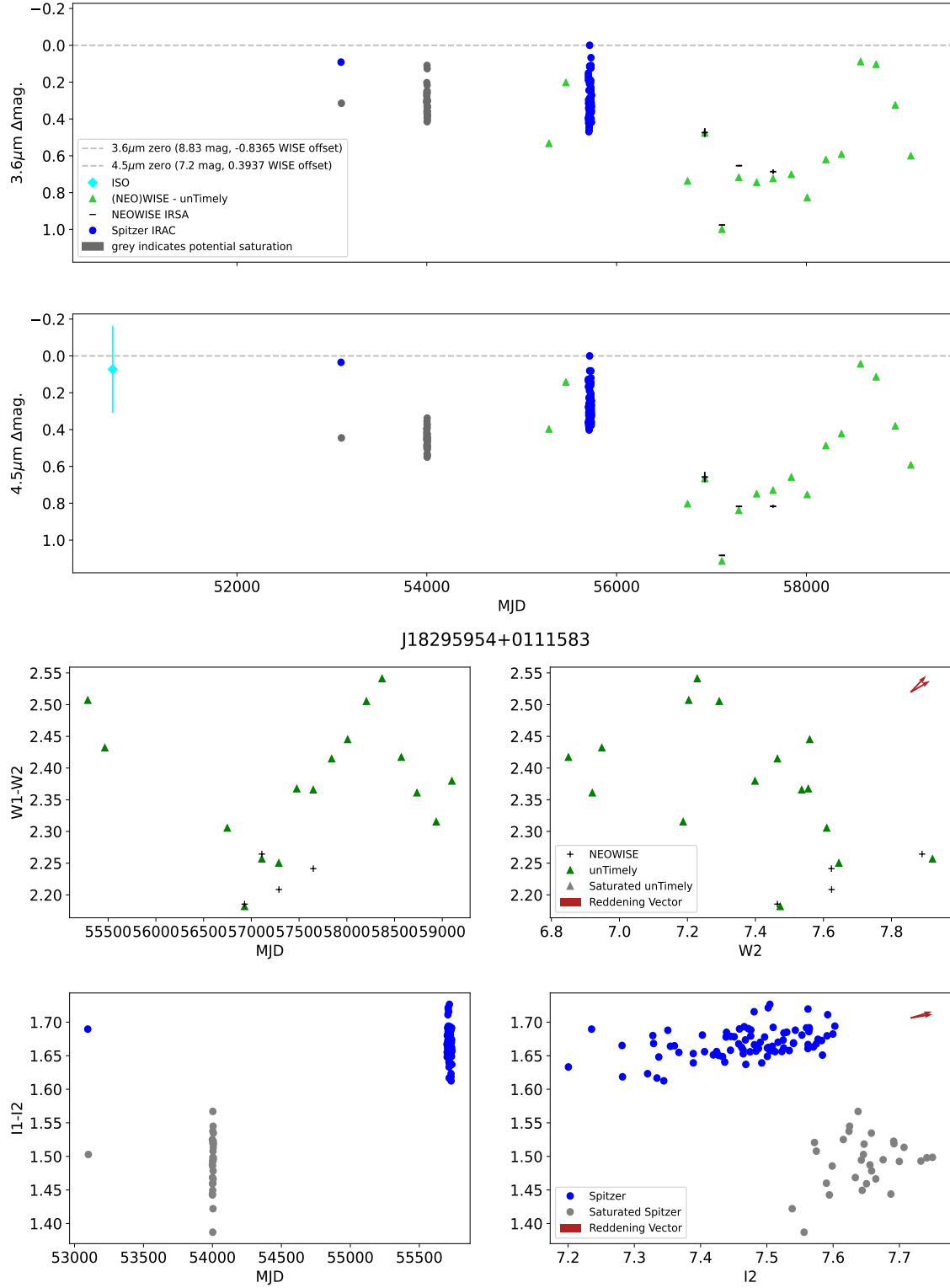
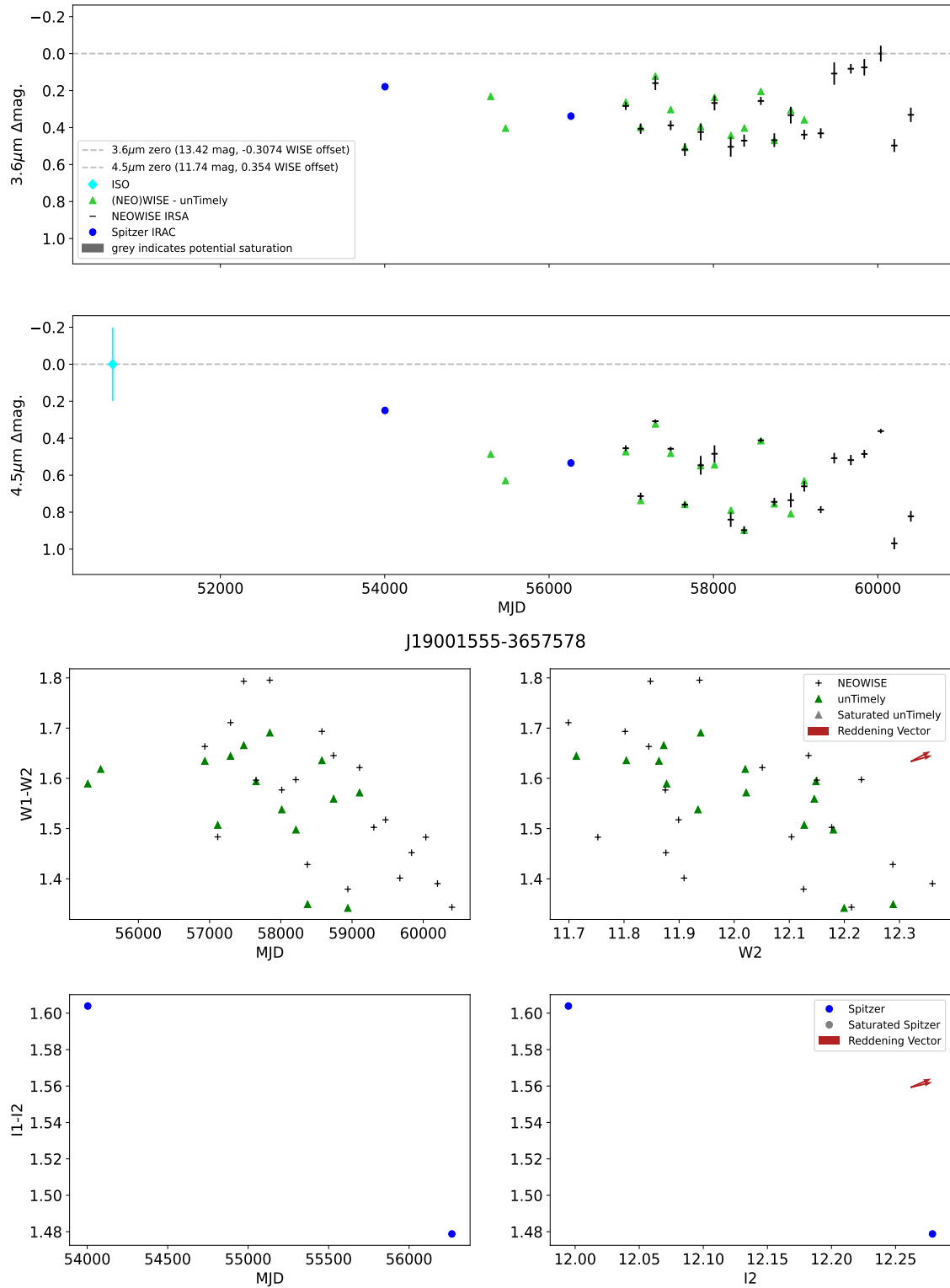


Figure 19. See above.

J19001555-3657578

**Figure 19.** See above.

J11094191-7634585

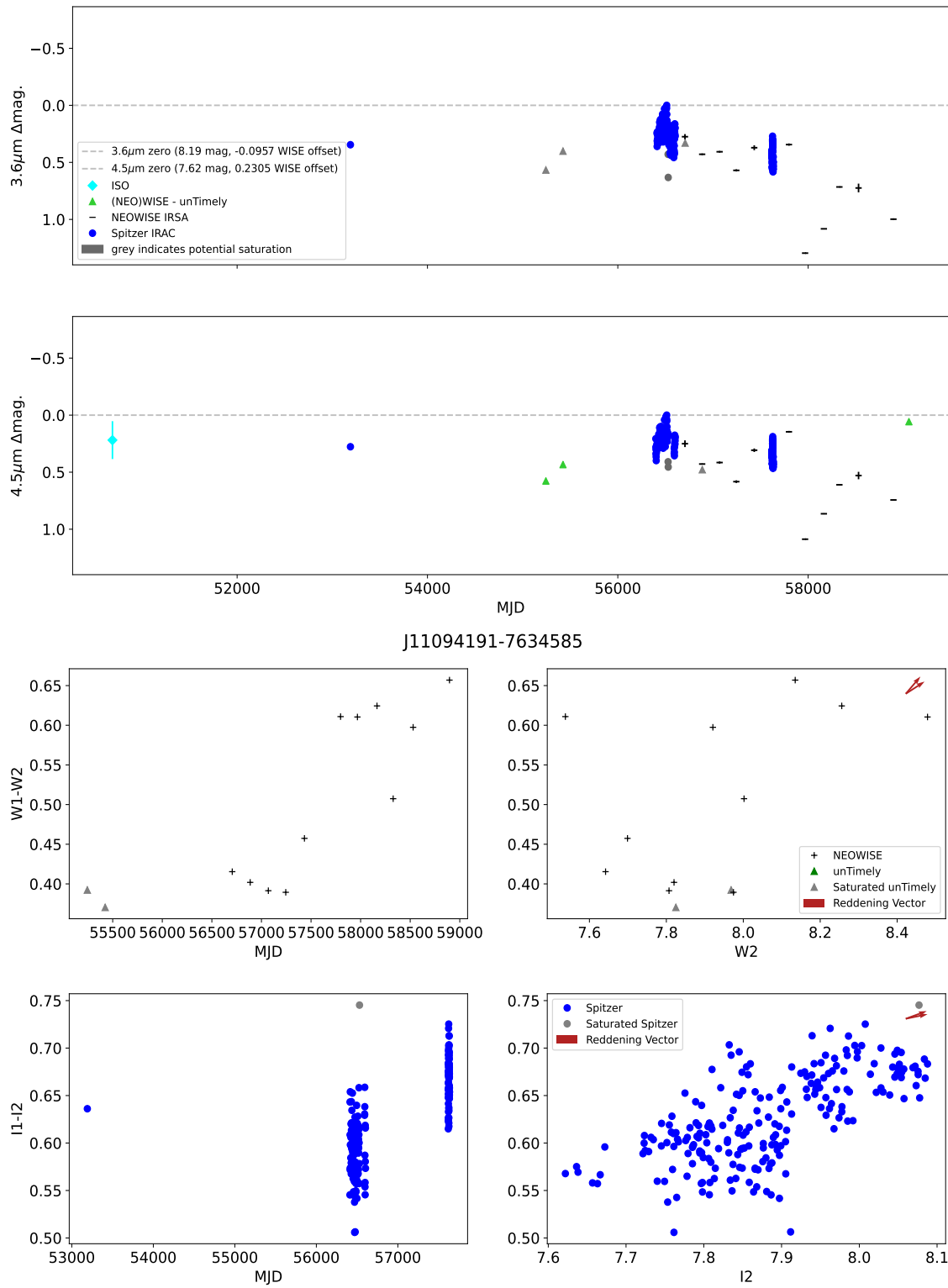
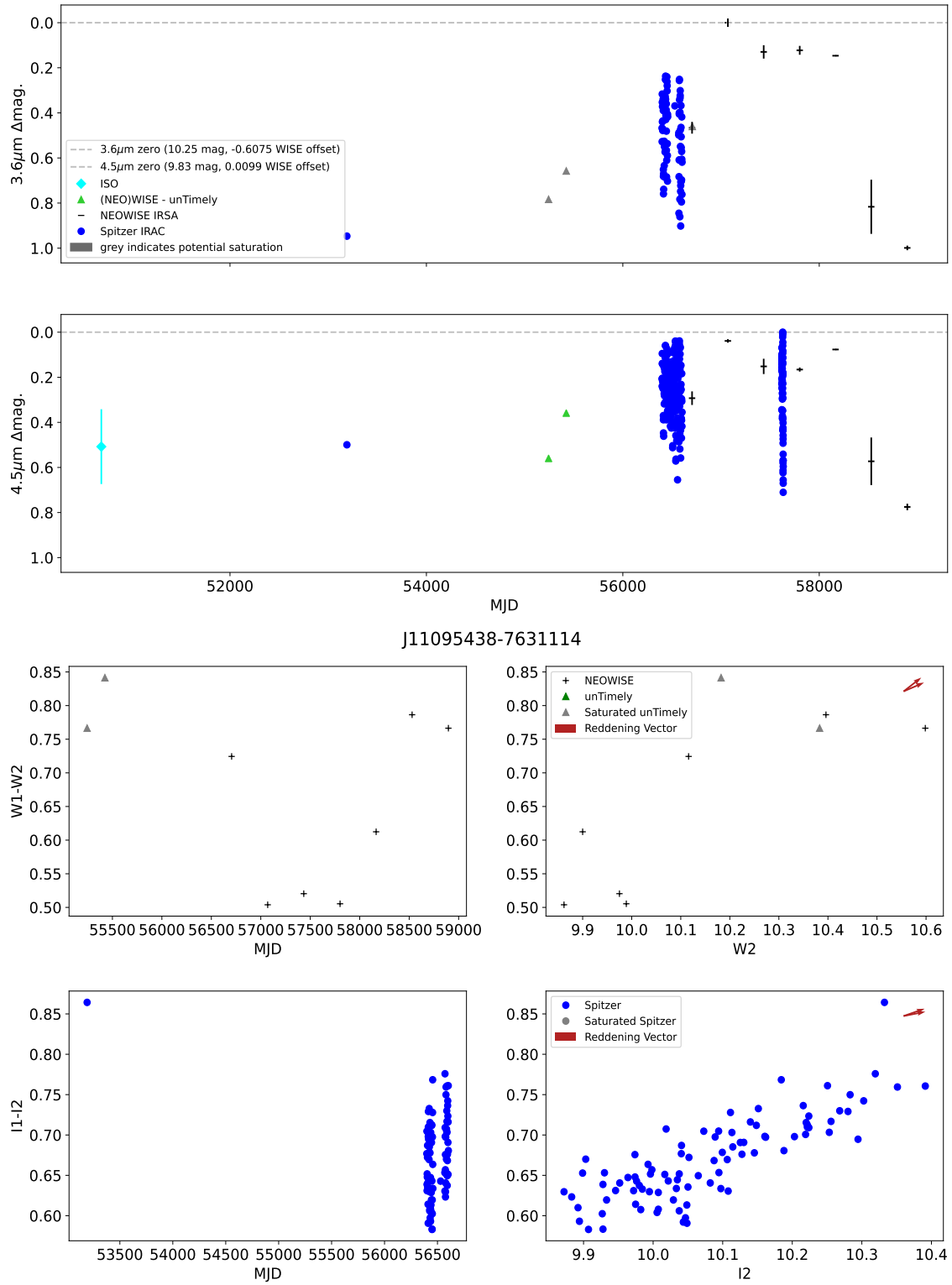


Figure 20. See above.

J11095438-7631114

**Figure 20.** See above.